Fast Scanning Calorimetry Studies of Molecular Dynamics in Crystals, Liquids, and Glasses

by Ulyana Sorokopoud Cubeta

A.A. in Liberal Arts, June 2004, Bard High School Early College
B.A. in Earth and Environmental Science, May 2008, Wesleyan University
B.A. in Chemistry, May 2008, Wesleyan University
M.A. in Chemistry, September 2010, Princeton University

A Dissertation submitted to

The Faculty of
The Columbian College of Arts and Sciences
of The George Washington University
in partial fulfillment of the requirements
for the degree of Doctor of Philosophy

May 20, 2018

Dissertation directed by

Vladislav Sadtchenko
Associate Professor of Chemistry

The Columbian College of Arts and Sciences of The George Washington University certifies that Ulyana Sorokopoud Cubeta has passed the Final Examination for the degree of Doctor of Philosophy as of March 23, 2018. This is the final and approved form of the Dissertation.

Fast Scanning Calorimetry Studies of Molecular Dynamics
in Crystals, Liquids, and Glasses

Ulyana Sorokopoud Cubeta

Dissertation Research Committee:

Vladislav Sadtchenko, Associate Professor of Chemistry, Dissertation Director

Michael J. Wagner, Associate Professor of Chemistry, Committee Member

Henry Teng, Associate Professor of Chemistry and Geosciences, Committee Member

© Copyright 2018 by Ulyana S. Cubeta
All rights reserved

Dedication

I dedicate this dissertation to my grandmother,

Luybov Sorokopoud, a chemist and a mother.

Acknowledgements

I am extremely grateful to my research advisor, Dr. Vlad Sadtchenko, who restored my faith in science. Спасибо. I would like to thank my colleagues, Dr. Deepanjan Bhattacharya and Rinipal Kaur, for their kindness and support. I am also grateful to the mentors who supported my early scientific endeavors: Dr. Salwen, Dr. Roberts, Dr. Ku, and Dr. Westmoreland.

Finally, I would like to express my deepest gratitude to my family, especially my husband, Jeffrey, and my mother-in-law, Barbara. Thank you for keeping our boat sailing.

Abstract of Dissertation

Fast Scanning Calorimetry Studies of Molecular Dynamics
in Crystals, Liquids, and Glasses

There is a dearth of experimental techniques that can probe the dynamic properties of non-equilibrium condensed phases, particularly in materials characterized by very slow kinetics, such as glasses. Although fundamental theories on the glass transition and the properties of glass-forming liquids abound, none can be validated because there is insufficient experimental data on the molecular dynamics of these materials at temperatures near the glass transition. In this Dissertation, I demonstrate the utility of a novel technique, Fast Scanning Calorimetry (FSC), to interrogate the kinetic and thermodynamic parameters of non-equilibrium condensed phases. The custom-built, quasi-adiabatic, thin-wire calorimeter can quickly heat micrometer-scale crystalline, liquid, or glassy samples, all rapidly prepared by vapor deposition, to obtain high resolution and accurate data for non-equilibrium structural relaxation. Essentially, fast temperature scanning vibrationally perturbs the material far from its initial or equilibrium state and the calorimeter can measure the structural response of the material to these thermal perturbations.

My FSC studies reveal that, in the limit of high heating rates on the order of 10^6 K/s, the kinetics of any phase transition, e.g. glass devitrification, viscous liquid relaxation, or crystalline melting, simplify greatly to follow a zero-order rate law with an Arrhenius-like temperature dependence. The discovery of this unique kinetic regime, along with the analytical methodology developed in this Dissertation, have opened a new venue for gathering data on the molecular mobility of glassformers at low temperatures. Studies on the melting of superheated molecular crystals illustrate the capabilities of FSC and expose long-held misconceptions on the mechanism of heterogeneous melting. The observed high

activation energy barriers to this diffusion-limited process demonstrate that, under conditions of rapid heating, the structure of the material at the crystalline-amorphous interface is surprisingly similar to that of a glass.

Furthermore, FSC studies that compare the devitrification of ordinary, melt-cooled glasses and vapor-deposited amorphous phases confirm that both materials can undergo heterogeneous, surface-facilitated relaxation when heated with a sufficiently high rate. The high activation energies for these relaxation processes reflect the kinetic properties of the materials in their initial states at low temperatures, not at the temperatures at which transformation occurs. FSC studies that utilized a set of glass-forming liquid samples with well-defined initial states confirm the impact of initial sample temperature on the transformation rate and provide validation for a proposed model of front-propagated structural relaxation. In fact, the data measured by FSC can be used to calculate the thermodynamic driving force for front propagation and provide quantitative validation of the proposed relaxation mechanism.

Finally, the FSC relaxation rate data with the aforementioned sample set shows an astounding correlation with molecular self-diffusion at low temperatures, demonstrating that the technique can be used to measure diffusivity in condensed phases with very slow dynamics, even below the glass transition. The last study of this Dissertation is a preliminary exploration of the slow molecular kinetics in amorphous vapor-deposited materials with very stable initial structures. The results of these experiments implicate the existence of a crossover in equilibrium mobility parameters at temperatures below the glass transition, an unprecedented finding that may have a significant impact on developing an accurate theoretical framework for the formation and devitrification of glasses.

Table of Contents

Dedication iv

Acknowledgements v

Abstract of the Dissertation vi

List of Figures xi

List of Tables xiv

List of Variables and Abbreviations xv

Chapter One: Introduction 1

1.1. An overview 1

1.2. Distinctions between glasses and liquids 2

1.3. Characteristic temperatures: T_g and T_f 3

1.4. Kinetic parameters and fragility 5

1.5. The unique temperature dependence of diffusivity 7

1.6. Dynamic heterogeneities in deeply supercooled liquids 11

1.7. Two-fold problem of glass science: time^2 13

1.8. Faster sample preparation by vapor deposition 15

1.9. Impediments to measurements: observation time 16

1.10. Fast Scanning Calorimetry (FSC): a path for transformative research on the glass transition 18

1.11. Dissertation objectives 20

1.12. References for Chapter One 21

Chapter Two: Experimental apparatus and procedures 30

2.1. Brief overview of Fast Scanning Calorimetry (FSC) 30

2.2. Essential hardware 30
2.3. Physical vapor deposition system 35
2.4. Data acquisition and process control system (DAQPCs) 38
2.5. Temperature and heat capacity calculations 43
2.6. Routine temperature calibrations 45
2.7. Validation of temperature calibrations 48
2.8. Temperature gradients and lags 53
2.9. References for Chapter Two 58
Chapter Three: Non-equilibrium melting of superheated molecular crystals 60
3.1. Overview 61
3.2. Experimental apparatus 63
3.3. Choice of polycrystalline materials and film preparation protocol 65
3.4. Thermogram analysis 66
3.5. Validating thermogram analysis 69
3.6. Melting kinetics during rapid heating 73
3.7. References for Chapter Three 83
Chapter Four: Surface-facilitated softening of ordinary and vapor-deposited glasses 88
4.1. Overview 88
4.2. Experimental 91
4.3. Thermogram analysis and results 93
4.4. Discussion 94
4.5. Summary and afterword 99
4.6. References for Chapter Four 100
Chapter Five: Relaxation mechanism of rapidly heated non-crystalline phases 103

5.1. Overview 103
5.2. Experimental technique 106
5.3. Sample preparation protocols 106
5.4. Analysis of FSC thermograms 108
5.5. Determining the Arrhenius parameters of rapid relaxation 112
5.6. Proposed mechanism of relaxation front propagation 118
5.7. Correlation between non-equilibrium relaxation rates, Z(T), and equilibrium diffusivity, D(T) 123
5.8. Summary and afterword 126
5.9. References for Chapter Five 127
Chapter Six: Insights into near-equilibrium molecular kinetics of ordinary and stable, vapor-deposited glasses from FSC experiments 133
6.1. Overview 135
6.2. Experimental details and sample preparation protocols 139
6.3. Calculating thermodynamic parameters for rapid relaxation 139
6.4. Correlation between low-temperature equilibrium self-diffusivities and self-diffusivities during high-temperature transformation 143
6.5. Insights into equilibrium molecular dynamics in stable vapor-deposited glasses with low fictive temperatures 147
6.6. Summary and afterword 155
6.7. References for Chapter Six 156
Chapter Seven: Future research directions 159
7.1. References for Chapter Seven 167

List of Figures

Fig. 1.1. Entropy of glasses and supercooled liquids (SCLs) 4

Fig. 1.2. The concept of fragility for supercooled liquids 8

Fig. 1.3. Decoupling of self-diffusion and viscosity in SCLs..... 10

Fig. 1.4. Activation energy barriers to self-diffusion and to structural relaxation in cold SCLs 12

Fig. 2.1. Fundamentals of Fast Scanning Calorimetry..... 31

Fig. 2.2. Schematic diagram of the FSC apparatus..... 33

Fig. 2.3. Diagram of the vapor deposition system for the FSC apparatus 37

Fig. 2.4. Outline of the data acquisition and process control system (DAQPC) 40

Fig. 2.5. Filament current calibration procedure..... 42

Fig. 2.6. Typical primary data collected during an FSC experiment..... 44

Fig. 2.7. Temperature calibration procedure..... 47

Fig. 2.8. Temperature calibration tests..... 51

Fig. 2.9. Rapid temperature calibration tests 54

Fig. 2.10. Temperature lags or gradients 57

Fig. 3.1. Typical analysis of the FSC thermograms of polycrystalline materials..... 67

Fig. 3.2. Validating the kinetic analysis of FSC data with vaporization endotherm analysis 71

Fig. 3.3. Zero-order kinetic rate law for melting under conditions of rapid heating 74

Fig. 3.4. Summary of the kinetic analysis and Arrhenius parameters for the melting of superheated molecular crystals 79

Fig. 3.5. The apparent activation energy barriers to dielectric structural relaxation for methyl benzene and 2-propanol 81
Fig. 4.1. Typical analysis of the FSC thermograms for glassy materials 92
Fig. 4.2. Devitrification kinetics in stable and ordinary glassy films of methyl benzene (MB)..... 95
Fig. 4.3. Devitrification rates in ordinary glassy films of MB and 2-propanol (2P) 98
Fig. 5.1. An outline of the FSC experiments with liquid MB films 105
Fig. 5.2. The sample preparation protocol for preparing well-equilibrated, ordinary liquid films..... 107
Fig. 5.3. Kinetic analysis used to derive relaxation rates from FSC thermograms of ordinary methyl-benzene liquid phases 109
Fig. 5.4. Absolute relaxation rates for three MB films with distinct fictive temperatures..... 114
Fig. 5.5. Dependence of the apparent activation energy barrier for relaxation on the sample's initial temperature 117
Fig. 5.6. The classic and modified version of the Wilson-Frenkel mechanism for front-propagated relaxation 120
Fig. 5.7. Comparing absolute relaxation rates for distinct samples..... 124
Fig. 6.1. Modified Wilson-Frankel model for front-propagated relaxation of glassy phases..... 134
Fig. 6.2. Variations in the magnitude of the thermodynamic driving force during rapid relaxation of glassy MB..... 137

Fig. 6.3. Calculating the Gibbs free energy difference between non-equilibrium and equilibrium sample phases 140

Fig. 6.4. Calculating the thermodynamic driving force of rapid relaxation for ordinary liquid MB samples 142

Fig. 6.5. The correlation between absolute relaxation rates and self-diffusion coefficients in ordinary liquid MB samples 144

Fig. 6.6. Correlation plot between non equilibrium diffusivity at the relaxation front of rapidly heated liquid MB films and the equilibrium diffusivity coefficients of MB at the samples' fictive temperatures 146

Fig. 6.7. Calculating the fictive temperatures of vapor deposited MB films from relative enthalpy diagrams 148

Fig. 6.8. FSC thermograms and relaxation rate diagrams for vapor deposited methylbenzene (MB) films 150

Fig. 6.9. Distinctions in the apparent activation energy for front propagated rapid relaxation and diffusivity at the relaxation front for ordinary liquid and vapor deposited glassy MB films 153

Fig. 7.1. Proposed experimental protocol for determining the relative transverse thermal diffusivity 163

List of Tables

Table 2.1. Crystalline organic compounds used as standards for the final validation of the temperature calibration procedure 50

Table 3.1. Properties of the compounds used in Chapter Three 64

Table 7.1. Glass-forming compounds suggested for future FSC research studies 160

List of Variables and Abbreviations

DSC.....differential scanning calorimetry

FSC .....fast scanning calorimetry

FME .....fast melting endotherm

FRE .....fast relaxation endotherm

FVE.....fast vaporization endotherm

LMW.....Low Molecular Weight compounds

OG.....ordinary glass, produced by melt-cooling and annealing

SCL .....supercooled liquid, meta-stable non-crystalline phase below T_m

SF .....surface-facilitated (transformation)

TDF .....thermodynamic driving force

VD.....vapor-deposited (condensed phase)

VFT .....Vogel-Fulcher-Tammann (Eq. 1.1)

WF.....Wilson-Frankel (transformation mechanism)

2P .....2-propanol (isopropyl alcohol), $(CH_3)_2CHOH$

DE .....diethyl ether, CH_3OCH_3

IB.....isobutane, $(CH_3)_2CHCH_3$

MB .....methyl benzene (toluene), $C_6H_5CH_3$

AI, ADC.....analog input and analog-to-digital convertor (on PCI board)

DAQPC.....Data Acquisition and Process Control system (also DAQ)

DI, DO.....digital input and digital output (on PCI board)

LN .....liquid nitrogen (heat sink)

PCI .....Peripheral Component Interconnect (for data acquisition)

RTD.....resistance temperature sensors (for TC)

SN .....signal-to-noise (ratio)

TC .....temperature controller (T_d and T_i)

L .....thickness of sample films (in μm)

η .....macroscopic shear viscosity (10^{12} Pa·s at T_g)

G_∞ .....high frequency shear modulus (a constant)

κ, $\kappa(T)$ .....thermal conductivity (in $W \cdot m^{-1} \cdot K^{-1}$)

ρ, $\rho(T)$ .....density of constituents (in $g \cdot cm^{-3}$)

R, RT .....gas constant and macroscopic energy scale factor (product of R and T)

k_B, kT .....Boltzmann constant and molecular energy scale factor (product of k_B and T)

R_t, R_s .....test resistor and sensing resistor (both at ambient temperature)

R_f, $R_f(t)$ .....measured resistance of the filament or filament-film system during FSC scans, as calculated from measured $I_f(t)$ and $V_s(t)$ values

V_t .....voltage drop across the test resistor during the current calibration procedure

$V_s(t)$, $V_f(t)$ .....voltage drop measured across sensing resistor and across the filament during FSC scans by the DAQ

I_t, $I_f(t)$ .....calculated current flow across the test resistor and the filament during scans

m_i, b_i .....current calibration parameters for calculating $I_f(t)$ from $V_s(t)$

m_T, b_T .....temperature calibration parameters (Eq. 2.1)

m_A .....fragility index of a supercooled liquid (Eq. 1.2)

T_b.....normal boiling point

T_m .....melting point or temperature of fusion

T_g .....standard glass transition temperature, the glass *hardening* temperature during melt cooling with a standard cooling rate

T_f .....fictive temperature of a glass, derived from configurational enthalpy

T_K .....Kauzmann temperature

T_d .....vapor deposition temperature (as set by temperature controller)

T_i .....initial sample temperature (immediately prior to heating)

T_{on} .....onset of transformation (approximated from C_p thermogram)

T_R .....temperature range of transformation or relaxation

T' .....test temperature, selected within the temperature range of transformation

ΔT .....degree of non-equilibrium "overheating" of configurationally frozen phase

T(t) .....measured Temperature of the filament-film system, calculated from m_T and b_T calibration parameters; i.e. the *true* temperature for the near-equilibrium liquid phase or the *vibrational* temperature for configurationally frozen phase (glass)

dT/dt, HR.....rate of temperature change or Heating Rate, calculated as the time derivative of measured *T(t)*

t_{obs} .....observational timescale of measurement (e.g. from frequency)

t_{exp} .....timescale in non-isothermal experiments (approx. 1K divided by *dT/dt*)

τ, τ_{bulk} .....microscopic structural relaxation time (Eq. 1.1 and Eq. 1.3)

τ_{surf} .....surface relaxation time (at the vacuum-sample interface)

τ_{vib} .....thermal equilibration time (Eq. 2.6)

D_{th} .....thermal diffusivity coefficient (in $m^2 \cdot s^{-1}$)

D, $D_s(T_f)$ .....compound's near-equilibrium self-diffusion coefficient at temperature T_f

d^*, $d^*(T_f)$ .....scaled self-diffusion coefficient, $D_s(T_f)$ divided by $D_s(T_g)$

D_F, $D_F(T,T_f)$....self-diffusion coefficient at the transformation front for an amorphous phase characterized by a fictive T_f, *at a higher temperature* (i.e. T greater than T_f)

d_F^*, $d^*(T,T_f)$ .....scaled front self-diffusion coefficient, $D_F(T,T_f)$ divided by $D_F(T,T_g)$

E_a, $E_a(T)$ .....apparent activation energy barrier, calculated an Arrhenius approximation for processes that involve cooperative motion (Eq. 1.6)

E_m .....activation energy barrier to melting under conditions of rapid heating

E_s, $E_{a,R}$.....energy barrier to glass softening or liquid relaxation during FSC scans

E_D, $E_{a,D}$.....energy barrier to constituent self-diffusion in equilibrium liquids (Eq. 5.5)

E_τ, $E_{\alpha d}$, $E_{a,\tau}$ .....energy barrier to structural relaxation in supercooled liquids, calculated from the dielectric α-relaxation time (Eq. 5.5)

E_{vap} .....apparent activation energy barrier to free vaporization

ΔH_{vap} .....molar enthalpy or latent heat of vaporization (endothermic)

ΔH_m .....molar enthalpy or latent heat of fusion (endothermic)

ΔH_{ex}.....*average* molar enthalpy change of transformation (e.g. relaxation)

$\Delta\mu$.....chemical potential difference between the transforming phases

ΔG,$\Delta G(T,T_f)$ ...Gibbs free energy difference between the transforming phases, calculated at some test temperature, T, greater than the fictive temperature, T_f, of the initial sample; used to derive the thermodynamic driving force for relaxation (see Eq. 6.1 and Eq. 6.5)

dQ/dt .....rate of heat generation (power) by the filament during FSC scans (Eq. 2.2)

C .....*unscaled* heat capacity of a sample (*not* molar or specific heat capacity)

$C_{p,a}$, $C_{p,a}(T)$.....measured thermogram or apparent heat capacity of a sample film (Eq. 2.5)

C_p, $C_p(T)$.....true heat capacity of a rapidly transforming sample film (Eq. 5.2)

$C_{p,s}$, $C_{p,l}$ .....heat capacity of the sample in its fully "solid" and "liquid" states (Eq. 5.2)

ΔC_p^{lg} .....*molar* heat capacity *difference* between the fully "glassy" and fully "liquid" states of the sample film (Eq. 6.5)

χ, $\chi(T)$.....dimensionless extent of transformation (Eq. 5.1)

$H(T)$ .....relative enthalpy of the sample film, temperature integral of $C_{p,a}(T)$

H_s, H_l.....relative enthalpies of the film in its fully "solid" and "liquid" states (Eq. 5.1)

$(dH/dT)_{ex}$ ....."excess" heat capacity during endothermic transformation, calculated as the difference between apparent $C_{p,a}(T)$ and true $C_p(T)$ (Eq. 5.2)

$(dH/dt)_{ex}$ ....."excess" heat flow *rate* during endothermic transformation, calculated as a product of $(dH/dT)_{ex}$ and heating rate dT/dt (Eq. 4.1)

$Z(T)$, $Z(T,T_f)$ ...rate of rapid relaxation during FSC scans (Eq. 5.4), at some higher temperature, T, for samples characterized by an initial fictive temperature of T_f, i.e. the flux of constituents across the transformation front

z^*, $z^*(T,T_f)$ .....scaled transformation rate, $z(T,T_f)$ divided by $z(T,T_g)$

ϑ_f, υ_m .....front velocity of transformation (in mm/s)

N.....number of "transformed" constituents

dN/dt .....transformation rate (constituents per second)

$k(T)$ .....transformation rate coefficient

A_f .....surface area of the transformation front (approx. equal to film surface area)

Chapter One: Introduction

1.1. An overview

Understanding the behavior of materials far from equilibrium is important for a broad range of scientific fields and emerging technologies. Many unanswered questions in chemistry and physics involve systems that are out of equilibrium, from amorphous water in deep space to biological organisms[1]. The instances, which give rise to non-equilibrium, include: the melting of superheated crystals, crystallization of deeply supercooled liquids, or their hardening into non-crystalline, glassy phases[2]. Although, in all cases, a fundamental understanding of these non-equilibrium processes is far from complete, the glass transition represents a particularly enduring challenge in the field of modern condensed matter physics[3-7].

Glasses, which lack the reproducible unit cell that defines crystalline solids[8], are the most common amorphous solid material in both manufacturing and the natural world. They can vary in chemical composition from organic glasses such as sucrose candy to inorganic silicates to typical polymer plastics like poly-methyl methacrylate. Glasses are used ubiquitously in architecture, the automobile industry, pharmacology, telecommunications, and artistic expression[9]. Recent advances in glassy materials include amorphous medicinal compounds[10], metallic glass power conduits,[11] and highly efficient light emitting diodes.[12] In short, glassy materials and the liquids that form them are an important area of research for any applications where crystalline features such as facets, grain boundaries, and defects are not desired.

Yet, despite tremendous research effort and the ubiquitous use of glasses, there is still no accepted theory of glass formation that has predictive powers with respect to a glass's final properties[6, 13]. Before addressing the current theoretical and experimental challenges in the field of glass science, it is necessary to provide some basic definitions and describe the general phenomenology used in the field.

1.2. Distinctions between glasses and liquids

A glass is generally known as the physical state of condensed matter having the extrinsic properties of a solid but the intrinsic properties of a liquid[14]. This amorphous solid has an immeasurably high shear viscosity, η, yet a surprisingly high molecular diffusivity. The most common method[15] for forming an ordinary glassy phase is by cooling a liquid below its melting point, T_m, to a characteristic temperature range known as the kinetic glass *hardening* transition. Deeply supercooled liquids (SCL) below T_m are meta-stable[16] with respect to the crystalline phase and exist because constituents in the liquid suffer from a kinetic slow-down that allows them insufficient time to overcome the energy barriers to forming crystalline nuclei[2]. In essence, as temperatures decrease significantly below T_m, the transition of the *equilibrium isotropic* liquid phase into crystalline grains becomes virtually impossible[2] and results in a *non-equilibrium and amorphous* glassy phase, which is typically isotropic[17-18]. This "solid" glass is subject to aging, i.e. annealing, as its structure *slowly* relaxes towards an equilibrium thermodynamic state[19,2, 18]. The most recent formal definition of a glass is as follows[20]:

"Glass is a non-equilibrium, non-crystalline condensed state of matter that exhibits a glass transition. The structure of glasses is similar to that of their parent supercooled liquids, and they spontaneously relax toward the supercooled liquid state. Their ultimate fate, in the limit of infinite time, is to crystallize." – Zanotto & Mauro, 2017

1.3. Characteristic temperatures: T_g and T_f

The process of glass formation, described in the preceding paragraph, is characterized by several basic parameters. One of these is the *standard* onset temperature of glass hardening[20], T_g. Fig. 1.1 illustrates the entropic changes for a condensed phase cooled below its melting point. When the liquid is cooled sufficiently slowly, it may remain in a quasi-equilibrium state at temperatures significantly below T_m. During progressive cooling, however, a limiting temperature is always reached where the liquid can no longer equilibrate on the timescale of the experiment[15]. This particular temperature depends on the cooling rate, which determines the experimental observational time, t_{obs}, calculated as 1 Kelvin divided by the rate of temperature change[15]. In fact, the standard T_g is often defined[15] as the temperature at which the liquid falls out of equilibrium when the cooling rate is 1 $K \cdot min^{-1}$. Consequently, the t_{obs} for a standard glass is approximately 10^2 seconds.

From the standpoint of statistical thermodynamics, the deviation from equilibrium at T_g represents a loss of variations in the configurational degrees of freedom for the liquid particles[21]. As shown in Fig. 1.1, upon further cooling, the only change in the entropy of the system arises from its vibrational contributions, similar to the entropic changes in crystalline materials. This "freezing" of configurational dynamics negates the concept of true temperature for the non-equilibrium system[22]. Therefore, a fictive temperature

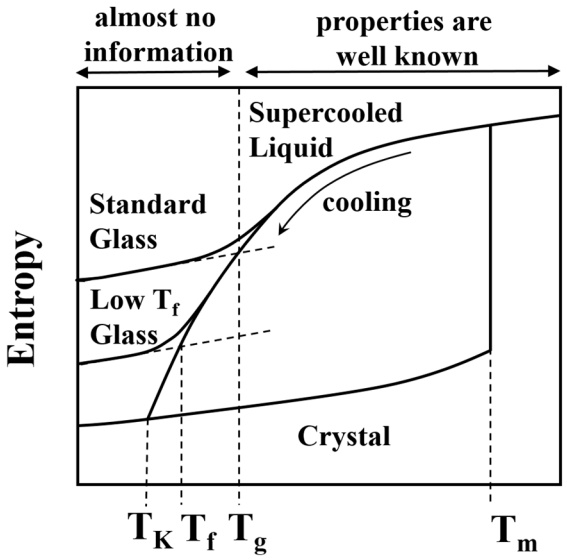

Fig. 1.1. Entropy of glasses and supercooled liquids (SCLs)**.** Illustration of the thermodynamic properties, e.g. **entropy**, of **glasses** and **supercooled liquids (SCL)** for temperatures below the melting point, $\mathbf{T_m}$. A **standard glass:** amorphous phase formed by cooling a SCL with the rate of approximately 1K/min. $\mathbf{T_g}$**:** standard glass transition temperature equal to the fictive temperature, $\mathbf{T_f}$, of a glass prepared with the "standard" cooling rate. **Low $\mathbf{T_f}$ glass:** a high stability glass prepared by slower cooling, by annealing, or by vapor-deposition. $\mathbf{T_K}$**:** the Kauzmann temperature at which the entropy of a SCL may (hypothesized) become equal to the entropy of the **crystal**. Note that similar diagrams may be drawn for other thermodynamic parameters such as configurational enthalpy or molar volume.

concept[15] is often invoked to relate the thermodynamic and structural properties of the non-equilibrium glass to a similar state of the equilibrium liquid. For example, the fictive temperature, T_f, for a liquid cooled with a rate of 1 $K \cdot min^{-1}$ is equal to the standard T_g. As illustrated by Fig. 1.1, the T_f of a glass formed by cooling with a *lower* heating rate can be *lower* than T_g. Note that the T_f can also exceed T_g, for glasses prepared by more rapid quench cooling. Also note that the T_f of any glass can be lowered by annealing at low temperatures. In summary, T_f represents a useful parameter for describing the sample's thermal history. It may also prove predictive for the behavior of glassy samples during heating[15], i.e. softening or devitrification.

As shown in Fig. 1.1, extrapolating the entropy of a quasi-equilibrium supercooled liquid toward exceedingly low temperatures may result in a disordered liquid with an entropy lower than that of an ordered crystalline phase. This controversial hypothesis is known in the field as Kauzmann's entropy crisis[23]. The temperature at which the paradox is predicted is referred to as the Kauzmann temperature, T_K. Although the very existence of this singular temperature is now deemed questionable[24], T_K is still an important parameter in empirical descriptions of the amorphous material's molecular kinetics near T_g and the phenomenon of liquid fragility, discussed immediately below.

1.4. Kinetic parameters and fragility

Upon glass hardening, the system's deviation from equilibrium *thermodynamic* parameters, e.g. entropy, enthalpy, or free volume, is radically reflected by a rapid drop in the liquid's molecular kinetics[25]. Depending on the experimental probe, one of three fundamental physical parameters can be used to characterize the kinetic slowdown, i.e. liquid "hardening" into glass: viscosity, self-diffusivity, or microscopic relaxation time

(η, D, τ). As discussed in the next Section (1.5), the temperature variations in these three parameters typically correlate[26] closely with each other; i.e. $\eta \sim D^{-1} \sim \tau$. While bulk shear viscosity and long-range translational self-diffusivity are concepts used widely in physics and chemistry, the microscopic relaxation time is a concept unique to glass sciences.

Typically, this *microscopic structural* relaxation time, τ, is defined as the average time for a molecular structure that is out of equilibrium (glassy) to return to its equilibrium state (liquid)[15]. Under constant pressure, the relaxation τ can be probed by small perturbations (e.g. heat) to the sample while measuring the temporal response of an extrinsic property (e.g. enthalpy). Techniques such as broadband dielectric spectroscopy[27-28] can probe and measure the average structural relaxation time for a bulk sample[22]. Note that the current consensus in the field is that the relaxation times measured by both structural and enthalpic techniques are equivalent[15]. From its definition, a glass with a fictive temperature of T_g has a relaxation time τ of 10^2 s, equal to the experimental observation time. Thus, the ratio of τ to t_{obs}, colloquially known as the Deborah criterion[15], is unity at T_g.

The *structural* relaxation of a glass's non-equilibrium configuration towards equilibrium that follows a complex (non-linear and non-exponential) function of time under isothermal conditions[9, 15]. More importantly, the temperature dependence of τ in supercooled liquids is non-Arrhenius. In fact, the best empirical fit of the available relaxation time data is by the Vogel-Fulcher-Tammann (VFT) equation[15]:

$$\tau(T) = \tau_0 \cdot \exp\left(\frac{B}{T - T_0}\right), \quad (1.1)$$

where τ_0 and B are temperature independent parameters. Remarkably, T_0 is typically quite close to the Kauzmann temperature[22], T_K, discussed in Section 1.3. In fact, the

mathematical form of Eq. 1.1 provides the best fit for the temperature dependence of both viscosity and diffusivity, though the fit parameters (B, T_0) for these distinct kinetic variables are different. Despite these differences (as illustrated in Fig. 1.2), all three kinetic parameters (η, D, τ) are expected to diverge rapidly at temperatures below T_g.

Fig 1.2 also shows the two extremes of mobility behavior in supercooled liquids. The deviation of kinetic parameters from an Arrhenius temperature dependence in supercooled liquids is quantitatively characterized by the liquid's fragility index, m_A. Angell and coworkers[29] developed a mathematical model to quantify this deviation:

$$m_A \equiv \left| \frac{d \log \tau}{d\left(T_g/T\right)} \right|_{T=T_g} . \quad (1.2)$$

Note that the m_A parameter is defined at temperatures equal to the standard Tg. In Fig 1.2, the m_A parameter is near 16 for strong Arrhenius-like liquids[29], and can approach a value as high as 170, in the case of extremely fragile liquids[30-31]. The fragility index is understood to reflect the extent of cooperative motion for constituent mobility in supercooled liquids, and interestingly, cannot be predicted by the temperature dependence of structural properties such as density[9].

1.5. The unique temperature dependence of diffusivity

In the previous Section (1.4), I mentioned that the kinetic parameters, e.g. viscosity and self-diffusivity, of a cold amorphous phase correlate well in a broad temperature range. The observed correlation, however, is stronger[32] between viscosity and relaxation time than between diffusivity and the other two parameters. The relationship between viscosity and the relaxation time is set by the high frequency shear modulus, G_∞, a constant that is

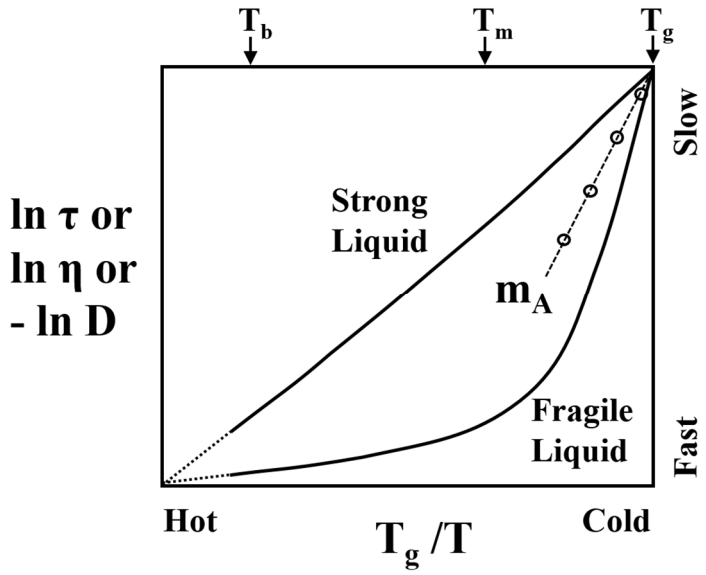

Fig. 1.2. The concept of fragility for supercooled liquids**.** Illustration of the fragility concept in **supercooled *liquids* (SCL)**. Note that the relaxation time, **τ**, is typically plotted in Arrhenius coordinates, as a natural log of τ versus a scaled inverse temperature, $\mathbf{T_g/T}$. **Strong liquids** approach an Arrhenius-like dependence (linear) in their mobility parameters (**η, D, or τ**), whereas **fragile liquids** have a super-Arrhenius dependence. The temperature dependence of their mobility parameters at high temperatures ($\mathbf{T_b}$ to $\mathbf{T_m}$) and at low temperatures ($\mathbf{T_m}$ to $\mathbf{T_g}$) differ *drastically* for fragile *liquids*. The degree of deviation is measured by the fragility parameter, $\mathbf{m_A}$**.** See text for details.

approximately 10^{10} Pa for condensed phases[33]. The relationship is defined as[15]:

$$\eta \coloneqq \tau \cdot G_{\infty}. \quad (1.3)$$

Historically[26], the relationship between D and η is given by the Stokes-Einstein equation:

$$D \approx \frac{k_B}{6\pi r} \cdot \frac{T}{\eta}, \quad (1.4)$$

where k_B is the Boltzmann constant and r is the molecular radius of constituents. This relation was established for low viscosity equilibrium liquids (between T_m and T_b).

Although macroscopic viscosity and microscopic relaxation time are proportional in a supercooled liquid's entire temperature range from T_m to T_g, the self-diffusivity[34] has been shown to deviate[2] from τ and η at temperatures near $1.4 \cdot T_g$. The deviation is illustrated in Fig. 1.3 using a relatively fragile glass-forming liquid. For many supercooled liquids, at temperatures *below* $1.4 \cdot T_g$, the long-range translational self-diffusivity values are *higher* than predicted by a direct application of Eq. 1.4 to either τ or η data.

The decoupling of self-diffusivity from relaxation time at low temperatures can be confirmed by the following analysis. A mathematically equivalent expression to the VFT equation (Eq. 1.1), has an Arrhenius-like temperature dependence and utilizes a temperature-dependent activation energy:

$$\tau(T) = \tau_0 \cdot \exp\left(\frac{B}{T - T_0}\right) = \tau_0 \cdot \exp\left(\frac{E_a(T)}{RT}\right). \quad (1.5)$$

From this approximation of relaxation time data, we can calculate the *apparent* activation energy barrier, E_a, at each temperature:

$$E_a(T) = R \cdot \frac{d(\ln \tau)}{d(1/T)}, \quad (1.6)$$

where R is the gas constant. A similar treatment can be used to calculate the *apparent*

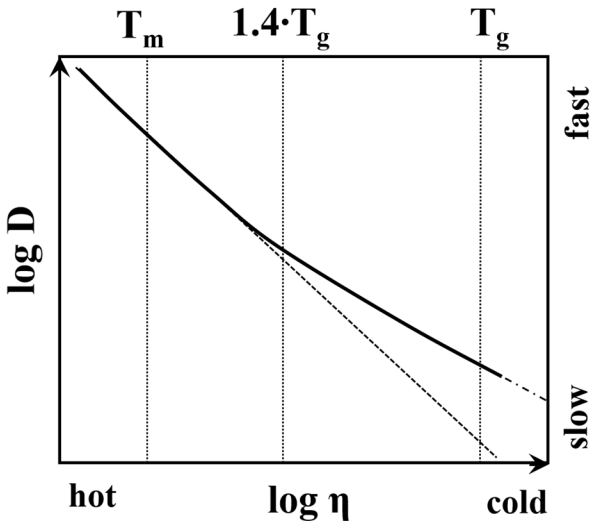

Fig. 1.3. Decoupling of self-diffusion and viscosity in SCLs. Illustration of the Stokes-Einstein breakdown for a relatively fragile supercooled liquid. Black line shows the low-temperature decoupling of self-diffusion (**D**) and viscosity(**η**). At high temperatures, diffusivity and viscosity follow Eq. 1.4 (dash-dotted line). However, at temperatures below approximately **1.4·Tg**, the correlation (dashed line) between these mobility parameters is lost. See text for details.

activation energy barrier for near-equilibrium self-diffusion. As shown in Fig. 1.4, the decoupling of the self-diffusivity from relaxation time is manifested by a *weaker* temperature dependence of diffusivity's E_a. Furthermore, at T_g, the fragility index from self-diffusivity data and the m_A calculated from relaxation time data are expected to differ.

The decoupling of diffusivity from relaxation time and viscosity, also known as the breakdown of the Stokes-Einstein dependence, is often attributed to the emergence of heterogeneity[35-37] in supercooled liquids as the temperature decreases toward T_g. The phenomenon is discussed in the next Section.

1.6. Dynamic heterogeneities in deeply supercooled liquids

Simulations and some microscopic techniques have detected regional variations of molecular dynamics in the bulk of both supercooled liquids and glasses[38] . These experiments detect regions that have faster dynamics and regions that have slower dynamics; this phenomenon is termed dynamic heterogeneity[16] (see Fig. 3 in Ref. [38]). These dynamic heterogeneities do not appear to be from kinetic fluctuations; instead, they resemble solid state defects resulting from local features of constituent configurations[9]. However, the origin of these "defects", the characteristic average length scale of the regions, and the fluctuation in the heterogeneities with time are all outstanding research questions[9]. The tentative consensus in the field is that there are *unquantifiable* structural differences in the dynamically distinct regions of the bulk. This tentative position is understandable, as all amorphous materials have a quasi-random constituent arrangement that is already hard to quantify. The experimental challenges of resolving this and other fundamental questions in glass science is explored in the next Section.

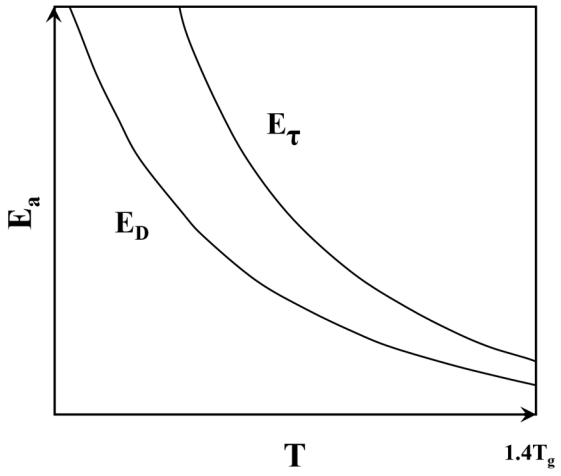

Fig. 1.4. Activation energy barriers to self-diffusion and to structural relaxation in cold SCLs. Illustration of the temperature dependence of the apparent energy of activation (**E_a**) for both self-diffusion (**D**) and dielectric relaxation time (**τ**) below approximately **$1.4 \cdot T_g$**. The example values were calculated using Eq. 1.6 for a relatively fragile supercooled liquid (methyl benzene).

1.7. Two-fold problem of glass science: time[2]

Historically, the key approach to elucidating structural and physical properties of glasses relied on studies[39] of their parent supercooled liquids at temperatures *above* T_g. These experiments yielded an immense array of data, such as dielectric relaxation times, self-diffusivity, viscosity, heat capacity, density, and optical properties. Unfortunately, these measurements did not translate into a comprehensive, universally accepted theory of glass formation. In fact, the overwhelming array of data produce fertile ground for a multitude of incredibly sophisticated theories, all of which fit the existing data well despite their use of profoundly opposing physical principles[40]. The most recent examples of such drastically distinct models are the random first order transition theory[5] and the kinetically constraint models[41]. These theories are based on different hypotheses for the microscopic mobility behavior near T_g. Some rely on an underlying (unattainable) phase transition and some on frustration or jamming of structure[8, 13]. All lack robustness by their use of empirical scaling to accommodate existing data, and none have predictive power with respect to new data[13].

This impasse in developing a comprehensive, non-controversial, universal description of the glass transition phenomenon has precipitated a drive toward developing novel experimental techniques[8]. These methods focus on interrogating the complex structural variations of supercooled liquids and glasses under a variety of conditions[9, 42]. Examples include *microscopic* imaging investigations of colloids and *macroscopic* studies of the jamming transition in flowing granular media[4, 43]. Although these state-of-the art experiments provided important insights, they are only relevant to the behavior and structure of *molecular or atomic* phases at temperatures significantly *above* T_g. As such,

studies of structure and dynamics in amorphous materials at temperatures at and below T_g are still needed to resolve theoretical disputes[7].

As described in Section 1.4, the obvious challenge for research of glassy materials is the observational time, t_{obs}. The glassy samples must be made and measured on human timescales. Yet, even a few degrees below T_g, the relaxation time of a glass approaches geological timescales. Consequently, measurements of dynamic parameters such as dielectric relaxation times[27] or self-diffusion coefficients[44] significantly below T_g are nigh-on-impossible. In fact, many predictions of glassy theories are often considered to be *untestable*[13, 45]. For example[5], random first order transition theory predicts a discontinuous phase transition with diverging length scales at temperatures tens of K below T_g. Given the time-scale at this temperature, this first-order-like transition cannot be verified or denied by current experimental techniques.

The problem of time in experiments with glasses and deeply supercooled liquids is two-fold: sample preparation time and measurement observation time. First, the traditional approach to glass preparation, slow cooling, requires progressively lengthier intervals of time for samples with fictive temperatures below T_g. As postulated by Eq. 1.1 and the Deborah criterion, τ and t_{obs} grow exponentially at temperatures approaching T_g, and sample preparation time can quickly exceed days and years. Second, if these stable amorphous samples can be produced, probing the time response of progressively slower mobility parameters becomes experimentally unfeasible, i.e. t_{obs} is too long. Again, as the temperatures drop, the timescale of τ, as predicted by Eq. 1.1, quickly exceeds days and years. Therefore, it is unsurprising that decades of ardent experimental effort have yielded few data below T_g.

1.8. Faster sample preparation by vapor deposition

Thankfully, there appears to be a solution to the problem of sample preparation time. Advances in vacuum technologies and careful study have led to an alternative method of forming highly stable amorphous materials, one that is orders of magnitude faster than melt cooling. Physical vapor deposition (VD) on virtually any cold substrate can be used to produce multilayer, amorphous films from a medley of distinct chemical compounds, even from materials that do not form glasses during melt cooling due to low barriers of crystal nucleation[9, 15, 25, 46]. Unlike the traditional glass preparation techniques, vapor deposition of glasses takes advantage of the incredibly high rates of constituent diffusion along the surface of the growing sample[47-48]. At temperatures that allow condensation, the time for surface diffusion is orders of magnitude shorter than the bulk relaxation time. In fact, the time ratio of surface to bulk diffusion grows rapidly as temperatures drop and can exceed 10^6 for some compounds[48] near T_g. Thus, the high molecular mobility at the vapor-glass interface[47-48] makes it possible for condensing constituents to find configurations with the lowest potential energy on the experimental time scale. In fact, at deposition temperatures, T_d, below the glass transition, vapor deposition can produce amorphous glassy films with remarkably high kinetic stability and low enthalpy[21, 49-67].

Early reports on stable VD glasses argued that the formation of these phases is possible only at a well-defined "critical temperature" (e.g. $0.86 \cdot T_g$)[49]. This interpretation of early experiments, however, was in contrast to the classical view of surface science[68], where molecular or atomic beam epitaxy was used to produce both crystalline *and amorphous* films for many decades. These studies, in combination with computer simulations and theoretical deposition models[68-72], demonstrated that the Deborah criterion

still applies during physical vapor deposition of amorphous phases. In other words, the experimental time is of equal importance to the deposition temperature. In fact, the primary controlling parameter for the formation of a layered film with a highly stable microscopic structure is the *ratio* of the surface diffusion rate to the deposition flux. Unsurprisingly, later experiments found that, even when deposition temperatures did not equal $0.86 \cdot T_g$, amorphous VD films still display the unique physical attributes of stable glasses[60, 63-65].

Although a vigorous debate on the nature and formation mechanisms of non-crystalline VD phases continues, experiments and simulations have already derived several important conclusions. Unequivocally, vapor deposition does not result in a singular "super-stable" or "ideal" glassy phase. To the contrary, depending on the deposition conditions (T_d and F_d), the technique can produce a *continuum* of glassy samples with distinct kinetic stabilities[65, 73-74]. In other words, by fine tuning the deposition flux and the substrate temperature, physical vapor deposition can be used to prepare glassy samples with a *continuum* of fictive temperatures, perhaps as low as T_K. Additionally, although certain compounds and deposition conditions may produce amorphous samples with structure and thermodynamic properties distinct from those of ordinary glass phases[21, 47-49, 55-58, 75-87], the use of alternative materials and deposition protocols may still result in amorphous phases that are indistinguishably similar to ordinary glasses.

In summary, physical vapor deposition takes advantage of fast surface diffusion and makes it possible to prepare low T_f "ordinary" glassy samples (see Fig 1.1) on a time scale of only hours or even minutes.

1.9. Impediments to measurements: observation time

Despite the unique ability of the vapor deposition technique to facilitate the rapid

preparation of low fictive temperature glasses, its use has not produced definitive results that credit a particular theory of glass transition. To a large extent, the continued impasse is due to the limitations of standard analytical techniques for probing thermodynamic, kinetic, and structural parameters in glasses. In effect, solving the first problem of time in glass science does not address the second problem of time. Independent of the probing technique, observing slow dynamics requires lengthy observation times, t_{obs}. The examples in this Section illustrate the scope of the problem.

A number of techniques allow *direct* determination of mobility parameters for materials at temperatures above T_g. Microscopic relaxation time and self-diffusion are accurately measured by broadband dielectric spectroscopy[28] and nuclear magnetic resonance experiments, respectively. However, when the relaxation time for samples below T_g exceeds 10^2 s, instrumental limitations make these techniques unsuitable. Even diffusion measurements by mass spectroscopy, such as noble gas permeation[73, 88], cannot bypass the exceedingly long t_{obs} of materials near T_g. Again, these techniques are quite capable of characterizing microscopic dynamics in bulk-like films *above* T_g. However, even reducing the diffusion length by utilizing nanoscale films does not significantly reduce the long experimental times needed to measure self-diffusion coefficients in glassy samples.

An alternative approach was pursued by *structural* studies of glasses and supercooled liquids. It is generally understood that time and length scales in thermodynamic systems are intrinsically related[15]. Structural characterization techniques[89], such as microscopy[90] or neutron[91] and X-ray scattering[92], can be used to probe the length scale of microscopic variations in SCL, ordinary glasses, and VD glasses. Yet each

technique lacks sufficient resolution and lacks a clear criterion for discerning subtle structural variations in amorphous materials, particularly at temperatures near T_g. This is exemplified by the demonstration of only dynamic, not structural, heterogeneities in deeply supercooled liquids[36] (see Section 1.6).

In addition to microscopic studies, highly accurate measurements of ensemble average properties such as specific volume and specific heat capacity were achieved, yet these studies were not particularly informative. Glassy materials are notorious for the fundamentally "weak" coupling between their thermodynamic and kinetic parameters [9, 15, 25]. An example, illustrated by Fig. 14 of Ref. [93], shows how minor changes of a few percent in macroscopic thermodynamic variables are accompanied by tremendous changes in microscopic kinetic parameters such as τ or D. Therefore, near-equilibrium techniques such as differential scanning calorimetry (DSC) and alternating current calorimetry can only *qualitatively*[61, 94-97] compare the kinetic stabilities of distinct glasses using the characteristic onset temperature of softening, T_{on}. However, the connection between T_{on} and the actual microscopic kinetics is as unclear as the connection between the relaxation time kinetics and other thermodynamic parameters[15].

1.10. Fast Scanning Calorimetry (FSC): a path for transformative research on the glass transition

A new and capable technique, Fast Scanning Calorimetry (FSC), was introduced in the last decade and quickly gained popularity among a diverse group of researchers. The rapid development of FSC-based experimental methods was epitomized by the release of a book[98] with the same tile by Springer in 2016. In addition to a thorough discussion of FSC basics, the treatise also describes a variety of innovative FSC applications in research

on condensed systems ranging from metallic glasses to polymers. However, despite its rapidly expanding applications, the full potential of FSC has not yet been realized in *fundamental* studies of the glass transition and related phenomena. This negligence likely results from a historically limited perception of the method.

Originally, fast scanning calorimetry methods that utilized heating rate on the order of 10,000 $K \cdot s^{-1}$ were developed to model technical production processes such as melt casting[98]. In other words, for historical reasons, there is a perception that the FSC technique is only suitable for studies of "fast" processes, such as crystallization of supercooled polymer melts. Additionally, since its development in industry, the heating rates currently employed in FSC studies rarely exceed 40,000 $K \cdot s^{-1}$. The reason for imposing this arbitrary heating rate is, ostensibly, to avoid thermal lags[98]. Although this is a valid concern, particularly in DSC experiments with large bulk samples on the order of several grams, it appears overly exaggerated for smaller samples on the order of a microgram. Indeed, for micrometer-scale films, it is possible to minimize temperature gradients to below 1K and accurately measure the temperature of samples heated with rates of up to $10^6 K \cdot s^{-1}$.

In addition to maintaining an arbitrary boundary on heating rate, current applications of FSC are also limited by an incorrect perception about thermogram complexity. The heat capacity thermograms measured by FSC have been considered, as with traditional DSC, to contain endo- or exotherms that are "too complex and convoluted". As with the DSC technique, the analysis of FSC thermograms is reduced to inferring the characteristic T_{on} of rapid processes as a function of the sample's heating rate or thermal history. Thus, past FSC studies failed to provide useful information on transformation kinetics under non-isothermal conditions.

1.11. Dissertation objectives

In this Dissertation, I describe experiments which demonstrate that the Fast Scanning Calorimetry technique is perfectly capable of overcoming the artificial limitations described in the preceding paragraphs. My approach is based on a remarkable, highly transformative discovery that, in the limit of high heating rates (in excess of 10^5 K/s), the kinetics of virtually *any transition* (glass devitrification, viscous liquid relaxation, and crystal melting) simplify to a zero-order, Arrhenius-like rate law. Furthermore, I demonstrate that, in the case of quasi-equilibrium liquids and non-equilibrium glasses, the simplified kinetics are defined primarily by the *initial* structural state of the sample.

The first objective of my studies was to improve the understanding of the glass devitrification mechanism under conditions of rapid heating. My second objective was to gain insights into slow molecular kinetics in the sub-T_g region for model glassformers. Thus, my studies focus specifically on the fundamentals of the glass transition and related phenomena. The approach is aimed to address both time-scale problems in glassy materials: sample preparation time and measurement observation time.

1.12. References for Chapter One

1. Ornes, S., Core Concept: How nonequilibrium thermodynamics speaks to the mystery of life. *Proc. Natl. Acad. Sci. U. S. A.* **2017,** *114* (3), 423-424.

2. Debenedetti, P. G.; Stillinger, F. H., Supercooled liquids and the glass transition. *Nature* **2001,** *410* (6825), 259-267.

3. Smarajit, K.; Chandan, D.; Srikanth, S., Length scales in glass-forming liquids and related systems: a review. *Reports on Progress in Physics* **2016,** *79* (1), 016601.

4. Gokhale, S.; Sood, A. K.; Ganapathy, R., Deconstructing the glass transition through critical experiments on colloids. *Advances in Physics* **2016,** *65* (4), 363-452.

5. Kirkpatrick, T. R.; Thirumalai, D., Colloquium: Random first order transition theory concepts in biology and physics. *Rev. Mod. Phys.* **2015,** *87* (1), 183-209.

6. Langer, J. S., Theories of glass formation and the glass transition. *Reports on Progress in Physics* **2014,** *77* (4), 042501.

7. McKenna, G. B.; Simon, S. L., 50th Anniversary Perspective: Challenges in the Dynamics and Kinetics of Glass-Forming Polymers. *Macromolecules* **2017,** *50* (17), 6333-6361.

8. Wolynes, P. G.; Lubchenko, V., Structural Glasses and Supercooled Liquids : Theory, Experiment, and Applications. 1 ed.; Wiley: Hoboken, NJ, 2012.

9. Ediger, M. D.; Harrowell, P., Perspective: Supercooled liquids and glasses. *The Journal of Chemical Physics* **2012,** *137* (8).

10. Becker, K.; Salar-Behzadi, S.; Zimmer, A., Solvent-Free Melting Techniques for the Preparation of Lipid-Based Solid Oral Formulations. *Pharm Res* **2015,** *32* (5), 1519-1545.

11. Ramanan, V. R. V., Metallic glasses in distribution transformer applications: An update. *J. Mater. Eng.* **2013,** *13* (2), 119-127.

12. Forrest, S. R.; Thompson, M. E., Introduction: Organic Electronics and Optoelectronics. *Chemical Reviews* **2007,** *107* (4), 923-925.

13. Tarjus, G., An overview of the theories of the glass transition. In *Dynamical Heterogeneities in Glasses, Colloids, and Granular Media*, Berthier, L.; Biroli, G.; Bouchaud, J. P.; Cipelletti, L.; Van Saarloos, W., Eds. OUP Oxford: 2011; pp 39-67.

14. Kolb, D.; Kolb, K. E., The chemistry of glass. *Journal of Chemical Education* **1979,** *56* (9), 604.

15. Hodge, I. M., Enthalpy relaxation and recovery in amorphous materials. *Journal of Non-Crystalline Solids* **1994,** *169* (3), 211-266.

16. Ediger, M. D.; Angell, C. A.; Nagel, S. R., Supercooled Liquids and Glasses. *The Journal of Physical Chemistry* **1996,** *100* (31), 13200-13212.

17. Krause, D., Glasses. In *Springer Handbook of Condensed Matter and Materials Data*, Martienssen, W.; Warlimont, H., Eds. Springer Berlin Heidelberg: 2005; pp 523-574.

18. Franken, P. A.; Hill, A. E.; Peters, C. W.; Weinreich, G., Generation of Optical Harmonics. *Phys. Rev. Lett.* **1961,** *7* (4), 118-119.

19. Corberi, F.; Cugliadolo, L. F.; Yoshino, H., Growing Length Scales in Aging Systems. In *Dynamical Heterogeneities in Glasses, Colloids, and Granular Media*, Berthier, L.; Biroli, G.; Bouchaud, J. P.; Cipelletti, L.; Van Saarloos, W., Eds. OUP Oxford: 2011; pp 370-401.

20. Zanotto, E. D.; Mauro, J. C., The glassy state of matter: Its definition and ultimate fate. *Journal of Non-Crystalline Solids* **2017,** *471*, 490-495.

21. Ramos, S.; Oguni, M.; Ishii, K.; Nakayama, H., Character of Devitrification, Viewed from Enthalpic Paths, of the Vapor-Deposited Ethylbenzene Glasses. *J. Phys. Chem. B* **2011,** *115* (49), 14327-14332.

22. Angell, C. A.; Ngai, K. L.; McKenna, G. B.; McMillan, P. F.; Martin, S. W., Relaxation in glassforming liquids and amorphous solids. *J. Appl. Phys.* **2000,** *88* (6), 3113-3157.

23. Kauzmann, W., The Nature of the Glassy State and the Behavior of Liquids at Low Temperatures. *Chemical Reviews* **1948,** *43* (2), 219-256.

24. Stillinger, F. H.; Debenedetti, P. G., Glass Transition Thermodynamics and Kinetics. In *Annual Review of Condensed Matter Physics, Vol 4*, Langer, J. S., Ed. Annual Reviews: Palo Alto, 2013; Vol. 4, pp 263-285.

25. Debenedetti, P. G.; Truskett, T. M.; Lewis, C. P.; Stillinger, F. H., Theory of supercooled liquids and glasses: Energy landscape and statistical geometry perspectives. In *Advances in Chemical Engineering*, Academic Press: 2001; Vol. Volume 28, pp 21-79.

26. Shi, Z.; Debenedetti, P. G.; Stillinger, F. H., Relaxation processes in liquids: Variations on a theme by Stokes and Einstein. *Journal of Chemical Physics* **2013,** *138* (12).

27. Kaatze, U., Measuring the dielectric properties of materials. Ninety-year development from low-frequency techniques to broadband spectroscopy and high-frequency imaging. *Measurement Science & Technology* **2013,** *24* (1).

28. Vassilikou-Dova, A.; Kalogeras, I. M., Dielectric Analysis (DEA). In *Thermal Analysis of Polymers*, John Wiley & Sons, Inc.: 2008; pp 497-613.

29. Böhmer, R.; Ngai, K. L.; Angell, C. A.; Plazek, D. J., Nonexponential relaxations in strong and fragile glass formers. *The Journal of Chemical Physics* **1993,** *99* (5), 4201.

30. Wang, L. M.; Velikov, V.; Angell, C. A., Direct determination of kinetic fragility indices of glassforming liquids by differential scanning calorimetry: Kinetic versus thermodynamic fragilities. *Journal of Chemical Physics* **2002,** *117* (22), 10184-10192.

31. Wang, L. M.; Angell, C. A.; Richert, R., Fragility and thermodynamics in nonpolymeric glass-forming liquids. *J Chem Phys* **2006,** *125* (7), 074505.

32. Stillinger, F. H., Relaxation and flow mechanisms in ‘‘fragile’’ glass-forming liquids. *The Journal of Chemical Physics* **1988,** *89* (10), 6461-6469.

33. Luning Prak, D. J.; Cowart, J. S.; McDaniel, A. M.; Trulove, P. C., Density, Viscosity, Speed of Sound, Bulk Modulus, Surface Tension, and Flash Point of Binary Mixtures ofn-Hexadecane + Ethylbenzene or + Toluene at (293.15 to 373.15) K and 0.1 MPa. *Journal of Chemical & Engineering Data* **2014,** *59* (11), 3571-3585.

34. Brodin, A.; Börjesson, L.; Engberg, D.; Torell, L.; Sokolov, A., Relaxational and vibrational dynamics in the glass-transition range of a strong glass former B 2 O 3. *Phys. Rev. B* **1996,** *53* (17), 11511.

35. Kim, K.; Saito, S., Multiple length and time scales of dynamic heterogeneities in model glass-forming liquids: a systematic analysis of multi-point and multi-time correlations. *J Chem Phys* **2013,** *138* (12), 12A506.

36. Berthier, L.; Biroli, G.; Bouchaud, J. P.; Jack, R. L., Overview of Different Characterizations of Dynamic Heterogeneity. In *Dynamical Heterogeneities in Glasses, Colloids, and Granular Media*, Berthier, L.; Biroli, G.; Bouchaud, J. P.; Cipelletti, L.; Van Saarloos, W., Eds. OUP Oxford: 2011; pp 68-109.

37. May, R. A.; Smith, R. S.; Kay, B. D., Mobility of supercooled liquid toluene, ethylbenzene, and benzene near their glass transition temperatures investigated using inert gas permeation. *J Phys Chem A* **2013,** *117* (46), 11881-9.

38. Berthier, L., Dynamic Heterogeneity in Amorphous Materials. *Physics* **2011,** *4*.

39. Donth, E., *The Glass Transition Relaxation Dynamics in Liquids and Disordered Materials* Springer-Verlag: New-York, 2001; Vol. 48.

40. Berthier, L.; Biroli, G., Theoretical perspective on the glass transition and amorphous materials. *Rev. Mod. Phys.* **2011,** *83* (2), 587-645.

41. Ritort, F.; Sollich, P., Glassy dynamics of kinetically constrained models. *Advances in Physics* **2003,** *52* (4), 219-342.

42. Kivelson, S. A.; Tarjus, G., In search of a theory of supercooled liquids. *Nat Mater* **2008,** *7* (11), 831-833.

43. Charbonneau, P.; Kurchan, J.; Parisi, G.; Urbani, P.; Zamponi, F., Glass and Jamming Transitions: From Exact Results to Finite-Dimensional Descriptions. In *Annual Review of Condensed Matter Physics, Vol 8*, Marchetti, M. C.; Sachdev, S., Eds. Annual Reviews: Palo Alto, 2017; Vol. 8, pp 265-288.

44. Suarez-Iglesias, O.; Medina, I.; Sanz, M. D.; Pizarro, C.; Bueno, J. L., Self-Diffusion in Molecular Fluids and Noble Gases: Available Data. *J. Chem. Eng. Data* **2015,** *60* (10), 2757-2817.

45. Hodge, I. M., Adam-Gibbs formulation of enthalpy relaxation near the glass transition. *J. Res. Natl. Inst. Stand. Technol.* **1997,** *102* (2), 195-205.

46. Kapko, V.; Zhao, Z. F.; Matyushov, D. V.; Angell, C. A., "Ideal glassformers" vs "ideal glasses": Studies of crystal-free routes to the glassy state by "potential tuning" molecular dynamics, and laboratory calorimetry. *Journal of Chemical Physics* **2013,** *138* (12).

47. Daley, C. R.; Fakhraai, Z.; Ediger, M. D.; Forrest, J. A., Comparing surface and bulk flow of a molecular glass former. *Soft Matter* **2012,** *8* (7), 2206-2212.

48. Zhu, L.; Brian, C. W.; Swallen, S. F.; Straus, P. T.; Ediger, M. D.; Yu, L., Surface Self-Diffusion of an Organic Glass. *Phys. Rev. Lett.* **2011,** *106* (25).

49. Swallen, S. F.; Kearns, K. L.; Mapes, M. K.; Kim, Y. S.; McMahon, R. J.; Ediger, M. D.; Wu, T.; Yu, L.; Satija, S., Organic Glasses with Exceptional Thermodynamic and Kinetic Stability. *Science* **2007,** *315* (5810), 353-356.

50. Chen, Z.; Sepulveda, A.; Ediger, M. D.; Richert, R., Dynamics of glass-forming liquids. XVI. Observation of ultrastable glass transformation via dielectric spectroscopy. *Journal of Chemical Physics* **2013,** *138* (12), 12A519.

51. Chua, Y. Z.; Ahrenberg, M.; Tylinski, M.; Ediger, M. D.; Schick, C., How much time is needed to form a kinetically stable glass? AC calorimetric study of vapor-deposited glasses of ethylcyclohexane. *Journal of Chemical Physics* **2015,** *142* (5), 11.

52. Dalal, S. S.; Ediger, M. D., Influence of Substrate Temperature on the Transformation Front Velocities That Determine Thermal Stability of Vapor-Deposited Glasses. *Journal of Physical Chemistry B* **2015,** *119* (9), 3875-3882.

53. Fakhraai, Z.; Still, T.; Fytas, G.; Ediger, M. D., Structural Variations of an Organic Glassformer Vapor-Deposited onto a Temperature Gradient Stage. *Journal of Physical Chemistry Letters* **2011,** *2* (5), 423-427.

54. Dalal, S. S.; Sepulveda, A.; Pribil, G. K.; Fakhraai, Z.; Ediger, M. D., Density and birefringence of a highly stable alpha,alpha,beta-trisnaphthylbenzene glass. *Journal of Chemical Physics* **2012,** *136* (20), 10.

55. Dawson, K.; Kopff, L. A.; Zhu, L.; McMahon, R. J.; Yu, L.; Richert, R.; Ediger, M. D., Molecular packing in highly stable glasses of vapor-deposited tris-naphthylbenzene isomers. *Journal of Chemical Physics* **2012,** *136* (9), 094505.

56. Ishii, K.; Nakayama, H., Structural relaxation of vapor-deposited molecular glasses and supercooled liquids. *Physical Chemistry Chemical Physics* **2014,** *16* (24), 12073-12092.

57. Kearns, K. L.; Swallen, S. F.; Ediger, M. D.; Wu, T.; Sun, Y.; Yu, L., Hiking down the energy landscape: Progress toward the Kauzmann temperature via vapor deposition. *J. Phys. Chem. B* **2008,** *112* (16), 4934-4942.

58. Lyubimov, I.; Ediger, M. D.; de Pablo, J. J., Model vapor-deposited glasses: Growth front and composition effects. *Journal of Chemical Physics* **2013,** *139* (14), 144505.

59. Lin, P. H.; Lyubimov, I.; Yu, L.; Ediger, M. D.; de Pablo, J. J., Molecular modeling of vapor-deposited polymer glasses. *Journal of Chemical Physics* **2014,** *140* (20), 9.

60. Liu, T. Y.; Exarhos, A. L.; Alguire, E. C.; Gao, F.; Salami-Ranjbaran, E.; Cheng, K.; Jia, T. Z.; Subotnik, J. E.; Walsh, P. J.; Kikkawa, J. M.; Fakhraai, Z., Birefringent Stable Glass with Predominantly Isotropic Molecular Orientation. *Phys. Rev. Lett.* **2017,** *119* (9), 6.

61. Sepulveda, A.; Leon-Gutierrez, E.; Gonzalez-Silveira, M.; Clavaguera-Mora, M. T.; Rodriguez-Viejo, J., Anomalous Transformation of Vapor-Deposited Highly Stable Glasses of Toluene into Mixed Glassy States by Annealing Above T-g. *Journal of Physical Chemistry Letters* **2012,** *3* (7), 919-923.

62. Sepulveda, A.; Tylinski, M.; Guiseppi-Elie, A.; Richert, R.; Ediger, M. D., Role of Fragility in the Formation of Highly Stable Organic Glasses. *Physical Review Letters* **2014,** *113* (4), 5.

63. Bhattacharya, D.; Sadtchenko, V., Vapor-deposited non-crystalline phase vs ordinary glasses and supercooled liquids: Subtle thermodynamic and kinetic differences. *Journal of Chemical Physics* **2015,** *142* (16), 9.

64. Tylinski, M.; Chua, Y. Z.; Beasley, M. S.; Schick, C.; Ediger, M. D., Vapor-deposited alcohol glasses reveal a wide range of kinetic stability. *Journal of Chemical Physics* **2016,** *145* (17), 12.

65. Walters, D. M.; Antony, L.; de Pablo, J. J.; Ediger, M. D., Influence of Molecular Shape on the Thermal Stability and Molecular Orientation of Vapor-Deposited Organic Semiconductors. *Journal of Physical Chemistry Letters* **2017,** *8* (14), 3380-3386.

66. Ahrenberg, M.; Chua, Y. Z.; Whitaker, K. R.; Huth, H.; Ediger, M. D.; Schick, C., In situ investigation of vapor-deposited glasses of toluene and ethylbenzene via alternating current chip-nanocalorimetry. *Journal of Chemical Physics* **2013,** *138* (2), 11.

67. Antony, L. W.; Jackson, N. E.; Lyubimov, I.; Vishwanath, V.; Ediger, M. D.; de Pablo, J. J., Influence of Vapor Deposition on Structural and Charge Transport Properties of Ethylbenzene Films. *ACS Central Sci.* **2017,** *3* (5), 415-424.

68. Venables, J. A.; Spiller, G. D. T.; Hanbucken, M., Nucleation and growth of thin films. *Reports on Progress in Physics* **1984,** *47* (4), 399.

69. Ruiz, R.; Nickel, B.; Koch, N.; Feldman, L. C.; Haglund, R. F.; Kahn, A.; Family, F.; Scoles, G., Dynamic scaling, island size distribution, and morphology in the aggregation regime of submonolayer pentacene films. *Phys. Rev. Lett.* **2003,** *91* (13), 136102.

70. Amar, J. G.; Family, F.; Lam, P.-M., Dynamic scaling of the island-size distribution and percolation in a model of submonolayer molecular-beam epitaxy. *Phys. Rev. B* **1994,** *50* (12), 8781-8797.

71. Plass, K. E.; Grzesiak, A. L.; Matzger, A. J., Molecular Packing and Symmetry of Two-Dimensional Crystals. *Accounts of Chemical Research* **2007,** *40* (4), 287-293.

72. Plass, K. E.; Kim, K.; Matzger, A. J., Two-Dimensional Crystallization: Self-Assembly, Pseudopolymorphism, and Symmetry-Independent Molecules. *Journal of the American Chemical Society* **2004,** *126* (29), 9042-9053.

73. Smith, R. S.; May, R. A.; Kay, B. D., Probing Toluene and Ethylbenzene Stable Glass Formation Using Inert Gas Permeation. *Journal of Physical Chemistry Letters* **2015,** *6* (18), 3639-3644.

74. Chua, Y. Z.; Tylinski, M.; Tatsumi, S.; Ediger, M. D.; Schick, C., Glass transition and stable glass formation of tetrachloromethane. *Journal of Chemical Physics* **2016,** *144* (24), 9.

75. Dawson, K. J.; Kearns, K. L.; Yu, L.; Steffen, W.; Ediger, M. D., Physical vapor deposition as a route to hidden amorphous states. *Proceedings of the National Academy of Sciences* **2009,** *106* (36), 15165-15170.

76. Kearns, K. L.; Ediger, M. D.; Huth, H.; Schick, C., One Micrometer Length Scale Controls Kinetic Stability of Low-Energy Glasses. *Journal of Physical Chemistry Letters* **2010,** *1* (1), 388-392.

77. Leon-Gutierrez, E.; Sepulveda, A.; Garcia, G.; Clavaguera-Mora, M. T.; Rodriguez-Viejo, J., Stability of thin film glasses of toluene and ethylbenzene formed by vapor deposition: an in situ nanocalorimetric study. *Physical Chemistry Chemical Physics* **2010,** *12* (44), 14693-14698.

78. Chen, Z.; Richert, R., Dynamics of glass-forming liquids. XV. Dynamical features of molecular liquids that form ultra-stable glasses by vapor deposition. *Journal of Chemical Physics* **2011,** *135* (12).

79. Singh, S.; de Pablo, J. J., A molecular view of vapor deposited glasses. *The Journal of Chemical Physics* **2011,** *134* (19), 194903.

80. Sun, Y.; Zhu, L.; Kearns, K. L.; Ediger, M. D.; Yu, L. A., Glasses crystallize rapidly at free surfaces by growing crystals upward. *Proc. Natl. Acad. Sci. U. S. A.* **2011,** *108* (15), 5990-5995.

81. Ediger, M. D.; Harrowell, P., Perspective: Supercooled liquids and glasses. *Journal of Chemical Physics* **2012,** *137* (8), 080901-1-14.

82. Guo, Y.; Morozov, A.; Schneider, D.; Chung, J. W.; Zhang, C.; Waldmann, M.; Yao, N.; Fytas, G.; Arnold, C. B.; Priestley, R. D., Ultrastable nanostructured polymer glasses. *Nat Mater* **2012,** *11* (4), 337-343.

83. Ahrenberg, M.; Chua, Y. Z.; Whitaker, K. R.; Huth, H.; Ediger, M. D.; Schick, C., In situ investigation of vapor-deposited glasses of toluene and ethylbenzene via alternating current chip-nanocalorimetry. *Journal of Chemical Physics* **2013,** *138* (2).

84. Chen, Z.; Sepulveda, A.; Ediger, M. D.; Richert, R., Dynamics of glass-forming liquids. XVI. Observation of ultrastable glass transformation via dielectric spectroscopy. *Journal of Chemical Physics* **2013,** *138* (12).

85. Douglass, I.; Harrowell, P., Can a stable glass be superheated? Modelling the kinetic stability of coated glassy films. *Journal of Chemical Physics* **2013,** *138* (12).

86. Sepulveda, A.; Swallen, S. F.; Ediger, M. D., Manipulating the properties of stable organic glasses using kinetic facilitation. *Journal of Chemical Physics* **2013,** *138* (12), 12A517.

87. Singh, S.; Ediger, M. D.; de Pablo, J. J., Ultrastable glasses from in silico vapour deposition. *Nature Materials* **2013,** *12* (2), 139-144.

88. May, R. A.; Smith, R. S.; Kay, B. D., Mobility of Supercooled Liquid Toluene, Ethylbenzene, and Benzene near Their Glass Transition Temperatures Investigated Using Inert Gas Permeation. *J. Phys. Chem. A* **2013,** *117* (46), 11881-11889.

89. Renuka, C.; Shinde, A. B.; Krishna, P. S. R.; Reddy, C. N., Structural analysis of molybdo-zinc-phosphate glasses: Neutron scattering, FTIR, Raman scattering, MAS NMR studies. *Journal of Molecular Structure* **2016,** *1118*, 83-90.

90. Wang, W.; Barber, A. H., Measurement of size-dependent glass transition temperature in electrospun polymer fibers using AFM nanomechanical testing. *Journal of Polymer Science Part B: Polymer Physics* **2012,** *50* (8), 546-551.

91. Duval, E.; Boukenter, A.; Achibat, T., Vibrational dynamics and the structure of glasses. *Journal of Physics: Condensed Matter* **1990,** *2* (51), 10227.

92. Dalba, G.; Afify, N. D.; Rocca, F., X-ray absorption spectroscopy studies of glass structure. *Physics and Chemistry of Glasses - European Journal of Glass Science andTechnology Part B* **2008,** *49* (3), 149-159.

93. Bhattacharya, D.; Sadtchenko, V., Enthalpy and high temperature relaxation kinetics of stable vapor-deposited glasses of toluene. *The Journal of Chemical Physics* **2014,** *141* (9), 094502.

94. Kearns, K. L.; Whitaker, K. R.; Ediger, M. D.; Huth, H.; Schick, C., Observation of low heat capacities for vapor-deposited glasses of indomethacin as determined by AC nanocalorimetry. *The Journal of Chemical Physics* **2010,** *133* (1), -.

95. Ahrenberg, M.; Shoifet, E.; Whitaker, K. R.; Huth, H.; Ediger, M. D.; Schick, C., Differential alternating current chip calorimeter for in situ investigation of vapor-deposited thin films. *Review of Scientific Instruments* **2012,** *83* (3), 033902.

96. Chua, Y. Z.; Ahrenberg, M.; Tylinski, M.; Ediger, M. D.; Schick, C., How much time is needed to form a kinetically stable glass? AC calorimetric study of vapor-deposited glasses of ethylcyclohexane. *The Journal of Chemical Physics* **2015,** *142* (5), 054506.

97. Leon-Gutierrez, E.; Garcia, G.; Lopeandia, A. F.; Fraxedas, J.; Clavaguera-Mora, M. T.; Rodriguez-Viejo, J., In situ nanocalorimetry of thin glassy organic films. *Journal of Chemical Physics* **2008,** *129* (18), 181101.

98. Schick, C.; Mathot, V., *Fast Scanning Calorimetry*. Springer International Publishing: 2016.

Chapter Two: Experimental apparatus and procedures

Preface: This Chapter is a modified manuscript of the chapter[1] published in Springer's book: Fast Scanning Calorimetry[3] with co-authors Deepanjan Bhattacharya and Vladislav Sadtchenko.

2.1. Brief overview of Fast Scanning Calorimetry (FSC)

In its essence, the FSC technique is consists of heating glassy, liquid, or crystalline materials from an initial temperature, T_i, with rates many times faster (accessible rates are from 10^3 to 10^7 $K \cdot s^{-1}$) than those employed in classical Differential Scanning Calorimetry[3] (DSC) experiments (1 $K \cdot min^{-1}$). As shown in the top panel of Fig. 2.1, the rapid heating of a non-crystalline material (e.g. a vapor deposited film on a thin filament) results in fast relaxation endotherms (FREs) whose magnitudes and positions are *extremely* sensitive to the initial structural and thermodynamic state of the sample. As I will discuss in Chapter 3-6 of this Dissertation, the shape of the endotherm in an FSC thermogram carries a wealth of information about the structure and dynamics of the system, its initial conditions and temperature[4-5], the dynamics far from equilibrium, and even the general equilibrium properties of the system[6].

2.2. Essential hardware

The wire-based FSC apparatus is conceptually simple and scalable. As shown in the center of Fig. 2.2, the calorimeter is essentially a *thin metal filament* surrounded by high vacuum and cryogenic shielding. These conditions allow the calorimeter to function *adiabatically* during fast temperature scanning. For all experiments in this Dissertation, we

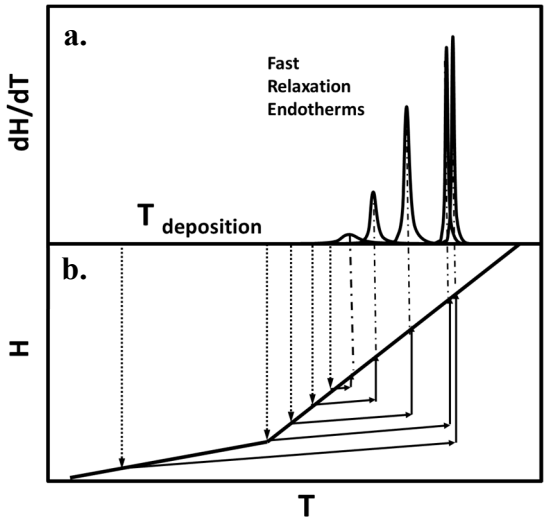

Fig. 2.1. Fundamentals of Fast Scanning Calorimetry. **(a)** FSC thermograms: apparent heat capacity. **(b)** The enthalpy changes in the sample films during rapid heating. Vapor deposition of constituents on a cold substrate at temperatures, $\mathbf{T_d}$, may result in formation of non-crystalline samples characterized by distinct enthalpies. Rapid heating of such samples results in **fast relaxation endotherms (FREs)** at temperatures, T_{FRE}, that are tens of degrees above the initial temperature, T_d. The position and shape of FREs are sensitive to the initial state of the sample.

utilized a tungsten wire that is 10 μm in diameter and 1.6 cm in length, as a thin wire's high thermal resistance facilitates rapid heat loading[7]. Tungsten was selected because of its high mechanical strength, ease of handling, low thermal expansion coefficient and very low cost[8-9]. Companies such as Goodfellow Corp. stock a wide variety of specialty wires, including bare and gold-coated W filament as thin as 5 μm. Note that after initial conditioning, the surface of the metal filament is oxidized such that the substrate surface for our experiments is likely a thin coat of tungsten oxide.

As illustrated in Fig 2.2, the filament is attached to copper support struts, which are in direct thermal contact with a liquid nitrogen (LN) heat sink. However, the supports are electrically isolated from the rest of the apparatus with two sapphire spacers (1 mm thick and 1 cm wide) placed between the supports and the heat sink bar. Spring loaded stainless steel screws and an arrangement of ceramic washers were used to mechanically fasten the support to the heat sink without breaking the electrical insolation.

In all experiments, the tungsten filament is attached to its support struts with a vacuum safe, lead free solder (Kester #83-7068-1402) that did not deteriorate under high heat and high vacuum conditions[10]. Though the wire can also be attached by spot-welding, soldering was useful because it reduced damage to the copper supports when the wire is replaced. Note that the mismatch in the thermal expansion coefficient of the solder alloy, W filament, and copper supports can lead mechanical decoupling and increased contact resistance (by 1-2 Ω) after cryogenic cooling. However, rapid cooling never results in a complete loss of electrical connectivity between the filament and the supports. Furthermore, the proper connection can always be restored by rapidly heating the bare filament using a few FSC scans or by passing 24 mA of currents through the filament from

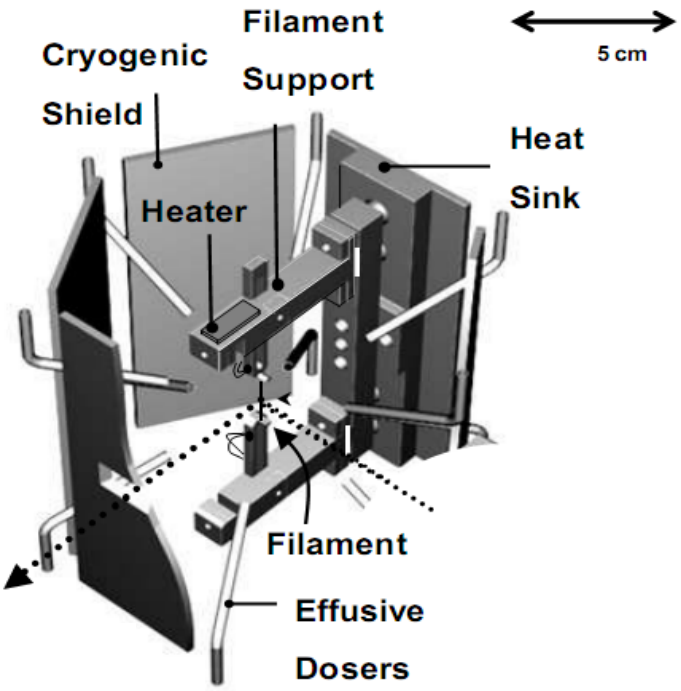

Fig. 2.2. Schematic diagram of the FSC device that occupies the apparatus's high vacuum chamber. The calorimeter (**filament**) is attached to filament **supports** that are in thermal equilibrium with a LN-cooled **heat sink**. The temperature of these supports is regulated with resistive **heaters**. Precisely aligned **effusive dosers** connect to a vapor deposition system for sample preparation. See text for details.

a hand-held current source (e.g. Fluke 750 Loop Calibrator).

The filament holder in Fig. 2.2 is surrounded by six cryogenic shields, which are cooled by the LN heat sink. The shields serve two purposes. First, they increased the pumping speed of the vacuum system of the FSC apparatus for condensable compounds such as water. They lower the partial pressure of condensable gasses in the chamber to approximately 10^{-9} Torr. Second, the shields reduce the radiative heating of the filament and supports by the walls and other parts of the vacuum chamber, which are maintained at ambient temperature[11]. The shields and all other essential parts of the calorimeter assembly utilized in the FSC experiments I describe in this Dissertation were custom-fabricated from high purity cooper at the GWU machine shop.

The calorimeter assembly illustrated in Fig 2.2. occupies an oil-free, high vacuum chamber built from a stainless-steel, 6-way cross (Kurt J. Lesker) and flanges (ISO-250K). The chamber has an inner diameter of approximately 24 cm and a volume of 75 Liters. The chamber's internal pressure of $5 \cdot 10^{-7}$ Torr is maintained by a 1500 $L \cdot s^{-1}$ turbo molecular pump (Leybold TMP 1000 C) and a back-up mechanical pump. This pressure is monitored by an ion gauge (Bayard Alpert type gauge tube)[11]. Additionally, although not utilized for the experiments described in this Dissertation, the apparatus is also equipped with a quadrupole mass spectrometer (RGA 300 from Stanford Research Instruments) positioned within a differentially pumped chamber[11].

The FSC instrument was specifically designed with a robust control of substrate temperature to facilitate sample preparation with a range of thermal histories. The filament support temperature, and thus the initial temperature (T_i) of the filament substrate (i.e. prior to an FSC scan), is highly adjustable from below cryogenic (90 K) to above room

temperature. The T_d or T_i can be modified by balancing the heat flow from resistive heaters to the supports against heat loss from the supports to the LN-cooled heat sink. The temperature of each support is monitored and can be adjusted independently via the temperature controller (Lakeshore Cryotronics Model 355). The temperature controller is auto-tuned to the desired temperature range and control parameters are kept constant throughout each experiment. As shown in Fig. 2.2, each support is equipped with a resistive heater cartridge capable of generating up to 25 W of power (Lakeshore HTR-25). Platinum resistance temperature detectors (Lakeshore PT-111 RTD) are mounted within 1mm of the filament to measure T_d or T_i with an accuracy of ±10 mK. The temperature controller can also be programmed with a wide range of heating and cooling ramps that can modify the sample's thermal history.

2.3. Physical vapor deposition system

The vapor deposition system utilized by our laboratory's FSC apparatus facilitates the preparation of condensed phase films that can be crystalline, liquid, melt-cooled glass, and kinetically stable VD glass. As illustrated in Fig. 2.2 and Fig. 2.3.b, the tungsten filament that serves as the deposition substrate is surrounded by 12 effusive dosers. The dosers are 1/8-inch diameter stainless steel tubes which are equally spaced about 2 cm from the filament. Each tube is positioned at an angle of about 60° with respect to the filament axis. In fact, the key to the deposition of neat films on a cylindrical filament is not the large number of dosers surrounding the filament but the proper alignment of these. The goal of the alignment should be to ensure head-on collision of the effusive beams, so that a localized vapor cloud could form around the filament during deposition.

The effusive dosers surrounding the substrate filament are connected to a custom-

designed vapor source that includes an axillary vacuum system. An outline of the vapor/gas source is shown in Fig. 2.3.a. The source was designed to facilitate deposition of vapors or condensable gases on the surface of the filament with rates ranging from 0.5 to 50 $nm \cdot s^{-1}$. In the case of samples which are liquid at ambient temperatures, a glass flask half-filled with the compound of interest is typically used. The flask is immersed in a cooling bath, and its temperature is lowered to a value between 10 and 20 ^{o}C. Maintaining the liquid at temperatures below ambient ensured that no condensation of the vapor is possible inside the source's vacuum lines and valves. In the case of samples which are in gaseous form at ambient temperature, a compressed tank or a lecture bottle is connected to the source either directly or through a pressure regulator.

The flow of vapor or gas from the cylinder or flask, i.e. vapor pressure of the source, is controlled with a precision variable leak valve (Granville-Phillips Co. Series 203). After the leak valve, the gas or vapor enters the main vacuum line of the source, which is connected to both the axillary stand-along mechanical pump and the lines leading to effusive dosers inside the main vacuum chamber. To avoid contamination of the vacuum lines and valves, the mechanical pump is equipped with an in-line LN vapor trap. Additionally, a series of manual throttle valves, shown in Fig. 2.3.a, are also used to regulate the flow of vapor into the mechanical pump, thereby controlling the vapor pressure of the deposition source. The fairly complex arrangement illustrated in Fig. 2.3 allows very precise control and an improved stability of vapor flux rate during sample preparation. For example, the continuous pumping of the source makes it possible to avoid a spike in vapor flux at the start of deposition, ensuring a near-constant flux from the beginning to the end of sample preparation.

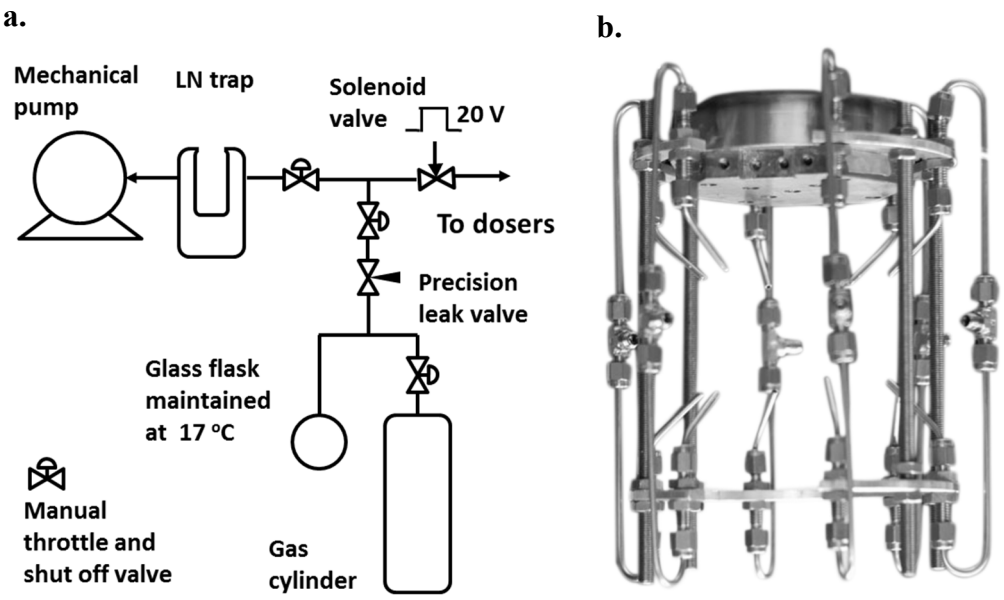

Fig. 2.3. (a) Diagram of the FSC apparatus's vapor source for deposition of micrometer-thick films of condensed phases (liquid, crystalline, melt-cooled glass, and stable VD glass). **(b)** View of the effusive dosers that surround the filament and its supports in the custom-built FSC apparatus.

The main line of the vapor source connects to the effusive dosers that surround the filament substrate within the FSC chamber via two solenoid valves (Parker Hannifin's series 9 miniature gas valve). These valves are normally closed and can be actuated manually or by the automated data acquisition and process control system (DAQPC), which is detailed in the next Section (2.4). The solenoid valves can be opened to allow the flow of vapor or gas into the effusive dosers for a time period ranging from 50 milliseconds to several hours. Thus, the deposition time can be varied to control sample film thickness.

2.4. Data acquisition and process control system (DAQPCs)

The data acquisition and process control system of the FSC apparatus is based on a single multifunctional electronic board for PC computers from National Instruments (NI) Corp. The board (model PCI 6620) includes four analog-to-digital converters (ADCs) capable of operating in double-ended configuration with a number of digital inputs and outputs (DI and DO). The resolution of each ADC is 16-bit and the sampling rate per channel can be as high as 10^6 measurements per second. A custom DAQPC software program was developed to operate the FSC apparatus using NI's LabVIEW software.

In addition to its function of initiating FSC scans and collecting FSC data, the PCI 6250 board is also used to control the vapor-deposition source of the FSC apparatus. As illustrated in Fig. 2.4, prior to scanning, one of the board's digital outputs (DO2) is used to send a +5 V latching pulse to the solenoid valve driver (Parker Hannifin's General Valve Driver II). The latching pulse activates the driver that opens the solenoid valve to the vapor dosers (Fig. 2.3). The generation of this first pulse also starts the clock on the PCI board. After a pre-programed time interval, the board generates a second latching pulse which returns the driver to its inactive state, closing the valve to the dosers. As we already

mentioned, the solenoid valve connecting the vapor system to the chamber dosers can be held open from 50 ms to several hours by changing the time interval between the latching pulses.

As illustrated in Fig. 2.4, a typical fast temperature scanning experiment begins after film deposition is complete with the software generating a 5 V trigger pulse from one of the digital outputs (DO1). The trigger pulse from the DAQPC board is routed to an external trigger input of a pulse generator (Wavetek Model 801). The pulse generator is manually configured to produce a single 5 V switch driver pulse of desirable time duration, typically from 100 μs to 10 ms. The generator's output is connected to a transistor switch, essentially a NPN Darlington pair (TIP 120 produced by O.N. Semiconductor), with a maximum collector current of 5 A and a collector-emitter voltage as high as 60 V. The switching time of the TIP 120 pair is a less than one microsecond. Activation of the transistor switch results in a time varying electrical current flow through the filament, which is continually biased with a voltage of +1 V to +5 V. The bias voltage is generated by an inexpensive direct current (DC) power supply (Mastech Model HY 5003), operating in a voltage limited mode.

Concurrently with the activation of the transistor switch, the DAQPS board triggers the timed data collection sequence. Two pairs of analog inputs (AIs) on the PCI 6250 board record the voltage drops in the system every microsecond. As illustrated in Fig. 2.4, the first pair (AI1) records the voltage drop across the rapidly heating filament (V_f). The other pair (AI2) measures the voltage drop (V_s) across a "sensing resister" (R_s). The sensing resistor (approximately 1.5 Ω) is connected in series to the filament and resides inside a shielded electrical box outside the main vacuum chamber of the FSC apparatus.

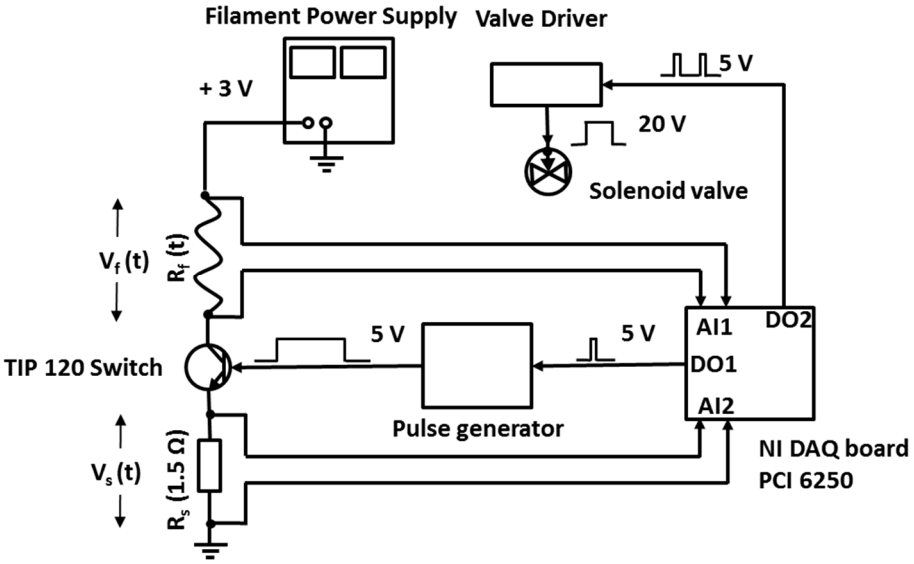

Fig. 2.4. Outline of the data acquisition and process control system (DAQPC) of the FSC apparatus. The DAQPC is based on a multifunctional electronic data acquisition board from National Instruments (**PCI 6250**). The board's **digital outputs** are used to operate the **valve driver** (DO2) for the apparatus's vapor deposition system and initiate FSC scans (DO1). The duration of the FSC scan is set by the **pulse generator** and the power used to heat the calorimeter ($\mathbf{R_f}$) is provided by the external **power supply**. The PCI board's two **analog inputs** (AI), which are capable of sampling rates on the order of 1MHz during FSC scans, measure the current and voltage drop across the filament and sensing resistor ($\mathbf{R_s}$), connected in series to the filament. See text for details.

The V_s values value are used to determine the current through the filament during heating. They are calculated from a priori calibrations of the apparatus that are performed whenever the electronics or connector wires of the DAQPC are modified. This calibration consists of disconnecting the filament, which has a changing resistance as temperatures change during a scan, and replacing it with a standard test resistor, R_t (e.g. 10.035 Ω). Data is collected while modifying the bias voltage of the power supply. From the voltage drop measured at the test resistor, V_t, the current is calculated ($I_t = V_t/R_t$) and can be plotted as a function of the voltage drop across the sensing resistor, as shown in Fig. 2.5. The slope (m_i) and near-zero intercept (b_i) of the data's linear fit are used as current calibration parameters during FSC experiments. Thus, the current passing through the filament is derived from V_s values as $I_f = m_i \cdot V_s + b_i$.

Fig. 2.6 shows variations in the voltage drop (V_f) and the calculated current (I_f) through the bare filament during rapid heating, as recorded by the DAQPC system of the FSC apparatus. The voltage and current values shown in Fig. 2.6 typically translate into heating rates on the order of 10^5 K/s in a temperature range from 100 to 180 K. The insets show the typical random noise levels during the voltage and current measurements, which were obtained by subtracting polynomial fits from the $I_f(t)$ and $V_f(t)$ curves shown in the main plots of Fig. 2.6. The signal to noise (SN) ratio in current and voltage measurements is approximately 10^4. This high SN ratio is achieved primarily by carefully rearranging the power and signal lines for the DAQPC to eliminate the ground loops. Note that the data shown in Fig. 2.6 do not represent the best possible result of noise elimination. In fact, in some of the experiments I describe in this Dissertation, we were able to reduce the noise level even further, i.e. to the levels approaching the resolution of the ADCs of the PCI 6250

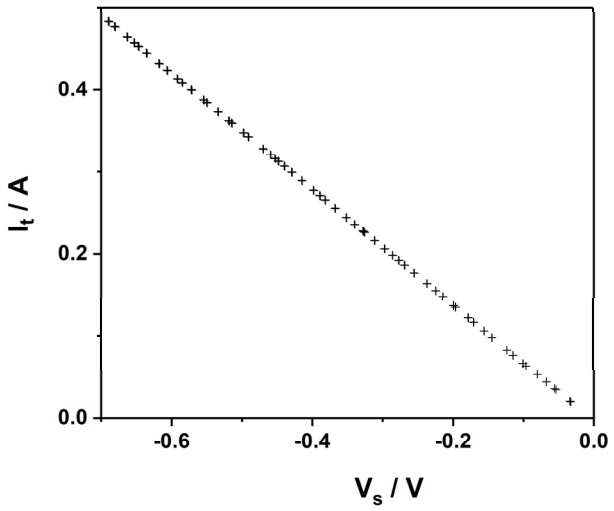

Fig. 2.5. Filament current calibration procedure. Example data for the a priori current calibration procedure used to derive the current values, $I_f(t)$, from the voltage drop across the sensing resistor, $V_s(t)$, measured by PCI's board (AI2) during FSC scans. During calibration, the filament is replaced by a **test** resistor, $\mathbf{R_t}$, and the bias provided by the power supply is modulated to derive the relationship between $\mathbf{V_s}$ values and current, $\mathbf{I_t}$, through the **test** circuit (see Fig. 2.4). The details of the calibration are described in the text.

board (0.06 mV for the dynamic range of ± 2 V). Further improvement in the SN ration of the voltage and current measurements can be achieved by using DAQ boards with greater number of analog inputs (i.e. four AIs for each voltage measurement instead of two) and higher resolution (e.g. 18 bit). Nevertheless, the noise values shown in the Fig. 2.6 insets are sufficiently low to allow measurements of good quality FSC thermograms of micrometer-thick condensed phase films. Note that inferring the FSC thermograms of acceptable quality from the data shown in Fig. 2.6 does not require any digital filtering or smoothing of data.

2.5. Temperature and heat capacity calculations

The primary temperature sensor of the FSC calorimeter is the filament itself. In all experiments, the resistance of the filament is used to determine its temperature *during and immediately prior to* rapid FSC scans. The filament's resistance, ($R_f = V_f / I_f$), is derived from the primary data collected by the PCI board. In the temperature range of FSC experiments, the time-dependent temperature of the tungsten filament is a linear function of the filament's resistance:

$$T(t) = m_T \cdot R_f(t) + b_T. \quad (2.1)$$

The parameters of this relation can be derived from a routine, a priori temperature calibration procedure, which is described in the next Section (2.6) of this Chapter.

The FSC thermograms for sample films are calculated by the following method. First, the voltage and current values measured by the DAQs during FSC scans can be used to calculate the heat, i.e. power, generated by the quasi-adiabatic filament:

$$\frac{d}{dt} Q(t) = V_f(t) \cdot I_f(t). \quad (2.2)$$

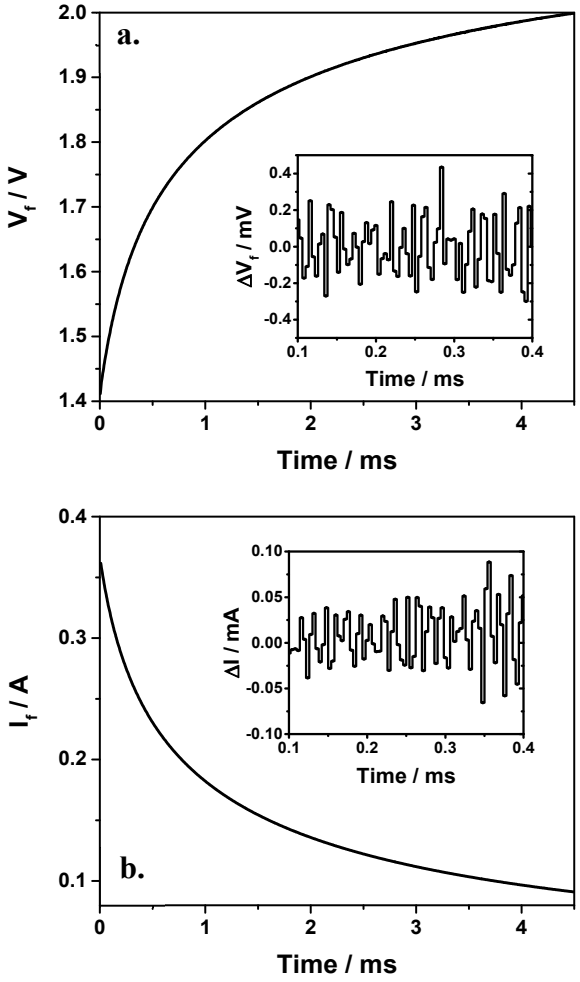

Fig. 2.6. Typical primary data collected during an FSC experiment. Every 4 μs, the DAQPC system takes two measurements for the voltage drop across the filament, $\mathbf{V_f}$, and the for current through the filament, $\mathbf{I_f}$. An average for each pair provides the time-dependent $V_f(t)$ and $I_f(t)$ data used to derive temperature, heating rate, heat flow rate, and finally apparent heat capacity. Example data for the voltage drop (**a.**) and current (**b.**) show the typical changes in the values and the **insets** show the random fluctuation in these values during a typical FSC scan.

Second, the heating rate of the filament,

$$HR = \frac{d}{dt}T(t), \quad (2.3)$$

is derived by taking the time derivative of the temperature calculated by Eq. 2.1. These values are used to calculate the apparent heat capacity of the entire sample-filament system:

$$C_{p,system}(t) = \frac{dQ}{dt} \cdot \frac{dt}{dT}. \quad (2.4)$$

The apparent heat capacity of only the film is inferred from the overall heat capacity of the sample-filament system, by subtracting the heat capacity of the bare filament, which is measured during an auxiliary FSC scan that immediately follows each experimental scan:

$$C_{p,a}(t) = C_{p,system}(t) - C_{p,filament}(t). \quad (2.5)$$

2.6. Routine temperature calibrations

A routine, a priori temperature calibration procedure utilized the robust temperature control (TC) system of the filament supports (Lakeshore Cryotronics Model 355), which is described in the last paragraph of Section 2.2. At the beginning of each day, the resistance of the filament was related to its temperature using the following experimental protocol (Eq. 2.1). First, the calorimeter is cooled to its lowest possible temperature (approximately 95 K) by switching the support heaters off. In this state, the upper support (see Fig. 2.2), which is in contact with the LN heat sink, is typically at a temperature a few K below that of the lower support. Then, the TC system is switched on, with equivalent temperatures set for both supports. Note that, in the temperature range of typical FSC experiments, the TC maintains the set filament support temperatures within ±0.03 K.

After equalizing the temperatures of the supports to a temperature near 100 K, the filament is heated with the rate of approximately 10^5 K/s and its resistance is calculated

and plotted as the function of time. As shown in Fig. 2.7.a, the resistances measured during the first 100 μs were extrapolated to zero time. The extrapolated resistance, R_0, of the filament is assumed to be nearly equal to the resistance of the filament prior to the rapid scan (the validity of this assumption was verified by measuring the resistance values with an ohmmeter). The temperature of the supports is then adjusted to a higher value and the experiment is repeated. In short, resistances of the filament can be measured for distinct support temperatures in the range of 100 to 170 K. As shown in Fig. 2.7.b, the resistance of the filament can be plotted against the support temperature and fit with a linear function (see Eq. 2.1). The parameters of that linear fit, m_T and b_T, are later used to infer the filament's temperature from its resistance, as described in Section 2.5.

An alternative to the procedure described in the preceding paragraph is to use an accurate ohmmeter to measure the filament resistance for distinct support temperatures. However, we chose not to follow this alternative protocol due to the following reasons. First, the high SN ration of voltage and current measurements facilitated by the DAQPC system made it possible to determine the resistance of the filament with a *precision* of better than 0.001 Ω. Such precise resistance measurements translate into a precision of the filament's temperature determination on the order of 0.05 K, which is more than sufficient for all FSC experiments. Second, as described in Section 2.2, drastic changes in the temperature of the supports sometimes results in a rather significant random increase of the filament's apparent resistance, due to its partial electrical decoupling from the attachment points at the supports. The increase in the apparent resistance is easily eliminated by "re-soldering" the filament during a rapid temperature scan. In other words, using an ohmmeter still required rapid scans and, therefore, its use would be redundant.

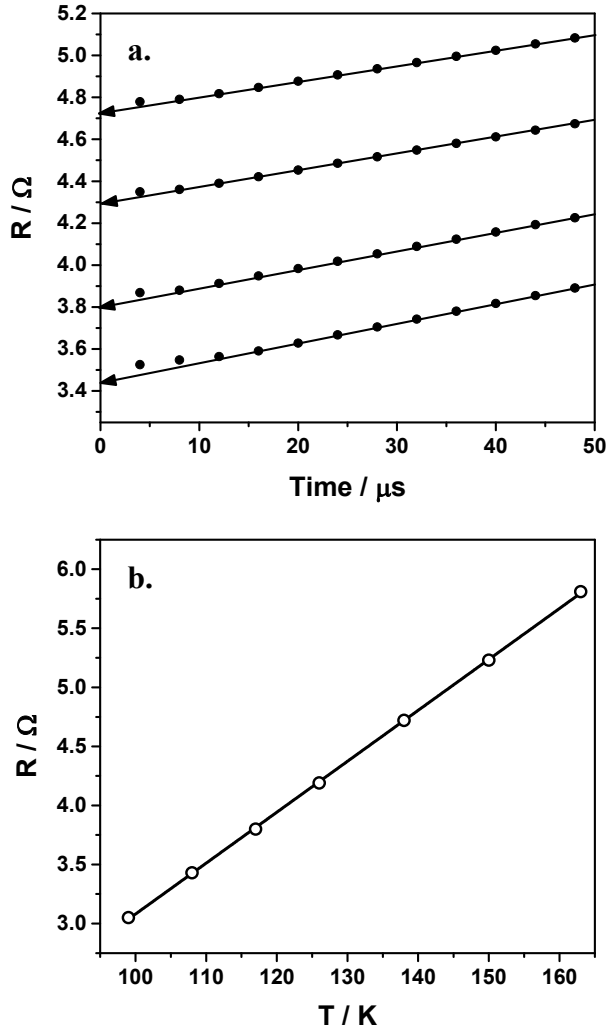

Fig. 2.7. Temperature calibration procedure**. (a)** The resistance of the filament system, **R(t),** during the early stages of a rapid scan calculated from the current and voltage data. An extrapolation of **R(t)** toward zero time are used to determine the filament resistance prior to the scan, $\mathbf{R_0}$**.** The lines correspond to the measured heating curves for distinct initial temperatures of the calorimeter. **(b)** The initial resistance of the filament $\mathbf{R_0}$, as a function of filament support temperature, **T**. The linear fit provides a simple formula for filament temperature (Eq. 2.1).

In addition to providing parameters for determining the filament temperature during rapid scans, the linear fit made it possible to gauge the impact of radiative cooling or heating of the filament at support temperatures of 100 to 170 K (see Fig. 2.7.b). As illustrated in Fig. 2.2, the filament support assembly is surrounded by six cryogenic shields consistently maintained at approximately 105 K during our experiments. As the temperature difference between the filament supports and the surrounding cryogenic shields increases, there may be concerns of significant radiative cooling of a segment of the wire. Yet if radiative cooling were to cause a temperature difference between the filament and the supports, we would observe a non-linear dependence of the filament's resistance to the support temperature. In fact (see Fig. 2.7.b), the highly linear correlation between support temperature and filament resistance confirms that the impact of radiative cooling on filament temperature is negligible.

2.7. Validation of temperature calibrations

Extensive tests of the routine temperature-resistance calibration procedure described in the preceding Sections were performed to provide verification for this routine procedure. Traditionally, the three phase transitions of cyclopentane (at approximately 122, 138 and 179 K) are used as final temperature calibration test of various calorimetric instruments in the 100 to 200 K temperature range[12]. However, two of its three transitions are characterized by exceedingly low transition enthalpies (0.3 and 0.6 kJ/mol for 138 and 179 K transitions respectively), and are therefore difficult to detect. Furthermore, these transitions were not observed in FSC thermograms measured at heating rates as low as 10^4 K/s. Therefore, other organic compounds, with melting temperatures ranging from 113.5 from 178.8 K, were examined to find convenient markers for verifying temperature

calibration tests.

Based on the results of some rather tedious experiments, we chose the following four compounds as the "standard candles" for validating the temperature measurements in our FSC experiments. These are listed in Table 2.1 along with their melting temperatures and the deposition conditions which resulted in formation of each crystalline phase. Note that some of the compounds do not crystallize readily during vapor deposition if the temperature is too low. For instance, preparation of fully crystalline methyl benzene films requires deposition temperatures in excess of 150 K, within 30 K of that compound's T_m.

Having found suitable organic crystals, we attempted to test our temperature calibration by measuring the FSC thermograms of the crystalline films at high heating rates (10^5 K/s). This approach, however, did not result in meaningful information because of two reasons. Cursory kinetic analysis of the thermograms indicated that the melting of the compounds during rapid heating followed zero-order kinetics, i.e. it originates at the surface of the crystalline films and progress into their interiors via an accelerating front (see Chapter 3). The resulting melting endotherms were characterized by a complex shape with an uncertain onset temperature. Furthermore, judging by the width of the endotherms, a part of the crystalline sample can be overheated by up to 10 K. Therefore, the following protocol was adapted for the validation of temperature calibration.

After preparation, the films were subjected to heating with the "slow" rates on the order of 2000 K/s, i.e. almost two orders of magnitude lower than the rates typically employed in our FSC experiments (10^5 K/s). The reduction of heating rate results in a decreasing melting endotherm width, to within a fraction of a Kelvin. Furthermore, instead of using the thermograms to detect a phase transition, we simply utilized classical heating

crystalline phase	T_m /K	T_d range /K	comments
isobutane	113.74	96 to 113.74	crystallizes upon VD in a wide T_d range
dimethyl ether	131.65	96 to 131.65	crystallizes upon VD in a wide T_d range
diethyl ether, β	149.86	near 135	does not crystallize at T_d below 110 K
diethyl ether, α	156.92	near 142	does not form at T_d below 142 K
methyl benzene	178.15	above 150	complete crystallization only at T_d above 150 K

Table 2.1. Crystalline organic compounds used as standards for the final validation of the temperature calibration procedure. The compounds were vapor deposited (VD) at temperatures which ensured a complete crystallization during deposition. Typical deposition temperatures ($\mathbf{T_d}$) and the literature values for the melting temperatures ($\mathbf{T_m}$) are given. The deposition rates for all samples were typically in the range from 15 to 40 nm/s. The films' thickness was on the order of 1 μm.

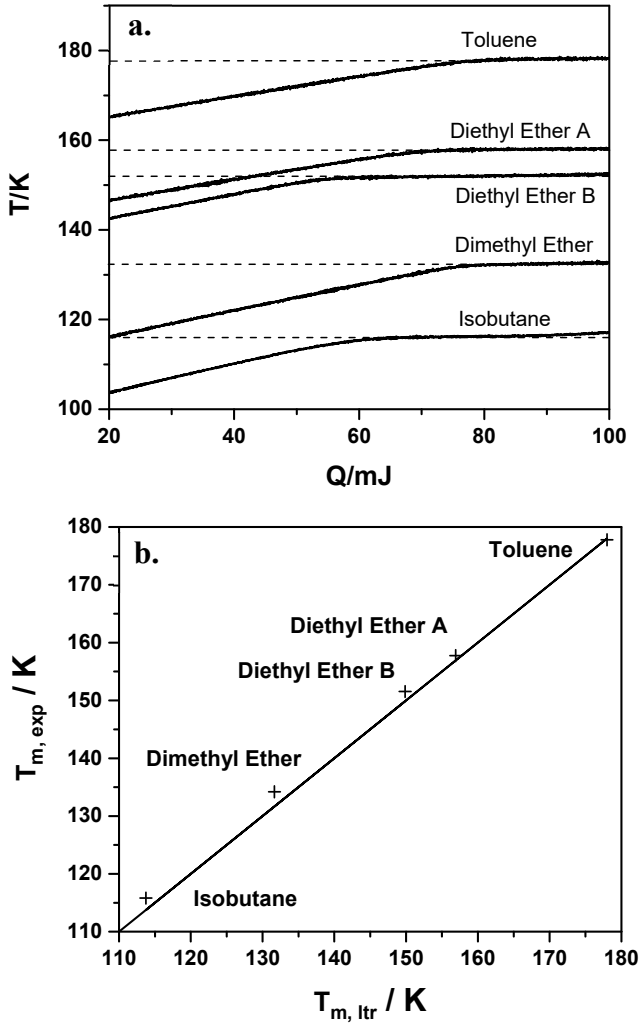

Fig. 2.8. Temperature calibration tests. Examples of heating curves (**a**) for the five crystalline compounds listed in Table 2.1. The distinct polycrystalline films were prepared by vapor deposition at temperatures that ensured complete crystallization during film growth (see Ref 2) . The films were approximately 1 μm thick and the initial heating rate were less than 2,000 K/s. The dashed lines in the top panel illustrate the inferred melting temperatures, which are also plotted as a function of the literature Tm values (b).

curves, i.e. the dependence of sample temperature on the energy generated by the heating filament.

The top panel (a) of Fig. 2.8 shows the heating curves for the five crystalline compounds in Table 2.1, with melting temperatures ranging from 113.5 to 178.8 K. As shown in the figure, the onset of melting for each compound is manifested as a sudden change in the heating curve to a plateau at a distinct temperature. The characteristic temperature of the plateau is taken to be equivalent to the apparent melting temperature of each crystalline film. The results of the heating curve analysis is summarized in Fig. 2.8.b. The apparent melting temperatures observed in our experiments are then compared to the established melting temperatures available from literature [13-16]. The excellent agreement between the apparent and literature values of T_m demonstrates that our routine temperature calibrations are valid.

Due to their complexity, such extensive tests of temperature calibration are impossible to implement routinely. However, having investigated the behavior of the apparatus's temperature measurement and control system, we developed a relatively simple, daily procedure for a quick validation of temperature calibration that requires less than 10 minutes to implement. This routine calibration test is based on measuring the FSC thermograms of two crystalline compounds, isobutane and dimethyl ether. Both crystallize readily upon deposition in a wide temperature range (see table 2.1). Thus, at any point during the experiments, the heater can be switched off, and, as the calorimeter temperature decreases below 110 K, a micrometer scale film of either crystalline isobutane or dimethyl either can be prepared using high deposition rates. Thermograms of the two samples can then be measured using our standard high heating rate (10^5 K/s).

As shown in Fig. 2.9 and discussed in detail in Chapter 3 of this Dissertation, the thermograms of crystalline isobutane and dimethyl either are characterized by melting endotherms with sharp leading edges. Furthermore, despite some crystal overheating, melting follows zero-order kinetics over the temperature interval of approximately 5 K, starting from the onset of melting. The results emphasize that temperature calibration errors as small as 0.5 K would result in significant variation in the position and slope of the melting endotherms[1] shown in Fig. 2.9. Therefore, the melting endotherms can be used as an *etalon* to quickly and easily validate the temperature calibration at any point during fast scanning calorimetry experiments.

2.8. Temperature gradients and lags

The high heating rates (up to 10^5 K·s^{-1}) of our FSC approach are essential to the experiments described in this Dissertation, from the superheating of molecular crystals (Chapter 3) to taking ordinary or vapor deposited amorphous phases far from equilibrium (Chapters 4-6). Additionally, the high heating rates increase the signal-to-noise ratio of our FSC thermograms. We recognize that this may raise concerns about the potential impact of transverse temperature lags and thermal gradients on our results. In an attempt to keep thermal lags below a fraction of a Kelvin, we choose both a maximum film thickness and a maximum heating rate after a careful analysis of heat conduction in the molecular films used for FSC experiments. The analysis is based on a comparison between the thermal equilibration time, τ_{vib}, of the crystalline films and the characteristic time, t_{exp}, of the experimental measurements. We approximate t_{exp} with 1K divided by the heating rate (see Fig. 3.1.b or 4.1.c or 5.3.a for examples), our typical rates of 10^5 K·s^{-1} result in an experimental time of 10 μs at the *start* of each FSC scan. Note that our quasi-adiabatic

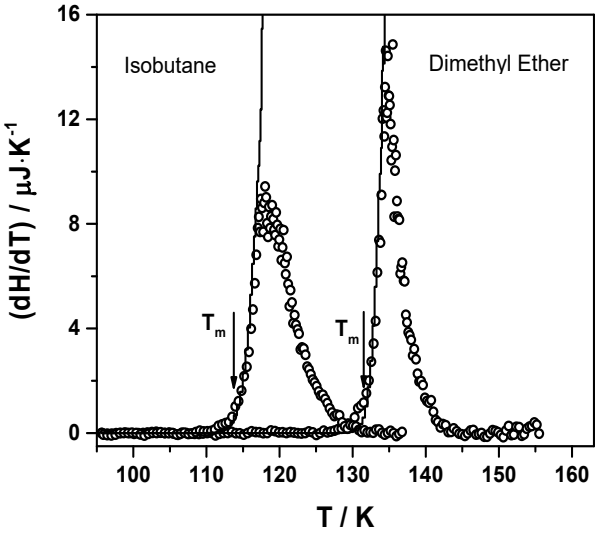

Fig. 2.9. The FSC melting endotherms of 1-μm-thick films of crystalline isobutane and dimethyl ether measured with heating rates of approximately 10^5 K/s (open circles). The black lines model the rate of surface-facilitated melting, as described in Chapter 3 of this dissertation. The literature melting points are marked as arrows. Temperature offsets as small as 0.5K, from calibration errors or other factors, would result in a marked shift of the melting endotherms.

experiments have negligible thermal losses on a time scale of several seconds. The clear condition for avoiding significant thermal lags during heating is to ensure that t_{exp} always exceeds τ_{vib}.

We obtain the typical thermal equilibration time, τ_{vib}, for molecular films on the surface of a cylindrical filament by using the two-dimensional Einstein-Smoluchowski equation for thermal transport[17]:

$$\tau_{vib} \approx \frac{L^2}{4D_{th}}, \quad (2.6)$$

where L is the thickness of the film, and D_{th} is the material's thermal diffusivity[18]. For the typical low-molecular-weight organic compounds utilized in our FSC experiments[19], the thermal conductivities of the organic *liquids* range from 0.16 to 0.24 $W \cdot m^{-1} \cdot K^{-1}$, while their volumetric specific heat capacities range from 1.2 to 1.9 $J \cdot K^{-1} \cdot cm^{-3}$. Thus (see Eq. 7.2), the resulting D_{th} is approximately 10^{-7} $m^2 \cdot s^{-1}$ for all of the low molecular weight organic *liquid* compounds discussed in this Dissertation, and this value is higher for glassy and crystalline phases. Therefore, using Eq. 2.6 for a 1-μm-thick molecular film yields 2.5 μs for τ_{vib}, which is 4 times smaller than the typical t_{exp}. Therefore, to maintain thermal lags below 1 K during FSC experiments with heating rates of 10^5 $K \cdot s^{-1}$, we limit the thickness of our samples to below 2 μm. The absence of thermal lags and gradients was verified during experiments by changing the films' thickness and the heating rate. These tests confirm that the impact of thermal lags on FSC thermograms is negligible as long as the film thickness is below two micrometers.

While the transversal temperature gradients discussed in the preceding paragraphs are relatively easy to characterize, determining the presence of a longitudinal temperature gradient between the filament supports does pose some challenge. There are two

approaches to verifying that the longitudinal gradient is less than 1 K. Both approaches require preparing a single sample film, as described immediately below.

For the first approach, we prepare a crystalline isobutane film. We must point out that the width of the endothermic transition from a fully crystalline to a fully liquid state, as observed in our near-equilibrium melting experiments (see Fig. 3b in Ref [2]) represents an upper estimate of longitudinal temperature gradients during deposition. This conclusion is based on the following argument. Let us assume that the formation of fully or partially liquid isobutane films is impossible during vapor-deposition at temperatures below the melting point of this particular compound. Consequently, the formation of a partially liquid film can be observed only when a part of the filament is above melting temperature and part is below T_m, i.e. only if there is a temperature gradient along the filament. Therefore, as the deposition temperature is increased, the transition from fully crystalline to fully liquid sample must occur over the temperature interval equal to the longitudinal gradient. Based on previous analysis (see Fig. 3 in Ref [2]), we conclude that the longitudinal temperature gradients during film deposition are less than 1 K, when the RTD readings of the supports are kept within 0.2 K of each other.

For the second approach, we prepare vapor-deposited amorphous films of methyl benzene (MB). As described in Chapter 5, for stable VD phases of MB, the onset temperature of the softening endotherms is highly sensitive to the deposition temperature, T_d. An example is illustrated in Fig. 2.10; when the temperatures of the supports are approximately equal, the width of the endotherm is less than 2 K. However, when the temperatures of the supports are set to values 2 K apart, the resulting endotherm broadens dramatically. Therefore, vapor-deposited, non-crystalline methylbenzene films of high

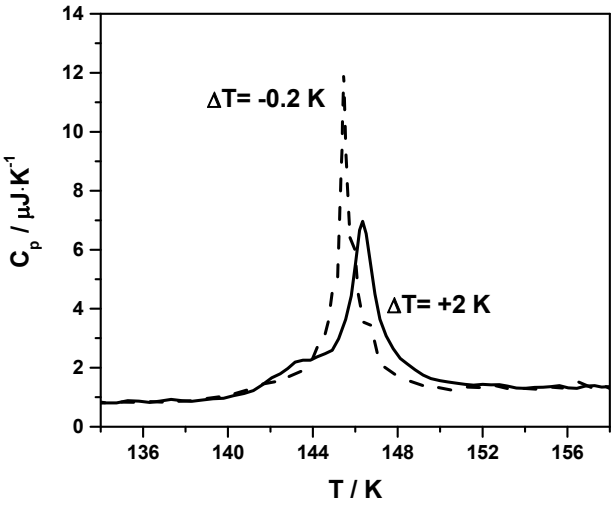

Fig. 2.10. Illustration of the impact of the longitudinal gradients (ΔT) on the FSC thermograms of micrometer thick films of stable vapor-deposited non-crystalline methyl benzene. The films were prepared at 112 K with a deposition rate of 15 nm/s. When the longitudinal gradient is kept at a minimum value (±0.2 K), the width of the fast relaxation endotherm is less than 1 K (see dashed line). However, introducing the gradient as small as ± 2 K leads to significant broadening and distortion of the FRE (solid line).

kinetic stability can be used to quickly test for longitudinal gradients in thin-wire calorimeters. This test would also work in fast scanning calorimeters of other designs.

Needless to say, we performed tests for temperature lags and gradients, as well as tests of our temperature calibrations on a routine basis. Therefore, the T_d and T(t) temperatures reported in the experiments described within this Dissertation are accurate to within a few tenths of a Kelvin.

2.9. References for Chapter Two

1. Bhattacharya, D.; Cubeta, U.; Sadtchenko, V., Fast Scanning Calorimetry–Fast Thermal Desorption Technique: The Thin Wire Approach. In *Fast Scanning Calorimetry*, Schick, C.; Mathot, V., Eds. Springer International Publishing: 2016; pp 151-186.
2. Bhattacharya, D.; Sadtchenko, V., Enthalpy and high temperature relaxation kinetics of stable vapor-deposited glasses of toluene. *The Journal of Chemical Physics* **2014,** *141* (9), 094502.
3. Schick, C.; Mathot, V., *Fast Scanning Calorimetry*. Springer International Publishing: 2016.
4. Schroter, K., Characteristic length of glass transition heterogeneity from calorimetry. *Journal of Non-Crystalline Solids* **2006,** *352* (30-31), 3249-3254.
5. Mazinani, S. K. S.; Richert, R., Enthalpy recovery in glassy materials: Heterogeneous versus homogenous models. *Journal of Chemical Physics* **2012,** *136* (17).
6. Wang, L. M.; Velikov, V.; Angell, C. A., Direct determination of kinetic fragility indices of glassforming liquids by differential scanning calorimetry: Kinetic versus thermodynamic fragilities. *Journal of Chemical Physics* **2002,** *117* (22), 10184-10192.
7. Krein, P. T., Elements of Power Electronics. Oxford University Press: 1998; pp 395-400.
8. Reed, R. P.; Clark, A. F.; Metals, A. S. f., *Materials at low temperatures*. American Society for Metals: 1983.
9. Martienssen, W., The Elements. In *Springer Handbook of Condensed Matter and Materials Data*, Martienssen, W.; Warlimont, H., Eds. Springer Berlin Heidelberg 2005; pp 114-117.
10. Lee, G. *Materials for Ultra-High Vacuum*; Fermi National Accelerator Laboratory: Batavia, Illinois, August 15, 1989, 1989; p 3.

11. Moore, J. H.; Davis, C. C.; Coplan, M. A.; Greer, S. C., Building Scientific Apparatus 4ed.; Cambridge University Press: 2009.

12. Jakobi, R.; Gmelin, E.; Ripka, K., High-precision adiabatic calorimetry and the specific heat of cyclopentane at low temperature. *Journal of Thermal Analysis* **1993,** *40* (3), 871-876.

13. Yamamuro, O.; Tsukushi, I.; Lindqvist, A.; Takahara, S.; Ishikawa, M.; Matsuo, T., Calorimetric study of glassy and liquid toluene and ethylbenzene: Thermodynamic approach to spatial heterogeneity in glass-forming molecular liquids. *Journal of Physical Chemistry B* **1998,** *102* (9), 1605-1609.

14. Ihmels, E. C.; Lemmon, E. W., Experimental densities, vapor pressures, and critical point, and a fundamental equation of state for dimethyl ether. *Fluid Phase Equilib.* **2007,** *260* (1), 36-48.

15. Counsell, J. F.; Lee, D. A.; Martin, J. F., Thermodynamic properties of organic oxygen compounds. Part XXVI. Diethyl ether. *Journal of the Chemical Society A: Inorganic, Physical, Theoretical* **1971,** (0), 313-316.

16. Aston, J. G.; Kennedy, R. M.; Schumann, S. C., The Heat Capacity and Entropy, Heats of Fusion and Vaporization and the Vapor Pressure of Isobutane. *Journal of the American Chemical Society* **1940,** *62* (8), 2059-2063.

17. Berghout, S. The Einstein Smoluchowski Equation in the One Dimensional Exclusion Process. Utrecht University, 2013.

18. Pope, J. E., *Rules of Thumb for Mechanical Engineers - A Manual of Quick, Accurate Solutions to Everyday Mechanical Engineering Problems*. Elsevier: 1997; p 14.

19. Bruce, E. P.; George, T.; Daniel, G. F.; Richard, L. R.; W. Vincent, W., Physical and chemical data. In *Perry's Chemical Engineers' Handbook, Eighth Edition*, Don, W. G.; Robert, H. P., Eds. McGraw Hill Professional, Access Engineering: 2008; pp 165-170.

Chapter Three: Non-equilibrium melting of superheated molecular crystals

Preface: This Chapter is a modified version of the manuscript published[5] in the Journal of Chemical Physics with co-authors Deepanjan Bhattacharya and Vladislav Sadtchenko. Additionally, I would like to thank a Johaness Ossorio and Max Piroshky for their participation in experiments and data analysis. I am also grateful to Dr. A. Toda and Dr. J. Hoyt, as their comments and discussion of the results reported in this Chapter were particularly helpful.

In addition to probing glass-softening kinetics and almost by default, the FSC apparatus described in Chapter 2 is capable of studying another non-equilibrium process: the melting of superheated molecular crystals. Unlike the kinetic phase transitions of glass hardening or softening, the first-order phase transitions between crystalline and liquid materials are fairly well understood. Even under non-equilibrium conditions, i.e. at temperatures not equal to the melting point, there are well-established models for melting and crystallization. At the same time, due to a shortage of experimental results on the melting kinetics of *superheated* crystalline materials, there is still a degree of ambiguity about the validity of current theoretical models for this important phenomenon. For example, it is often assumed that, under conditions of superheating, the limiting step for the phase transformation is simply self-diffusion of constituents (molecules or atoms) in the melt. However, no rigorous experimental tests of this "obvious" assumption were conducted in the past due to the difficulties involved in achieving a high degree of superheating under controlled conditions. In short, an FSC study of melting kinetics under

conditions of rapid heating serves, simultaneously, as an excellent demonstration of the FSC technique's capabilities and as a way to address possible misconceptions about the limiting steps of transformation in both crystalline and non-crystalline phases. The current theoretical debate and the utility of researching the melting of superheated crystalline materials are reviewed in detail in the proceeding Section.

3.1. Overview

The behavior of crystalline materials under conditions of superheating is a fascinating research field with a significant impact in both fundamental and applied material sciences. Understanding how crystals melt at temperatures above their equilibrium melting points, T_m, has practical applications in fields such as chemistry of energetic materials[6], laser or electron beam machining and welding[7], laser desorption-ionization mass-spectrometry[8], and the synthesis of nanoparticles by exploding wire methods[9]. From the fundamental viewpoint, experimental and theoretical investigations of superheated crystalline materials are important because they may speed the development of generalized theoretical approaches to studying a variety of other non-equilibrium processes, such as glass softening[10-12].

Despite possible benefits, research on the kinetics of phase transitions in superheated crystalline phases is limited. Under routine conditions, melting often originates at the crystalline free surface and the solid-liquid interface progresses into the bulk via a melting front[13-15]. This particular, *heterogeneous* melting mechanism makes it difficult to overheat crystalline samples beyond T_m using conventional techniques such as differential scanning calorimetry. Note that our definition of heterogeneous melting is distinct from that of the classical nucleation theory for phase transitions, where

heterogeneous nucleation sites may include bulk defects, grain boundaries, and chemical impurities, in addition to the sample surfaces. Although homogeneous melting has been investigated both experimentally[16-17] and computationally[18-19], the majority of publications on heterogeneous melting are simulations of surface pre-melting and of the initial stages of superheated surface melting in metals[20-22], model atomic crystals[23-26], or simple covalent solids[27-30].

Besides the experimental challenges, there is decreased research interest in studying heterogeneous melting because of the perception that the kinetics of non-equilibrium, surface-facilitated, condensed phase transitions are trivial. The classical Wilson-Frenkel (WF) model[31-34] of heterogeneous crystallization can also be used to describe the kinetics of heterogeneous melting. When the degree of superheating (or supercooling), ΔT, is a small fraction of T_m, the model postulates that the front velocity, ϑ_f, of melting (or crystallization) can be estimated as:

$$\vartheta_f(T) = \vartheta_{f,0} \times e^{-\frac{E_D(T)}{kT}} \times \left(1 - e^{-\frac{\Delta\mu(T)}{kT}}\right). \quad (3.1)$$

In Eq. 3.1, $\vartheta_{f,0}$ is a temperature independent coefficient, $\Delta\mu(T)$ is the chemical potential difference between the liquid and the solid, and $E_D(T)$ is the activation energy barrier to self-diffusion in the *equilibrium* melt. The term in parentheses is the thermodynamic driving force (TDF) for transformation. According to Eq. 3.1, the primary barrier to front propagation is E_D. Furthermore, in the limit of small ΔT, Eq. 3.1 can be approximated[25, 35] as a linear function of overheating, ΔT:

$$\vartheta_f(T) = \mu_f \times \Delta T\,, \quad (3.2)$$

where μ_f is a kinetic coefficient, which is weakly dependent on temperature[36]. It is important to mention that Eq. 3.1 and Eq. 3.2 both focus on the crystal-melt interface

propagating through an infinite, bulk material. Therefore, the Wilson-Frankel model does not include any details on the initial stages of the melting process, such as surface or interfacial premelting.

Despite the success of current computational and theoretical studies in capturing details of heterogeneous melting transitions in metals and other atomistic systems, it would be surprising if this linear dependence of $\vartheta_f(T)$ on superheating ΔT is universal. In other words, it is unclear if Eq. 3.2, or even Eq. 3.1, would apply to a broad range of chemically, dynamically, and structurally complex systems. Recently, fast scanning calorimetry (FSC) studies on a number of distinct crystalline polymers[37-40] have shown that $\vartheta_f(T)$ *does not* comply with Eq. 3.2. For these systems, $\vartheta_f(T)$ appears to have a power law dependence on ΔT, which indicates the existence of significant kinetic activation barriers to heterogeneous melting. In short, the non-linear dependence of melting rates in polymers emphasizes the need for further research on heterogeneous melting of superheated crystalline phases. Fast scanning calorimetry is well-suited for this challenge.

3.2. Experimental apparatus

All experiments in this Dissertation Chapter were conducted utilizing the custom-built, adiabatic, fast scanning calorimetry (FSC) apparatus that is described extensively in Chapter 2. The data acquisition system, vapor deposition source, and calibrations are all identical to the description provided in Chapter 2. Therefore, I proceed with the choice of the compounds, preparation protocols, and the specifics of data analysis.

	IB	**DE**	**MB**	**2P**
CAS No.	75-28-5	115-10-6	108-88-3	67-63-0
Formula	$(CH_3)_2CHCH_3$	CH_3OCH_3	$C_6H_5CH_3$	$(CH_3)_2CHOH$
MW, $g \cdot mol^{-1}$	58.12	46.07	92.14	60.10
$\mathbf{T_m}$, K	113.7	131.7	α: 178.2	185
$\boldsymbol{\rho_{liq}}$, $g \cdot cm^{-3}$ at T_m	0.740	0.873	0.975	0.877
$\boldsymbol{\rho_{xtal}}$, $g \cdot cm^{-3}$ *(*at T*)*	--	0.975 (93 K)	α:1.069 (150 K)	0.957 (180 K)
$\mathbf{\Delta H_m}$, $kJ \cdot mol^{-1}$	4.56	4.94	6.61	5.41
$\mathbf{\Delta H_{vap}}$ at T_m, $kJ \cdot mol^{-1}$	26.9	26.0	40.6	50.3
$\mathbf{T_g}$, K	--	--	117.2	115
Fragility ($\mathbf{m_A}$)	--	--	107	55
$\mathbf{E_{\alpha d}}$ at T_m, $kJ \cdot mol^{-1}$	--	--	~ 30	~ 30
$\mathbf{E_m}$, $kJ \cdot mol^{-1}$	**116**	**131**	**200**	**85**

Table 3.1. Thermodynamic and kinetic properties for the condensed phases of the compounds used in the reported FSC experiments with isobutane (IB), dimethyl ether (DE), methyl benzene (MB), and 2-propanol (2P). See text for details and references. The data are compiled from Ref. [1-4]

3.3. Choice of polycrystalline materials and film preparation protocol

Motivated by the fundamental importance of research on phase transitions under non-equilibrium conditions and the general scarcity of experimental studies on superheated crystalline phases, we have investigated the melting kinetics of low-molecular-weight (LMW) organic crystals using our adiabatic, FSC technique[41]. In this Dissertation Chapter, we describe our preliminary findings from experiments with micrometer-scale, polycrystalline films of isobutane (IB), dimethyl ether (DE), methyl benzene (MB), and 2-propanol (2P), as listed in Table 3.1. We choose these particular materials because of the obvious data gap on heterogeneous melting kinetics for systems of intermediate structural complexity. With distinct molecular geometries and intermolecular interactions, the complexity of chosen LMW crystal structures is significantly higher than that of Leonard-Jones atomic metals. Yet, these crystals are less structurally and dynamically complicated than polymers, and are therefore amenable to extensive computational studies. Furthermore, this set of compounds has significant variation in molecular structure (alkane, ether, aromatic, vs. alcohol), intermolecular interaction (e.g. Van-der-Waals vs. hydrogen bonding), and dynamic properties of the liquid phase (i.e. liquid fragility)[10, 12]. Finally, the equilibrium melting points of these compounds are within the temperature range accessible by our FSC apparatus, which are discussed in Sections 2.2 and 2.6.

Polycrystalline sample films were prepared by vapor deposition with a typical vapor flux of approximately 15 nm/s. The complete crystallization of the samples was ensured by setting the deposition temperature to 10 to 30 K below the T_m of each compound[41-42]. The thickness of polycrystalline film varied from 0.5 to 2 μm, limiting the possible grain size of the crystals to a micrometer length scale. As described in later

Sections of this Chapter, the thickness of the films, and therefore grain size, did not have a significant impact on the kinetic results.

The films' complete crystallization was routinely verified. We emphasize that our FSC technique is highly sensitive to the sample's phase composition[41], because it greatly impacts the FSC thermograms. For example, a supercooled liquid or an amorphous fractions in the sample would yield distinct fast relaxation endotherms (FRE)[41-43] at temperatures significantly below T_m. Therefore, the absence of FREs prior to melting is clear evidence for the sample's high crystallinity. The extent of crystallization was also quantified by comparing the films' melting enthalpies, calculated by $C_p(T)$ integration, with literature data. Finally, complete crystallization was confirmed by a lack of variation in the melting endotherm with deposition conditions and the sample's thermal history (see, for example, Fig. 2 of Ref. [43]). As expected, changes in a sample's preparation protocol, such as extended annealing of the crystalline films or variations in the vapor deposition rate, had no impact on the melting endotherms for all of the compounds studied.

3.4. Thermogram analysis

The apparent heat capacity thermograms for the polycrystalline films were obtained as described in Section 2.5 of this Dissertation. Data for multiple samples interrogated under identical experimental conditions was occasionally averaged or concatenated to improve the signal-to-noise ratio and the temperature resolution of the thermograms.

Fig. 3.1 illustrates the typical analysis used to infer the absolute melting rates from thermograms of LMW polycrystalline films. In this particular case, the sample is a 0.6 μm thick polycrystalline film of isobutane (IB). Fig. 3.1.a shows that, in a temperature range close to IB's melting point, the FSC thermogram is dominated by a large, fast-melting-

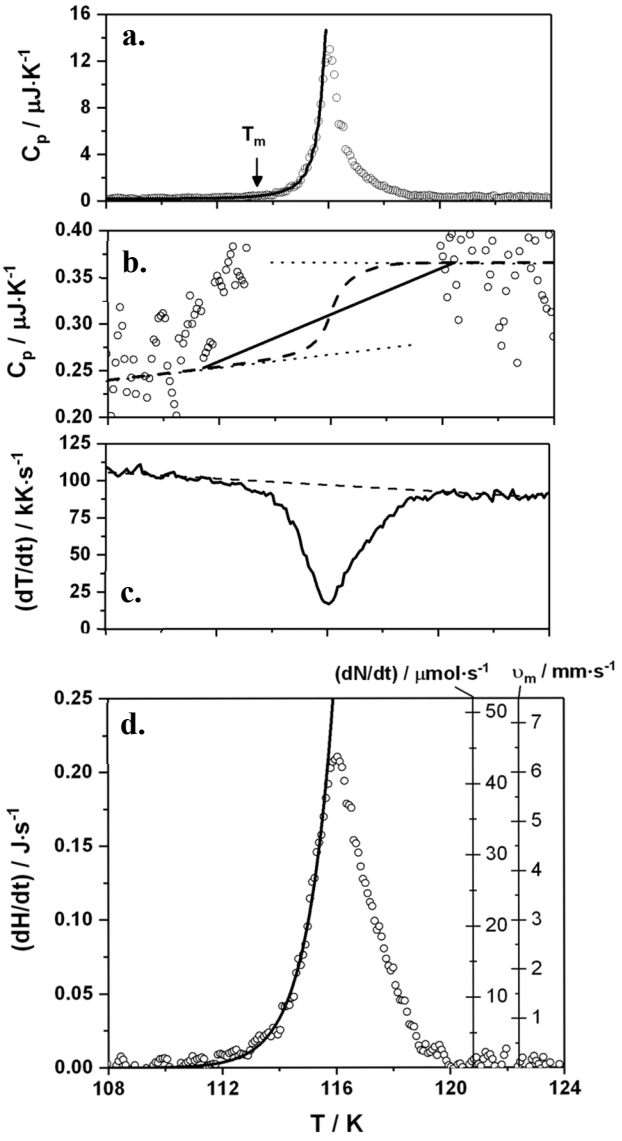

Fig. 3.1. Typical analysis of the FSC thermograms of polycrystalline materials. This example is for a 0.6 μm thick polycrystalline film of isobutane. **(a.) Circles** illustrate the apparent heat capacity of the film. The peak is the melting endotherm and the solid line is an eye guide. **(b.)** The simple (**solid**) and sophisticated **(dashed)** baselines used for inferring the excess heat capacity, dH/dT, from the thermogram **(circles)**. **(c.)** The heating rate during the sample's melting, with a dashed eye guide. **(d.)** The resulting heat flow, dH/dt, are plotted **(circles)** as function of temperature, during non-isothermal melting. The **solid** line is the Arrhenius fit of the heat flow data. The bars on the right side of the lowest panel show our estimates, relaying on parameters from Table 3.1, of the absolute melting rate, **dN/dt**, and the estimated melting front velocity, υ_m.

endotherm (FME) with an onset near 113.5 K. This rapid, non-linear increase in $C_{p,a}(T)$ continues until 116 K, where the remaining portion of the crystalline phase is superheated by 2.5 K. At 116 K, the *apparent* heat capacity reaches a maximum, and begins to decrease rapidly. The melting is complete near 120 K, where the $C_{p,a}(T)$ becomes nearly independent of temperature (see Fig. 3.1.b). As shown later in Fig. 3.2.a, the melting endotherm is then followed by a liquid vaporization endotherm at higher temperatures.

As illustrated in Fig. 3.1.b, we begin our analysis with a standard assumption that, in the temperature range of transformation (116 ± 4 K), the overall $C_{p,a}(T)$ must consist of two contributions. The first is the true heat capacity of the melting sample, $C_p(T)$, and the second is the excess heat, $(dH/dT)_{ex}$, which arises from increased heat flow into a sample undergoing an endothermic transformation. As we explain later (see Eq. 3.3 and Eq. 3.4), the $(dH/dT)_{ex}$ values serve as the primary data for inferring the absolute melting rates. Therefore, we continue by estimating the true heat capacity of the melting film.

In the simplest case, we approximate the true $C_p(T)$ of the partially melted IB samples by a straight line, which connects the sample's $C_p(T)$ in its fully crystalline and completely melted states (see solid line in Fig. 3.1.c). We assume that, in the short temperature intervals prior to and after melting, the $C_p(T)$ can be approximated by a linear function for the crystalline film and a constant for the melted film (dotted lines in Fig. 3.1.b). Subtracting this "baseline" $C_p(T)$ from the FSC thermogram yields $(dH/dT)_{ex}$. Although we developed a more sophisticated model of the melting sample's true heat capacity (see dashed line in Fig. 3.1.b), using this alternative "baseline" has an insignificant impact on the essential conclusions of our investigation, since the variations are negligible compared to the FME's magnitude (see Fig. 3.1.a).

To obtain the rate of excess heat flow, $(dH/dt)_{ex}$, into the film during melting, we multiply $(dH/dT)_{ex}$ by the film's heating rate, dT/dt (see Fig. 3.1.c). According to the central assumption of thermal analysis[44], the absolute rate of transformation is proportional to excess heat flow:

$$\frac{dN}{dt}(T) = \frac{1}{\Delta H_m} \times \left(\frac{dH}{dt}\right)_{ex}(T), \quad (3.3)$$

where dN/dt is the number of crystalline constituents entering the melt per unit of time and ΔH_m is the melting enthalpy per constituent, which is nearly constant over ΔT. Note that dN/dT is proportional to the melting front velocity, ϑ_f, in the case of heterogeneous melting. As illustrated in Fig. 3.1.d, the micrometer scale polycrystalline IB sample shows a *non-linear* temperature dependence for the $(dH/dt)_{ex}$ and, consequently, for the melting rate. In fact, an Arrhenius temperature dependence[45] of the heat flow:

$$\left(\frac{dH}{dt}\right)_{ex}(T) = \left(\frac{dH}{dt}\right)_0 \times e^{-\frac{E_m}{RT}}, \quad (3.4)$$

provides the best fit to the melting data. In Eq. 3.4, $(dH/dt)_0$ is a constant and E_m is the apparent activation energy barrier for the melting of superheated crystals. In short, the kinetics of superheated melting for LMW molecular polycrystalline films are significantly distinct from those predicted for atomic crystals and for polymers (see Eq. 3.2).

3.5. Validating thermogram analysis

Before elaborating on the origins of the observed kinetics, we would like to present verification of our melting endotherm analysis with the kinetic analysis of another phase transition: the free vaporization of fully melted films. The free-vaporization endotherm (FVE) follows the fast melting endotherm in the FSC thermograms, as illustrated in

Fig. 3.2.a for our example isobutane film. Unlike non-equilibrium melting and other condensed phase transitions, free vaporization is well understood[46-47]. Note that free vaporization, which occurs without gas phase collisions and backscattering, is another advantage of using a thin filament as the film substrate[48]. Vaporization must originate at the free surface and this liquid-vacuum interface progress into the bulk via a "vaporization front". Thus, examining the FVE's can verify the essential assumptions of our analysis and our FSC technique and data analysis.

Numerous past temperature programed desorption studies under high vacuum conditions have demonstrated that free-vaporization follows zero-order kinetics during heating [46, 49-50]. The kinetics of a chemical or physical transformation process are zero-order when the rate of transformation, *dN/dt*, is independent[45] of the number of transformed constituents for a large *N*. In other words, when the rate law is

$$\frac{dN}{dt}(T) = k(T) \times N^0, \quad (3.5)$$

where *k(T)* is a temperature-dependent constant. For phase transitions of non-reactive, single constituent systems, zero-order kinetics are observed when a transformation proceeds *irreversibly* via a moving boundary between two phases, i.e. in a monolayer-by-monolayer fashion. Under isothermal conditions, the flux of constituent entering the new phase remains constant when the molecular density and the interface area do not change. For example, in the case of irreversible desorption of a multilayer molecular film in vacuum, the surface number density of constituents is independent of the extent of vaporization despite monolayer-by-monolayer removal of the material. Under non-isothermal conditions, the rate of vaporization increases with temperature and is well approximated by an Arrhenius rate law[45, 50], as long as the surface area of the vaporizing

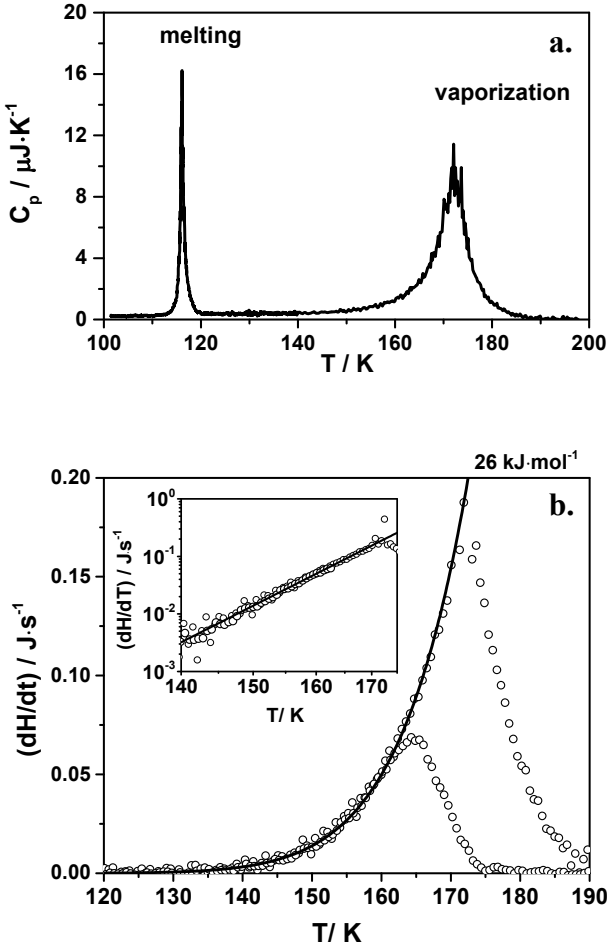

Fig. 3.2. Kinetic analysis of the *vaporization* of a liquid IB film. **(a.)** The FSC thermogram with two endotherms due to melting and vaporization of micrometers scale film. **(b.) Circles** show the excess heat flow, dH/dt, into the samples during vaporization inferred from the melting endotherms of 300 and 600 nm thick IB films. The inset shows the rate of vaporization as a function of temperature in the Arrhenius coordinates. The vaporization rate is assumed proportional to the dH/dt values. The Arrhenius fit of the data in the inset results in 26 kJ·mol^{-1} for the activation energy of IB vaporization. This fit is plotted as the **solid line** in both (b.) and its inset.

film remains constant. Furthermore, the apparent activation energy, E_{vap}, should be nearly equal to literature values for the enthalpy of vaporization, ΔH_{vap}.

Fig. 3.2 shows the results of the thermogram analysis performed on the FVE's of two isobutane films with distinct thicknesses (0.3 and 0.6 μm). The analysis is conceptually identical to that illustrated in Fig. 3.1. As shown in Fig. 3.2, the leading edges of $(dH/dt)_{ex}$ for vaporization are both well fit by a single Arrhenius equation; i.e. the transformation follows zero-order rate kinetics. Furthermore, the E_{vap} of 26±1 kJ·mol^{-1} is in excellent agreement with the near- equilibrium[2] ΔH_{vap} value of 26.9 kJ·mol^{-1} for temperature range of 120 to 187 K. Note that E_{vap} for methylbenzene also matched[42] (within 2 kJ·mol^{-1}) the compound's ΔH_{vap} near T_m.

Based on the observations described in the preceding paragraphs, the following four conclusions assert the suitability of our experimental and analytical FSC technique for studying phase transitions. *(i.)* Typical of thermal analysis, the inferred $(dH/dt)_{ex}$ values represents phase transformation rates of condensed-phase films. *(ii.)* When the leading edges of $(dH/dt)_{ex}$ overlap for films of differing thicknesses, the phase transition under investigation *must be* heterogeneous; i.e. it progresses from the film's free surface into the sample bulk and follows zero-order kinetics. *(iii.)* Although the FSC technique uses heating rates which are much higher than those of near-equilibrium studies (i.e. traditional temperature programed desorption and differential scanning calorimetry), it is perfectly capable of extracting physically meaningful and correct kinetic parameters for condensed phase transitions (i.e. process activation energies) as confirmed by vaporization endotherm analysis. *(iv.)* Lastly, the near-perfect leading-edge overlap of $(dH/dt)_{ex}$ for our thickest and thinnest condensed phase films *unambiguously* demonstrates that temperature gradients

and lags are negligible (less than 0.2 K) in our thin-wire FSC experiments. We emphasize that this conclusion is in accord with our past temperature calibrations and characterizations of thermal lags, thermal conductance barriers, and temperature gradients in the films of LMW materials[41-42] with thicknesses below 1.5 μm. It is also in agreement with our estimates of thermal lags and gradients, as described in Chapter 2. In summary, thin-wire fast scanning calorimetry is a perfectly suitable technique for studying the melting of superheated crystalline materials.

3.6. Melting kinetics during rapid heating

Having verified our technique, we now return to our findings on the melting kinetics of superheated low-molecular-weight crystals. Fig. 3.3 shows the excess heat flows, the absolute melting rates, and the estimated melting front velocities in IB and MB films of thickness ranging from 0.3 to 1.0 μm. The *dN/dt* and ϑ_f values were inferred from *dH/dt* data using Eq. 3.3 and Eq. 2 of Ref. [42]. For all films, the leading edges of absolute rate, *dN/dt*, overlap as predicted by zero-order kinetics. This demonstrates that the polycrystalline films melt heterogeneously and that melting is likely to originate at the free surface (film-vacuum interface), similar to irreversible vaporization of LMW films in vacuum. Melting at temperatures above T_m is likewise irreversible, as the recrystallization of a melt is thermodynamically unfeasible.

The surface origin of the melting front is further indicated by non-zero melting rates at temperatures below the compounds' equilibrium T_m (see the dashed lines in Fig. 3.3). The onset of melting at a few K below T_m is consistent with *surface premelting*: the formation of a quasi-liquid layer at the surface of the polycrystalline film[51-53]. Under

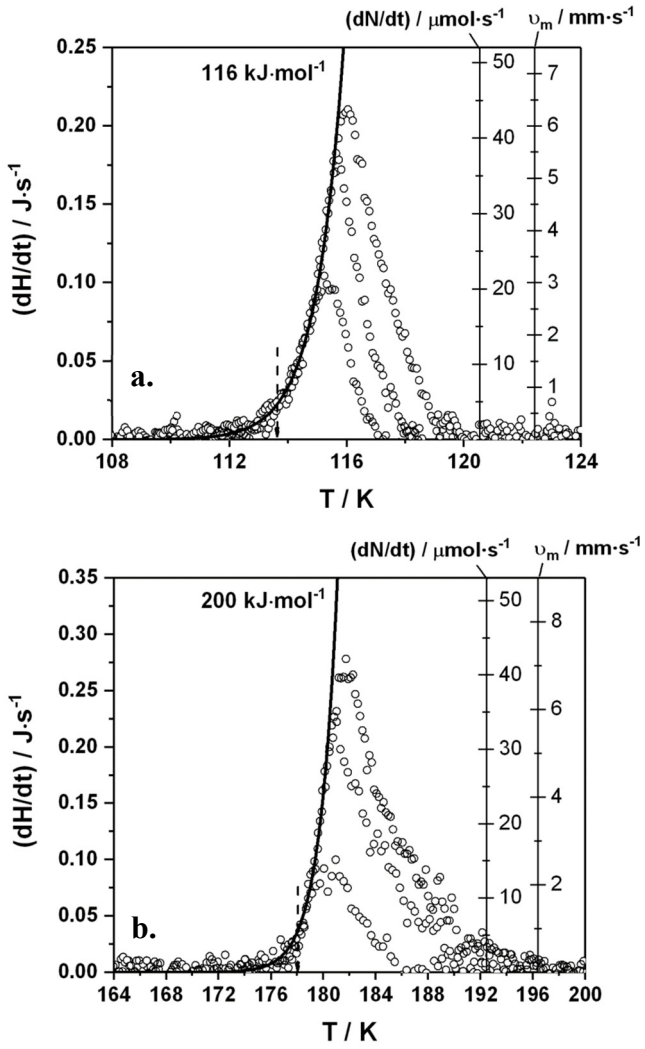

Fig. 3.3. The melting rates of IB (a) and MB (b) polycrystalline films of thicknesses ranging from 0.3 to 1.0 μm. The overlap of the leading edges of dH/dt diagrams strongly implies heterogeneous melting kinetics. The solid lines are the Arrhenius fits of the melting rate data. The apparent activation energy barriers to melting are shown next to the Arrhenius fit of the dH/dt data. The bars on the right side of the panels show our estimates of the absolute melting rate (dN/dt), and the estimated melting front velocity (υ_m).

near-equilibrium conditions, heterogeneous melting is expected to occur by the divergence of the quasi-liquid layer thickness as temperature approaches T_m. The continuous increase in the melting rate across T_m, is in qualitative agreement with this scenario.

Observation of possible premelting under conditions of rapid heating and the similarities between kinetics of melting and vaporization are not the only evidence in support of our assumption that melting of superheated crystals begins at the free surfaces of the films. Another argument in favor of the free surface origin of the melting front relies on the evidence for wetting of the filament surface by the chosen LMW compounds. The evidence arises, once again, from the observation of zero-order vaporization kinetics at temperatures tens of Kelvins above the T_ms of the compounds. If the liquids did not wet the filament, beading (droplet formation) would change the surface area of the liquid films during vaporization, making the observation of zero-order desorption kinetics unlikely. Wetting implies relatively strong attractive interactions between the molecules of the film and the tungsten oxide substrate (see Section 2.2). Therefore, it is extremely difficult to imagine that melting will initiate at the filament-film interface *in preference* to the film-vacuum interface.

Despite the arguments of the preceding paragraphs and the similarities between the kinetics of melting and of vaporization, we cannot completely rule out the possibility that melting may begin at the film-substrate interface. However, *we must emphasize that the exact origins of the melting front are not vital to our essential findings and conclusions*. In our FSC experiments, the bulk of the kinetic information on heterogeneous melting is obtained *when the melting front has already moved tens of nanometers away from the facilitating interface*. In other words, our FSC measurements explore the kinetics of

melting long past the initial interfacial premelting stage[53] and, therefore, are unlikely to be affected by the physical properties of the interface. Furthermore, *if* melting does begin at *both* the film-vacuum and the film-filament interfaces, the observed Arrhenius kinetics exclude the possibility that the melting fronts originating from these interfaces have drastically different mechanisms. In particular, the activation energy for melting front propagation must be the same for both melting fronts; only this scenario would result in a linear (Arrhenius) dependence of the combined heat flow logarithm on the inverse temperature. As I discuss in the concluding paragraphs of this Chapter, our findings are based on the values of the apparent activation energy for propagating the melting fronts, and not on the velocities of the fronts.

In an ideal zero-order kinetic process[45], the transformation rate would increase with filament temperature until the entire sample has transformed; i.e. the rate increase would be followed by a sharp cut-off at the end of transformation. However, as illustrated for both IB and MB films in Fig. 3.3, our rate diagrams do not show a sharp cut-off. Although the melting rate is Arrhenius until 30-60% of the sample has transformed, the rate decreases rapidly in the later stages of the transformation. Furthermore, in the case of 1.0 μm thick MB film, the rate decrease is not completely monotonic and has a discernable shoulder 10 K above the T_m. These non-Arrhenius features of the melting endotherms (Fig. 3.1, Fig. 3.3, and Fig. 3.4) clearly indicate that zero-order kinetics break down when the melting transformation rate is near its maximum.

Presently, we do not have a comprehensive explanation for the zero-order breakdown observed in the rate diagrams of melting condensed phase LMW organic films. It was suggested to us that this kinetic breakdown might result from insulation of the film

by a thin layer of vaporized material at the filament-film interface. However, this seems highly unlikely due to the relatively low vapor pressure of the investigated compounds at their respective T_ms and the short time-scale of our FSC experiments. For example, IB films have a saturated vapor pressure[54] of $4.65 \cdot 10^{-2}$ Pa near T_m and their heating time from 100 K to T_m is less than 200 microseconds during scans. Using the kinetic theory of gasses, we estimate that *less than 3 percent of a single IB monolayer* can vaporize during the initial stages of our FSC experiments. Because this amount of vapor is unlikely to effectively insulate the film from the filament, our alternative conjecture is that the films mechanically decouple from the filament. Temporary decoupling can result from significant differences between the thermal expansion coefficients of the tungsten filament and of the superheated polycrystalline LMW film. We emphasize that, inconsequential to the origins of the breakdown, the fact remains that melting kinetics for a significant fraction (30-60%) of the sample *are* zero-order *and* Arrhenius. As such, we will delve into the physical meaning of the inferred Arrhenius parameters under conditions of moderate superheating.

Fig. 3.4.a summarizes our rate analysis results for IB, DE, MB and 2P films. During moderate superheating, we observe zero-order Arrhenius melting kinetics for *all* samples. Although their latent heats are quite similar (see Table 3.1), the compounds have significantly distinct non-equilibrium melting activation energies, E_m. More importantly, the E_m values exceed even the vaporization enthalpies, $\Delta H_{vap}(T_m)$. These non-linear transformation rates in Fig. 3.4.a and high E_m barriers strongly imply that the linear approximation by Eq. 3.2 and even the classical Eq. 3.1 do not capture details of heterogeneous melting in molecular crystals.

In Eq. 3.1, the kinetic activation barriers for heterogeneous melting are assumed to result from self-diffusion in the *equilibrium liquid* phase at temperatures near T_m. Yet the barriers for self-diffusion at T_m in equilibrium liquid are not expected to exceed $\Delta H_{vap}(T_m)$ for molecular condensed phases[55]. In contrast to this prediction, we observe activation energy barriers that are approximately 2, 4, 5, and 6 times higher than the $\Delta H_{vap}(T_m)$ for IB, DE, MB, and 2P, respectively. The direct implication of such high activation energies is that the melting of superheated LMW crystals is *a highly cooperative process*, involving the correlated motion of a large number of constituents. In other words, for LMW crystals, the superheated melting process may bear some similarities to glass softening[56].

To elucidate the physical origins of the high barriers to heterogeneous melting, we expanded our analysis of the melting kinetics of MB and 2P films (see Fig. 3.4.b). For these particular compounds, previous broad-band dielectric spectroscopy studies[3-4] provide data on molecular dynamics of equilibrium liquids cooled below T_m. We assume that the apparent activation energies, $E_{\alpha d}$, for the dielectric α-relaxation process are comparable to the activation energy barriers of self-diffusion in the equilibrium liquid. Note that such an assumption is sound for temperatures near T_m, where decoupling of kinetic parameters is not expected[12] (see Section 1.5).

Fig. 3.5 shows the dielectric activation energies, $E_{\alpha d}$, for supercooled liquids of MB and 2P, which we estimate from an Arrhenius plot of α-relaxation times (Eq. 1.6). We note that 2P and MB have similar molecular kinetics near their equilibrium melting points (see Table 3.1). At their respective T_ms the $E_{\alpha d}$ values[3-4] are approximately 30 $kJ \cdot mol^{-1}$ for both liquid 2P and liquid MB. If, as proposed by the WF model (see Eq. 3.1), the melting front velocity is controlled primarily by the activation energy for self-diffusion in the liquid

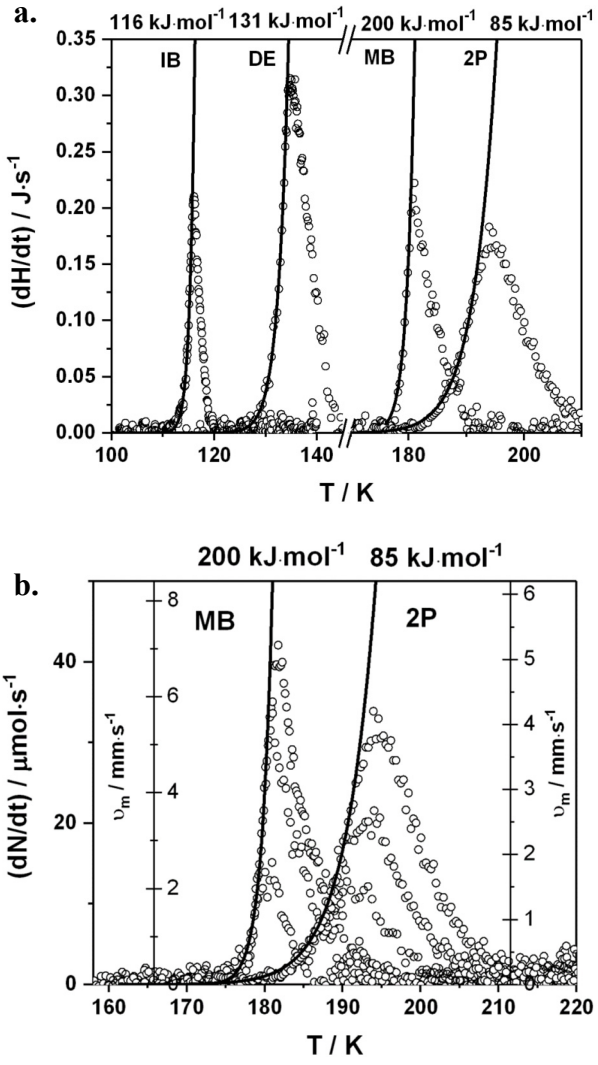

Fig. 3.4. **(a.)** The summary of the kinetic analysis of melting for micrometer scale polycrystalline films of IB, DE, MB, and 2P. With exception of 2P, the apparent activation energies of melting are 3 to 5 times greater than the respective vaporization enthalpies of the compounds. **(b.)** Comparison of the heterogeneous melting rates of MB and 2P. Despite similar equilibrium melting point and other thermodynamic parameters, the apparent melting activation energy of MB is almost three times greater than that of 2P. See text for discussion. The bars on the left, and right sides of the lower panel show our estimates of the melting front velocity (υ_m). Estimates rely on the parameters from Table 3.1.

at equilibrium, then the E_m values of 2P and MB during superheated melting would be nearly equivalent. Our experimental FSC results, however, are in stark contrast to this expectation. Indeed, the E_m of superheated 2P samples is almost 3 times the expected $E_{\alpha d}$ in the warm equilibrium liquid phase near T_m. Moreover, the E_m of MB is more than 6 times greater than the $E_{\alpha d}$ near T_m. Therefore, during superheated melting of LMW crystals, molecular diffusion in the *ordinary near-equilibrium* liquid near T_m is clearly *not* the limiting step.

Despite the lack of correlation between the E_m and $E_{\alpha d}$ values near T_m, our FSC results do not immediately annul the classical model of heterogeneous melting described by Eq. 3.1. We note that liquid 2P is significantly *less* fragile than MB. In other words, its molecular kinetics are more Arrhenius as the liquid is cooled to the glass transition temperature, T_g. The lower fragility of 2P is manifested by a weaker temperature dependence of $E_{\alpha d}$ near T_g. From the dielectric spectroscopy data illustrated in Fig. 3.5, it follows that while the $E_{\alpha d}$ in liquid MB increases by more than 6 times, it merely triples in liquid 2P in the temperature range between T_m and T_g. These observations are in qualitative agreement with the estimated fragilities of 2P[57] and MB[3] (55 and 107, respectively). Furthermore, the E_m values for superheated crystalline 2P and MB samples closely match the energy barriers for the molecular kinetics (α-relaxation rates) in their liquid phases near each compound's T_g (115 and 117 K respectively). In short, the Wilson-Frenkel model may still capture the kinetics of heterogeneous melting in superheated LMW polycrystalline films, albeit under the assumption that the amorphous phase immediately behind the propagating, solid-liquid interface is structurally and dynamically distinct from the ordinary equilibrium liquid at T_m. To be more specific: we conclude that, under

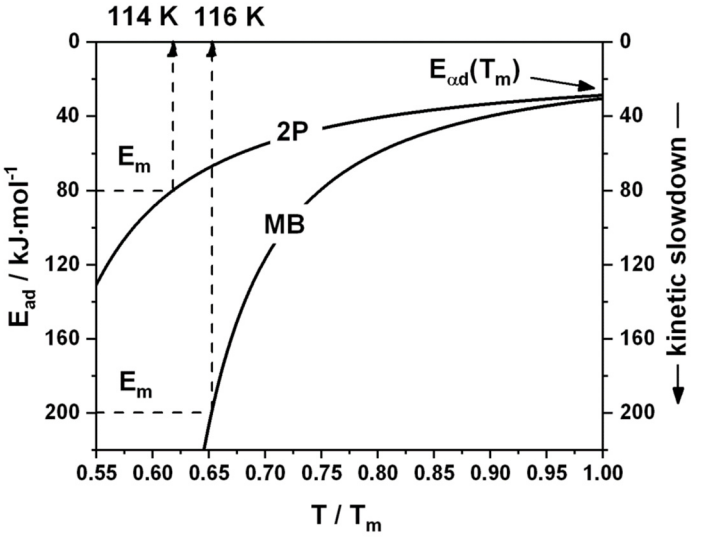

Fig. 3.5. The apparent activation energies for α-relaxation process in supercooled liquid MB and 2P. The $E_{\alpha,d}$ values are inferred from reported dielectric spectroscopy studies (see text). Comparison of the E_m and $E_{\alpha,d}$ values implies that the heterogeneous melting kinetics under conditions of rapid heating are *not* controlled by mass transport or structural relaxation in ordinary liquid at T_m. However, the energy barriers to melting are in agreement with the hypothesis that the melting kinetics are controlled by diffusion of molecules into an abnormally dense liquid. See text for discussion.

conditions of superheating, the rate of heterogeneous melting appears to be limited by diffusion into a dense, glass-like, non-crystalline phase.

We would like to elaborate further on the details and the possible physical basis of the observed kinetics. First, note that the specific volume changes are positive upon melting for all investigated compounds[2]. Thus, when melting is limited to within a few nanometers of the solid-vacuum interface, i.e. at the *onset* of transformation, the rate of liquid expansion is likely to be rapid. At this stage, the activation energy for diffusion in the melt and, consequently, the apparent E_m must be near or even less than the E_d of ordinary liquid at T_m. In fact, past molecular dynamics simulations likely capture the microscopic details for this *initial* stage of surface-facilitated phase change, as they typically investigate heterogeneous melting on a length scale of less than a few hundred angstroms and on a time scale of less than a few hundred picoseconds. However, during our experiments, Arrhenius kinetics occur over a timespan of tens of microseconds, when the solid-liquid interface has traveled hundreds of molecular layers from the sample surface. During this mesoscale transformation stage, the melt may develop a broad density gradient near the interface, and, therefore, diffusion into the dense liquid becomes the rate-limiting step to further melting (see Fig. 5.6). As research on dynamics and mobility in colloidal glasses and liquids implies, a decrease in specific volume is equivalent to a decrease in the temperature[58]. Consequently, the abnormally dense liquid interface layer may be similar to a supercooled liquid at temperatures close to T_g, where self-diffusion is cooperative and is characterized by diverging apparent activation energies[10-11].

In summary, our fast scanning calorimetry (FSC) investigations of low-molecular-weight (LMW), bulk-like, polycrystalline films demonstrate that superheated,

non-isothermal, melting kinetics are distinct from those predicted by a *direct* application of the Wilson-Frenkel theory and its derivatives. Significant kinetic activation barriers limit the melting front velocity after the transformation of a thin surface fraction (less than 100 nm). In fact, we observe apparent activation energies that are approximately 2, 4, 5, and 6 times higher than the enthalpies of vaporization for isobutane, dimethyl ether, methyl benzene, and 2-propanol, respectively (see Table 3.1). Comparison of melting activation energy barriers for liquids of distinct fragilities implicates self-diffusion into a glass-like, abnormally dense phase (compared to the melt) as the rate-limiting step to melting. According to the analysis, this phase has transport properties similar to those of a supercooled liquid near its standard glass transition temperature, T_g.

3.7. References for Chapter Three

1. Bruce, E. P.; George, T.; Daniel, G. F.; Richard, L. R.; W. Vincent, W., Physical and chemical data. In *Perry's Chemical Engineers' Handbook, Eighth Edition*, Don, W. G.; Robert, H. P., Eds. McGraw Hill Professional, Access Engineering: 2008; pp 165-170.
2. Stephenson, R. M.; Malanowski, S., *Handbook of the Thermodynamics of Organic Compounds*. Springer Netherlands: 1987.
3. DöS, A.; Hinze, G.; Schiener, B.; Hemberger, J.; Böhmer, R., Dielectric relaxation in the fragile viscous liquid state of toluene. *The Journal of Chemical Physics* **1997,** *107* (6), 1740-1743.
4. Hassion, F. X.; Cole, R. H., Dielectric Properties of Liquid Ethanol and 2-Propanol. *The Journal of Chemical Physics* **1955,** *23* (10), 1756-1761.
5. Cubeta, U.; Bhattacharya, D.; Sadtchenko, V., Melting of superheated molecular crystals. *The Journal of Chemical Physics* **2017,** *147* (1), 014505.
6. Klapötke, T. M., *Chemistry of High-Energy Materials*. De Gruyter: Berlin, Boston, 2015.
7. Li, H.; Liu, H. L.; Yu, H. H.; Huang, Y. P., The Applications of the Electron Beam Machining Technology in Research of Materials Science. In *Electronics,*

Mechatronics and Automation Iii, Ma, M.; Afrasiabi, Z.; Wu, A. F., Eds. Trans Tech Publications Ltd: Stafa-Zurich, 2014; Vol. 666, pp 17-21.

8. Norris, J. L.; Caprioli, R. M., Analysis of Tissue Specimens by Matrix-Assisted Laser Desorption/Ionization Imaging Mass Spectrometry in Biological and Clinical Research. *Chem. Rev.* **2013,** *113* (4), 2309-2342.
9. Das, R.; Das, B.; Shukla, R.; Deb, P.; Prabaharan, T.; Shyam, A., Experimental study of exploding wire method for production of metal nanoparticles. *Instruments and Experimental Techniques* **2012,** *55* (1), 131-133.
10. Hodge, I. M., Enthalpy relaxation and recovery in amorphous materials. *J. Non-Cryst. Solids* **1994,** *169* (3), 211-266.
11. Biroli, G.; Garrahan, J. P., Perspective: The glass transition. *Journal of Chemical Physics* **2013,** *138* (12), 12a301.
12. Ediger, M. D.; Harrowell, P., Perspective: Supercooled liquids and glasses. *Journal of Chemical Physics* **2012,** *137* (8), 080901-1-14.
13. Chen, Q.; Sirota, E. B.; Zhang, M.; Chung, T. C. M.; Milner, S. T., Free Surfaces Overcome Superheating in Simulated Melting of Isotactic Polypropylene. *Macromolecules* **2015,** *48* (24), 8885-8896.
14. Lutsko, J. F.; Wolf, D.; Phillpot, S. R.; Yip, S., Molecular-dynamics study of lattice-defect-nucleated melting in metals using an embedded-atom-method potential. *Physical Review B* **1989,** *40* (5), 2841-2855.
15. Stegailov, V., Homogeneous and heterogeneous mechanisms of superheated solid melting and decay. *Computer Physics Communications* **2005,** *169* (1–3), 247-250.
16. Li, B.; Wang, F.; Zhou, D.; Peng, Y.; Ni, R.; Han, Y., Modes of surface premelting in colloidal crystals composed of attractive particles. *Nature* **2016,** *531* (7595), 485-488.
17. Wang, Z.; Wang, F.; Peng, Y.; Zheng, Z.; Han, Y., Imaging the Homogeneous Nucleation During the Melting of Superheated Colloidal Crystals. *Science* **2012,** *338* (6103), 87-90.
18. Samanta, A.; Tuckerman, M. E.; Yu, T. Q.; E, W. N., Microscopic mechanisms of equilibrium melting of a solid. *Science* **2014,** *346* (6210), 729-732.
19. Delogu, F., Mechanistic Aspects of Homogeneous and Heterogeneous Melting Processes. *The Journal of Physical Chemistry B* **2006,** *110* (25), 12645-12652.
20. Yang, X. Y.; Wu, D., The melting behaviors of the Nb(110) nanofilm: a molecular dynamics study. *Appl. Surf. Sci.* **2010,** *256* (10), 3197-3203.

21. Wejrzanowski, T.; Lewandowska, M.; Sikorski, K.; Kurzydlowski, K. J., Effect of grain size on the melting point of confined thin aluminum films. *J. Appl. Phys.* **2014,** *116* (16), 7.

22. Celestini, F.; Debierre, J. M., Measuring kinetic coefficients by molecular dynamics simulation of zone melting. *Physical Review E* **2002,** *65* (4), 041605.

23. Chung, J. D., Molecular dynamic simulation of the melting and solidification processes of argon. *J. Mech. Sci. Technol.* **2009,** *23* (6), 1563-1570.

24. Razul, M. S. G.; Hendry, J. G.; Kusalik, P. G., Mechanisms of heterogeneous crystal growth in atomic systems: Insights from computer simulations. *Journal of Chemical Physics* **2005,** *123* (20), 204722.

25. Broughton, J. Q.; Gilmer, G. H.; Jackson, K. A., Crystallization Rates of a Lennard-Jones Liquid. *Physical Review Letters* **1982,** *49* (20), 1496-1500.

26. Kuksin, A. Y.; Norman, G. E.; Stegailov, V. V.; Yanilkin, A. V., Surface melting of superheated crystals. Atomistic simulation study. *Computer Physics Communications* **2007,** *177* (1–2), 34-37.

27. Zhang, S. L.; Zhang, X. Y.; Qi, L.; Wang, L. M.; Zhang, S. H.; Zhu, Y.; Liu, R. P., The study of melting stage of bulk silicon using molecular dynamics simulation. *Physica B* **2011,** *406* (13), 2637-2641.

28. Orekhov, N. D.; Stegailov, V. V., Molecular-dynamics based insights into the problem of graphite melting. *Journal of Physics: Conference Series* **2015,** *653* (1), 012090.

29. Orekhov, N. D.; Stegailov, V. V., Graphite melting: Atomistic kinetics bridges theory and experiment. *Carbon* **2015,** *87*, 358-364.

30. Zhou, N. G.; Hong, T.; Zhou, L., A comparative study between MEAM and Tersoff potentials on the characteristics of melting and solidification of carborundum. *Acta Phys. Sin.* **2012,** *61* (2), 028101.

31. Kirkpatrick, R. J., Crystal growth from the melt: A review. *American Mineralogist* **1975,** *60* (9-10), 798-614.

32. Herlach, D. M.; Palberg, T.; Klassen, I.; Klein, S.; Kobold, R., Overview: Experimental studies of crystal nucleation: Metals and colloids. *The Journal of Chemical Physics* **2016,** *145* (21), 211703.

33. Wilson, H. W., XX. On the velocity of solidification and viscosity of super-cooled liquids. *Philosophical Magazine Series 5* **1900,** *50* (303), 238-250.

34. Frenkel, J., Note on a relation between the speed of crystallization and viscosity. *Phys. Z. Sowjetunion* **1932,** *1*, 498.

35. Wu, K. A.; Wang, C. H.; Hoyt, J. J.; Karma, A., Ginzburg-Landau theory of the bcc-liquid interface kinetic coefficient. *Physical Review B* **2015,** *91* (1), 10.

36. Mendelev, M. I.; Rahman, M. J.; Hoyt, J. J.; Asta, M., Molecular-dynamics study of solid-liquid interface migration in fcc metals. *Modelling and Simulation in Materials Science and Engineering* **2010,** *18* (7), 074002.

37. Toda, A.; Androsch, R.; Schick, C., Insights into polymer crystallization and melting from fast scanning chip calorimetry. *Polymer* **2016,** *91*, 239-263.

38. Minakov, A. A.; Wurm, A.; Schick, C., Superheating in linear polymers studied by ultrafast nanocalorimetry. *The European Physical Journal E* **2007,** *23* (1), 43.

39. Toda, A.; Hikosaka, M.; Yamada, K., Superheating of the melting kinetics in polymer crystals: a possible nucleation mechanism. *Polymer* **2002,** *43* (5), 1667-1679.

40. Toda, A.; Kojima, I.; Hikosaka, M., Melting kinetics of polymer crystals with an entropic barrier. *Macromolecules* **2008,** *41* (1), 120-127.

41. Bhattacharya, D.; Cubeta, U.; Sadtchenko, V., Fast Scanning Calorimetry–Fast Thermal Desorption Technique: The Thin Wire Approach. In *Fast Scanning Calorimetry*, Schick, C.; Mathot, V., Eds. Springer International Publishing: 2016; pp 151-186.

42. Bhattacharya, D.; Sadtchenko, V., Enthalpy and high temperature relaxation kinetics of stable vapor-deposited glasses of toluene. *The Journal of Chemical Physics* **2014,** *141* (9), 094502.

43. Bhattacharya, D.; Sadtchenko, V., Vapor-deposited non-crystalline phase vs ordinary glasses and supercooled liquids: Subtle thermodynamic and kinetic differences. *Journal of Chemical Physics* **2015,** *142* (16), 164510.

44. Vyazovkin, S.; Chrissafis, K.; Di Lorenzo, M. L.; Koga, N.; Pijolat, M.; Roduit, B.; Sbirrazzuoli, N.; Sunol, J. J., ICTAC Kinetics Committee recommendations for collecting experimental thermal analysis data for kinetic computations. *Thermochim. Acta* **2014,** *590*, 1-23.

45. House, J. E., *Principles of Chemical Kinetics* 2ed.; Academic Press: Saint Louis, US, 2007.

46. Bilde, M.; Barsanti, K.; Booth, M.; Cappa, C. D.; Donahue, N. M.; Emanuelsson, E. U.; McFiggans, G.; Krieger, U. K.; Marcolli, C.; Tropping, D.; Ziemann, P.; Barley, M.; Clegg, S.; Dennis-Smither, B.; Hallquist, M.; Hallquist, A. M.; Khlystov, A.; Kulmala, M.; Mogensen, D.; Percival, C. J.; Pope, F.; Reid, J. P.; da Silva, M.; Rosenoern, T.; Salo, K.; Soonsin, V. P.; Yli-Juuti, T.; Prisle, N. L.; Pagels, J.; Rarey, J.; Zardini, A. A.; Riipinen, I., Saturation Vapor Pressures and Transition Enthalpies

of Low-Volatility Organic Molecules of Atmospheric Relevance: From Dicarboxylic Acids to Complex Mixtures. *Chem. Rev.* **2015,** *115* (10), 4115-4156.

47. Garai, J., Physical model for vaporization. *Fluid Phase Equilib.* **2009,** *283* (1-2), 89-92.
48. Sadtchenko, V.; Brindza, M.; Chonde, M.; Palmore, B.; Eom, R., The vaporization rate of ice at temperatures near its melting point. *Journal of Chemical Physics* **2004,** *121* (23), 11980-11992.
49. Cappa, C. D.; Lovejoy, E. R.; Ravishankara, A. R., Evaporation rates and vapor pressures of the even-nunibered C-8-C-18 monocarboxylic acids. *J. Phys. Chem. A* **2008,** *112* (17), 3959-3964.
50. Kolasinski, K. K., *Surface Science : Foundations of Catalysis and Nanoscience (3)*. Wiley: Somerset, GB, 2012.
51. Tartaglino, U.; Zykova-Timan, T.; Ercolessi, F.; Tosatti, E., Melting and nonmelting of solid surfaces and nanosystems. *Phys. Rep.-Rev. Sec. Phys. Lett.* **2005,** *411* (5), 291-321.
52. Dash, J. G., Melting from one to two to three dimensions. *Contemporary Physics* **2002,** *43* (6), 427-436.
53. Dash, J. G., Surface melting. *Contemporary Physics* **1989,** *30* (2), 89-100.
54. Lemmon, E. W.; McLinden, M. O.; Friend, D. G., Thermophysical Properties of Fluid Systems. In *NIST Chemistry WebBook, NIST Standard Reference Database Number 69*, Linstrom, P. J.; Mallard, W. G., Eds. National Institute of Standards and Technology: Gaithersburg, MD, 2005.
55. Chezeau, J. M.; Strange, J. H., Diffusion in molecular crystals. *Physics Reports* **1979,** *53* (1), 1-92.
56. Langer, J. S., Theories of glass formation and the glass transition. *Reports on Progress in Physics* **2014,** *77* (4), 042501.
57. Ramos, M. A.; Kabtoul, B.; Hassaine, M., Calorimetric and thermodynamic study of glass-forming monohydroxy alcohols. *Philosophical Magazine* **2011,** *91* (13-15), 1847-1856.
58. Gokhale, S.; Sood, A. K.; Ganapathy, R., Deconstructing the glass transition through critical experiments on colloids. *Advances in Physics* **2016,** *65* (4), 363-452.

Chapter Four: Surface-facilitated softening of ordinary and vapor-deposited glasses

Preface: This Chapter is a modified version of the manuscript published[1] in the Journal of Chemical Physics with co-authors Deepanjan Bhattacharya and Vladislav Sadtchenko. As discussed in Chapter 1, the recent discovery of highly stable vapor-deposited glass is now considered to be the most important development in the field[2-3]. It was revealed that these amorphous phases undergo softening by a surface facilitated mechanism[4], which is only typically observed in crystalline materials[5-7]. The unintentional consequence of these studies was the assumption that this surface-facilitated transformation is unique to "super-stable" VD glasses. In this Chapter, I challenge this belief by demonstrating for the first time, that, in the limit of high heating rates, softening of ordinary glasses also proceeds heterogeneously.

4.1. Overview

After decades of intense experimental and theoretical study, there remains a significant challenge to predict and understand the structure and physical properties of supercooled liquids and glasses[8-10]. The outstanding fundamental questions include the origins of liquid fragility, the correlation of physical properties with thermal history, and the mechanisms of glass hardening or softening (devitrification) under a variety of experimental conditions. The most common glass preparation technique is the slow cooling of a melt below its standard glass transition temperature, T_g. This traditional approach is not the only route to making solid non-crystalline phases. As demonstrated by Suga and coworkers more than four decades ago[11], vitreous phases can also be formed in vacuum by

physical vapor deposition onto cooled substrates. Furthermore, under certain conditions, this alternative technique may produce vitreous films with a surprisingly high density and kinetic stability[12].

The high stability of vapor-deposited (VD) glasses is manifested by their long structural relaxation times, τ, and consequently, high devitrification temperatures. The formation mechanism of these "super-stable" phases is assumed to result from rapid surface diffusion, which is several orders of magnitude faster[8, 13] than bulk self-diffusion at T_g. The surface constituents can consequently occupy local potential energy minima, which are inaccessible during traditional melt cooling[8]. Thus, stable VD phases are often considered to be ordinary glasses (OG) with exceedingly low fictive temperatures[14], T_f .

Although many experimental results support the notion that VD materials are fundamentally similar to ordinary glasses[15], one notable difference between the phases is the apparent glass softening mechanism[16]. While the devitrification of the OG phases is known to occur throughout the bulk, the devitrification of stable VD phases originates at the film's surface and progresses into its bulk via a transformation front[4, 16]. The kinetic rate law of such a surface-facilitated (SF) transformation is zero-order, i.e. the rate does not depend on the number of transformed constituents[17].

The SF softening of VD glasses is typically observed during alternating-current calorimetry experiments that utilize isothermal holds[18] at temperatures several K above T_g (e.g. Fig. 8 of Ref. [19]). In non-isothermal experiments, where the temperature of devitrification relates to the heating rate, SF softening can occur[20-21] at tens of K above the T_g. For instance, our quasi-adiabatic Fast Scanning Calorimetry (FSC) experiments with stable, VD, micrometer-scale MB films yielded convincing evidence for the SF softening

mechanism[20]. The leading-edge overlap in heat flow diagrams of films with distinct thicknesses strongly indicates that transformation rates are independent of sample size, i.e. kinetics are zero-order. Another group obtained similar results from FSC experiments, even in the case of ultrathin (20 - 200 nm) methylbenzene[22] and indomethacin[21] vapor-deposited films. In short, SF devitrification is now accepted as a general phenomenon, albeit unique to stable VD glasses.

The distinct devitrification mechanisms of OG and VD glasses can be rationalized by an interplay of bulk and near-surface structural relaxation times, τ_{bulk} and τ_{surf}. For non-equilibrium phases, τ_{bulk} is a monotonically *decreasing* function of fictive temperature and has a stronger, super-Arrhenius dependence on sample temperature compared to that of τ_{surf}.[8, 14] The VD glasses' low T_f results in long τ_{bulk}s , which drastically exceed τ_{surf} at the softening temperature. Thus, the bulk softening kinetics in VD glasses are effectively "jammed" and the only remaining softening pathway is relaxation from the surface[16].

Unlike stable VD glasses, OG phases must be characterized by a much higher T_f and, therefore, a much shorter τ_{bulk} . Consequently, there is a significantly smaller gap between τ_{bulk} and τ_{surf}. This blurring distinction between the relaxation times of OGs leads to competition between bulk and surface-facilitated softening mechanisms. Therefore, both isothermal and non-isothermal calorimetry experiments show complex, non-zero-order softening kinetics.

The distinct devitrification scenarios described in the preceding paragraphs seem to imply that the principle factor determining the softening mechanism (bulk vs. SF) may be the difference between the softening and fictive temperatures of the sample. This conjecture leads to the following conclusion: even ordinary glasses may undergo surface-

facilitated devitrification when their softening temperatures are increased significantly above their fictive temperatures. For example, under conditions of rapid heating the characteristic softening temperatures[20-21, 23-24] can rise tens of K above the standard T_g. Therefore, in FSC experiments, the softening of an ordinary glassy film may also originate on the free surface (vacuum-film interface) and progress into its bulk, just as in the case of VD glassy films. Thus, complex glass-softening kinetics can potentially reduce to the fastest pathway: surface-facilitated transformation, with an Arrhenius-like rate constant.

To test this hypothesis and gain further insights into the softening mechanisms of stable VD and ordinary glasses, we conducted a set of FSC experiments with micrometer-scale, OG films of methylbenzene (MB) and 2-propanol (2P) at their standard T_gs, 117 and 115 K, respectively[25-26]. We choose these particular glass formers because of their distinct molecular structure (aromatic vs. alcohol), intermolecular interactions (Van-der-Waals vs. hydrogen bonding), and dynamic properties (i.e. liquid fragility) [8, 14].

4.2. Experimental

All of the sample films were prepared in our thin-wire FSC apparatus, for which the design and operations is described in Chapter 2. Therefore, the experimental procedures for this Chapter are limited to the sample preparation protocol, which is straightforward. Preparation of ordinary glassy films began with vapor deposition onto the filament at T_g + 10 K. Deposition was followed by gradual cooling, and then a 10-minute, isothermal hold at T_g. Essentially, our ordinary glass samples are highly viscous liquids that are *fully equilibrated* at T_g. In other words, their fictive temperatures are *equal* to T_g. In addition to OG films, MB films of heightened kinetic stability were prepared by vapor-deposition at $0.95 \cdot T_g$ (112 K) with a rate of 15 $nm \cdot s^{-1}$.

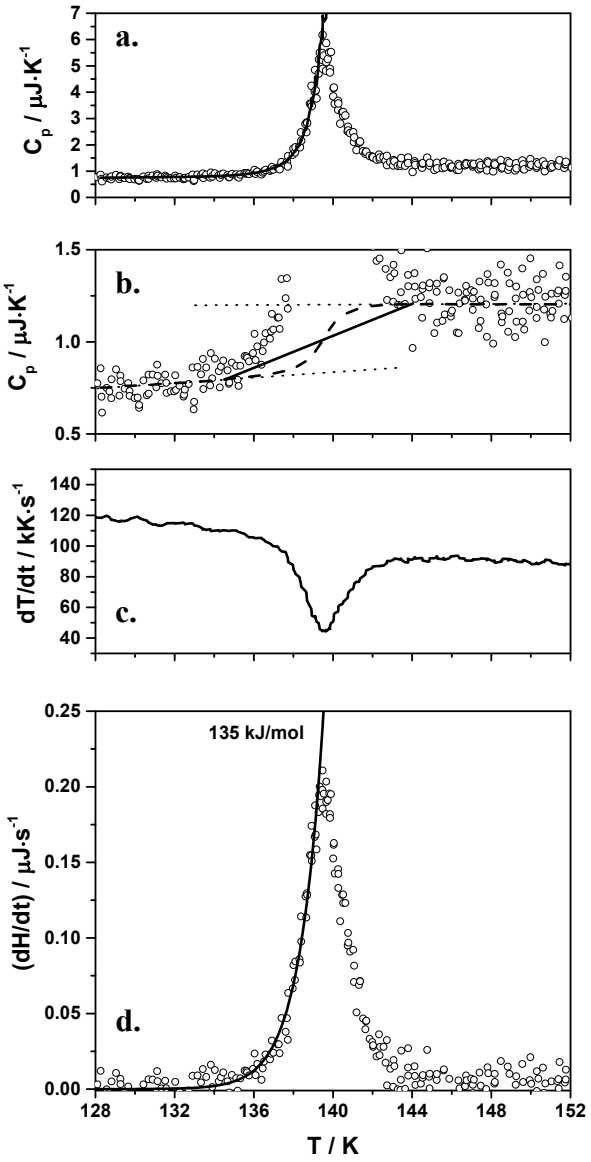

Fig. 4.1. The typical analysis of the FSC thermograms for glassy materials. Example data is for a 1.6 μm thick OG film of MB. The apparent heat capacity with softening endotherm **(a)** and the baseline estimates **(b)** of true C_p. This baseline is subtracted from the thermogram to infer $(dH/dT)_{ex}$. With the addition of heating rate **(c)** during transformation, we obtain the heat flow rate **(d)** plotted as the function of temperature. This value is assumed to be proportional to the softening rate.

4.3. Thermogram analysis and results

Fig. 4.1 illustrates the typical analysis used to infer the devitrification rates. The data are for a 1.6-μm-thick ordinary glassy film of methylbenzene. The analysis is identical to that employed in our recent studies on melting kinetics of superheated molecular crystals[27] (see Chapter 3). The dominant feature of the FSC thermogram in Fig. 4.1.a is a large fast-relaxation endotherm with an onset temperature of approximately 133 K. As heating continues, the apparent heat capacity reaches a maximum at 140 K and then decreases rapidly. At 144 K, the softening transition is complete and $C_{p,a}$ becomes nearly independent of temperature.

We begin our analysis with a standard assumption that, in the temperature range of transformation (140 ± 4 K), the overall $C_{p,a}$ must consist of two contributions. The first contribution is the true heat capacity of the softening sample, C_p. The second is the *excess* heat capacity, $(dH/dT)_{ex}$, which arises from increased heat flow into a sample that is undergoing an endothermic transformation. Note that the $(dH/dT)_{ex}$ values serve as the primary data[27] for inferring the softening rates in the films. As shown by the solid line in Fig. 4.1.b, our simplest approximation of the true C_p for the partially softened MB samples is a straight line connecting the sample's C_p in its initial and softened states. *Prior to and after* softening, the sample's C_p can be approximated by a linear function for the vitreous film and a constant for the liquid film (dotted lines in Fig. 4.1.b). Subtracting the results of this model from the FSC thermogram yields $(dH/dT)_{ex}$. Although we developed a more sophisticated approximation of the softening sample's true heat capacity (see dashed line in Fig. 4.1.b), its use proved to be unnecessary due to the high relative magnitude of the endotherm in respect to true C_p (see Fig. 4.1.a).

To obtain the *rate* of excess heat flow, $(dH/dt)_{ex}$, into the film during softening, we multiply $(dH/dT)_{ex}$ by the film's heating rate, dT/dt, which is shown in Fig. 4.1.c. According to the central assumption of thermal analysis[28], the absolute rate of transformation is proportional to the excess heat flow rate $(dH/dt)_{ex}$. As illustrated by the solid line in Fig. 4.1.d, a simple Arrhenius temperature dependence of the heat flow,

$$\left(\frac{dH}{dt}\right)_{ex}(T) = \left(\frac{dH}{dt}\right)_0 \times e^{-\frac{E_S}{RT}}, \quad (4.1)$$

provides the best fit of the data. In Eq. 4.1, $(dH/dt)_0$ is a constant and E_s is the apparent activation energy barrier for softening. Again, the example in Fig. 4.1 is typical *for all* OG films which we interrogated with heating rates on the order of 10^5 K·s^{-1}. For *all* investigated samples, an Arrhenius approximation is the best fit for the temperature-dependent rate of heat flow. In summary, the kinetics of softening for glassy films under conditions of rapid heating are much simpler than those typically observed in traditional DSC studies[14].

4.4. Discussion

Fig. 4.2 compares the kinetics of softening for VD and OG methylbenzene films. It reinforces the conclusion of the preceding paragraph. From previous analysis[20], these VD samples have a specific enthalpy that is approximately 150 J·mol^{-1} lower than the enthalpy of equilibrium liquid at T_g. The lower enthalpy translates into a significantly higher kinetic stability manifested by higher softening temperature of VD films. As shown in Fig. 4.2.a, the devitrification onset temperature for VD samples is approximately 10 K higher than for OG films. Fig. 4.2.b and Fig. 4.2.c show that the leading edges of $(dH/dt)_{ex}$ diagrams overlap almost perfectly (within 0.2 K) for both OG and VD films of distinct thicknesses. Therefore, the *softening mechanism* of OG samples is *essentially identical* to that of VD

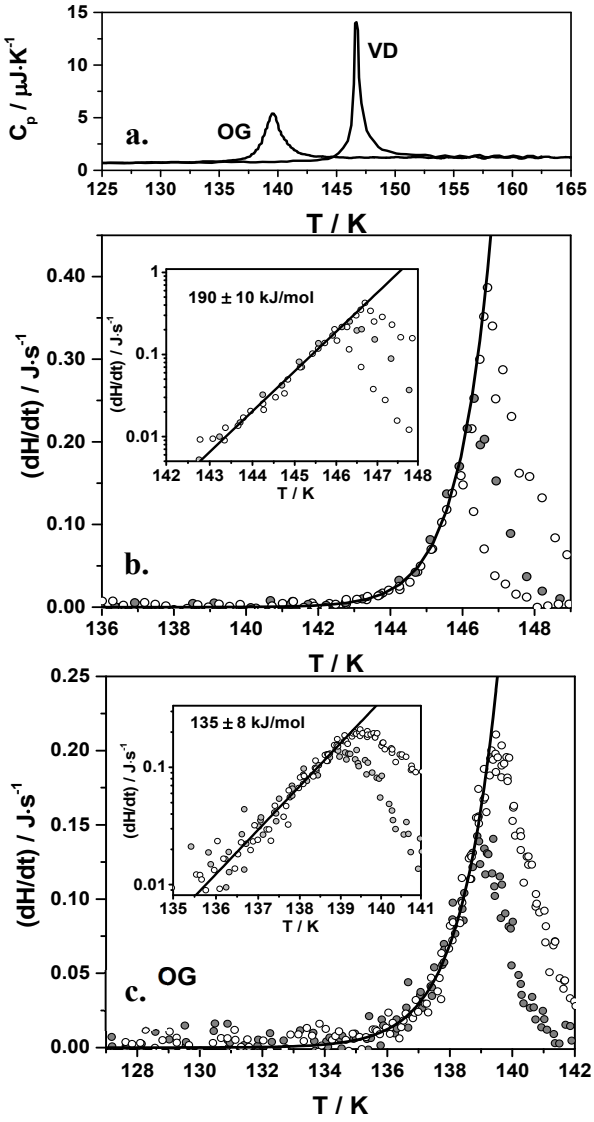

Fig. 4.2. Comparison of devitrification kinetics in stable and ordinary glassy films of MB. Softening endotherms **(a)** for stable and ordinary films. Softening rates of vapor-deposited **(b)** and ordinary glass **(c)** films of MB with thickness ranging from 0.8 to 1.8 μm. The overlap in the rate diagrams' leading edges for samples of distinct size strongly implies softening via a propagating front. Inset figures show the same data in Arrhenius coordinates (rate logarithm vs. inverse temperature). The apparent barriers to transformation are the values above the solid lines, which are the Arrhenius fits of the rate data.

films during rapid heating. Although pseudo-zero-order kinetics can approximate complex transformation rates at the start of many processes[29], we observe zero-order kinetics for *a significant* fraction (~50%) of both VD and OG samples. Thus, the *only* explanation for the observed kinetics in a single-constituent, non-reactive, uncatalyzed process such as softening, melting, or vaporization of condensed phases is a *zero-order, surface-facilitated* transformation.

In the ideal case, the softening rate would increase rapidly with temperature until the *entire* sample has transformed. Yet, as illustrated for both VD and OG films in Fig. 4.2.b and Fig. 4.2.c, our $(dH/dt)_{ex}$ rate diagrams show deviation from an Arrhenius dependence *after* the transformation of approximately 50-80% of the film. Presently, we do not have a comprehensive explanation for the tails and other non-Arrhenius features observed during transformation. Our preliminary conjecture is that the organic films may fracture or physically decouple from the tungsten substrate due to the thermal stresses of heating materials with mismatched expansion coefficients. This type of film fracturing has already been observed, albeit during rapid cooling[30]. Nevertheless, the fact remains that, for a significant fraction of our OG sample, softening kinetics *are* zero-order *and* Arrhenius. As such, we will continue our discussion of the generality and physical origins of the observed kinetics.

Up to this point, we focused primarily on the results of our FSC experiments with OG and VD films of methylbenzene. Although MB is an archetypical glass-former, it has a high[31] melt fragility (*m_A is 107*). Therefore, it is not immediately clear if strong glass formers will display SF softening under conditions of rapid heating. To alleviate the concerns that SF softening is a phenomenon unique to fragile glass formers[32], we

investigated softening kinetics in OG films of the relatively strong[33] 2-propanol (*m_A is 55*).

Fig. 4.3 compares the softening rates for OG films of both MB and 2P that are *fully-equilibrated* at their respective T_gs. As shown in Fig. 4.3, for 2P films of distinct thicknesses, the leading edges of rate diagrams overlap. More significantly, devitrification occurs with a rate that is well approximated by an Arrhenius temperature dependence (see black line in Fig. 4.3). This unambiguously shows that SF softening is not limited to condensed amorphous phases of only fragile glass-formers. In other words, surface-facilitated transformation is likely to be a general phenomenon for condensed phases under conditions of rapid heating[27].

Despite the qualitative similarities in their softening mechanism, the actual softening rates of the two compounds differ quantitatively. In addition to a lower characteristic onset temperature for softening, the fragile MB samples have a higher effective average activation energy than the strong 2P samples. As illustrated in Fig. 4.3, the Arrhenius E_s to OG softening for MB films appears to be 1.7 times greater than that of 2P samples (135 vs. 80 kJ·mol^{-1}). Furthermore, it seems that the physical properties of the sample *prior to* rapid heating control the softening rate. Indeed, the E_s values are near the activation energy of α-relaxation for each compound at temperatures close to their respective T_gs (see Fig. 3.5)[27]. Though a comprehensive explanation of the observed transformation kinetics is outside the scope of this preliminary study, the variations in E_s demonstrate that relaxation kinetics *are* reflective of fundamental properties of glass-formers and the stability of the amorphous phase. The fact that E_s values of stable VD samples are much larger than the values of OG films (190 vs. 135 kJ·mol^{-1} for MB films in Fig. 4.2) is also consistent with this conclusion.

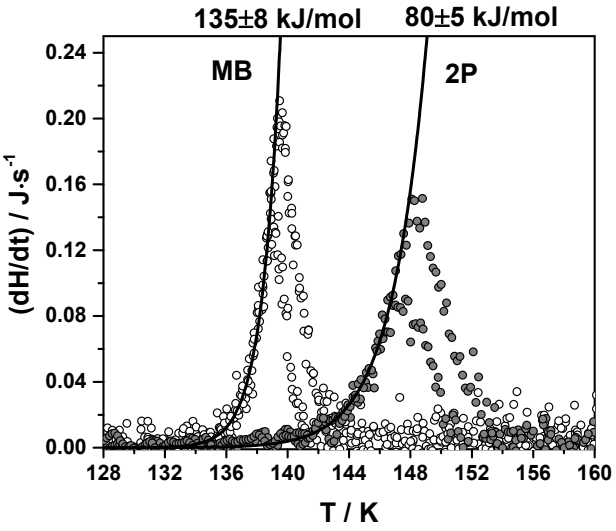

Fig. 4.3. Comparison of the surface-facilitated devitrification rates in ordinary glassy films of MB and 2P, with thicknesses ranging from 0.8 to 1.6 μm. Despite similar standard T_gs and thermodynamic parameters, the apparent E_s of MB films is 1.7 times greater than that of 2P films. For a summary of thermodynamic and kinetic data, see Table 3.1 in Chapter 3.

Although we implicitly assume that the devitrification of our glassy films originates at the film-vacuum interface, we cannot rule out a possibility that it may also occur at the filament-film boundary. We must emphasize, however, that the exact origins of the transformation front are *not vital* to our essential findings and conclusions. In our FSC experiments, the majority of kinetic data (e.g. E_s) is collected after the softening front has already progressed hundreds of molecular layers away from the facilitating interface[27]. Therefore, the location and physical properties of that interface are irrelevant to kinetics of glass softening at this later stage. Furthermore, in the unlikely case of two simultaneous softening fronts propagating from distinct interfaces, the apparent activation energy values must be identical to produce a linear dependence of the rate logarithm on inverse temperature.

4.5. Summary and afterword

We demonstrate that, not only vapor-deposited, but also ordinary glasses can soften by a surface- or interface- facilitated mechanism. When the heating rate is sufficiently high, complex devitrification kinetics of ordinary glasses reduce to a single, simple pathway with an Arrhenius temperature dependence. In addition to providing information on the kinetic behavior of vapor-deposited and ordinary glassy materials under thermal stress, our preliminary results also open a new venue for studying non-crystalline materials by fast scanning calorimetry. Because the interface-facilitated softening kinetics depend, at least partially, on the initial state of the non-crystalline sample prior to heating, we believe that this kinetic regime can become a novel experimental probe with a straightforward interpretation. In the proceeding Chapters of this Dissertation, I present the results of FSC experiments which validate this claim.

4.6. References for Chapter Four

1. Cubeta, U.; Bhattacharya, D.; Sadtchenko, V., Communication: Surface-facilitated softening of ordinary and vapor-deposited glasses. *Journal of Chemical Physics* **2017,** *147* (7), 071101.
2. Dawson, K. J.; Kearns, K. L.; Yu, L.; Steffen, W.; Ediger, M. D., Physical vapor deposition as a route to hidden amorphous states. *Proc. Natl. Acad. Sci. U. S. A.* **2009,** *106* (36), 15165-15170.
3. Chen, Z.; Richert, R., Dynamics of glass-forming liquids. XV. Dynamical features of molecular liquids that form ultra-stable glasses by vapor deposition. *Journal of Chemical Physics* **2011,** *135* (12), 124515.
4. Dalal, S. S.; Ediger, M. D., Influence of substrate temperature on the transformation front velocities that determine thermal stability of vapor-deposited glasses. *J Phys Chem B* **2015,** *119* (9), 3875-82.
5. Hart, E. W., Two-dimensional phase transformation in grain boundaries. *Scripta Metallurgica* **1968,** *2* (3), 179-182.
6. Kirkpatrick, R. J., Crystal growth from the melt: A review. *American Mineralogist* **1975,** *60* (9-10), 798-614.
7. Duvall, G. E.; Graham, R. A., Phase transitions under shock-wave loading. *Rev. Mod. Phys.* **1977,** *49* (3), 523-579.
8. Daley, C. R.; Fakhraai, Z.; Ediger, M. D.; Forrest, J. A., Comparing surface and bulk flow of a molecular glass former. *Soft Matter* **2012,** *8* (7), 2206-2212.
9. Gokhale, S.; Sood, A. K.; Ganapathy, R., Deconstructing the glass transition through critical experiments on colloids. *Advances in Physics* **2016,** *65* (4), 363-452.
10. Tropin, T. V.; Schmelzer, J. W. P.; Aksenov, V. L., Modern aspects of the kinetic theory of glass transition. *Phys. Usp.* **2016,** *59* (1), 42-66.
11. Haida, O.; Suga, H.; Seki, S., Realization of the glassy state of some simple liquds by the vapor condensation method. *Thermochim. Acta* **1972,** *3* (3), 177-180.
12. Swallen, S. F.; Kearns, K. L.; Mapes, M. K.; Kim, Y. S.; McMahon, R. J.; Ediger, M. D.; Wu, T.; Yu, L.; Satija, S., Organic Glasses with Exceptional Thermodynamic and Kinetic Stability. *Science* **2007,** *315* (5810), 353-356.
13. Zhu, L.; Brian, C. W.; Swallen, S. F.; Straus, P. T.; Ediger, M. D.; Yu, L., Surface Self-Diffusion of an Organic Glass. *Physical Review Letters* **2011,** *106* (25), 256103.
14. Hodge, I. M., Enthalpy relaxation and recovery in amorphous materials. *Journal of Non-Crystalline Solids* **1994,** *169* (3), 211-266.

15. Chua, Y. Z.; Ahrenberg, M.; Tylinski, M.; Ediger, M. D.; Schick, C., How much time is needed to form a kinetically stable glass? AC calorimetric study of vapor-deposited glasses of ethylcyclohexane. *Journal of Chemical Physics* **2015,** *142* (5), 11.

16. Dalal, S. S.; Ediger, M. D., Influence of Substrate Temperature on the Transformation Front Velocities That Determine Thermal Stability of Vapor-Deposited Glasses. *J. Phys. Chem. B* **2015,** *119* (9), 3875-3882.

17. House, J. E., *Principles of Chemical Kinetics* 2ed.; Academic Press: Saint Louis, US, 2007.

18. Kearns, K. L.; Ediger, M. D.; Huth, H.; Schick, C., One Micrometer Length Scale Controls Kinetic Stability of Low-Energy Glasses. *Journal of Physical Chemistry Letters* **2010,** *1* (1), 388-392.

19. Ahrenberg, M.; Chua, Y. Z.; Whitaker, K. R.; Huth, H.; Ediger, M. D.; Schick, C., In situ investigation of vapor-deposited glasses of toluene and ethylbenzene via alternating current chip-nanocalorimetry. *Journal of Chemical Physics* **2013,** *138* (2), 11.

20. Bhattacharya, D.; Sadtchenko, V., Enthalpy and high temperature relaxation kinetics of stable vapor-deposited glasses of toluene. *The Journal of Chemical Physics* **2014,** *141* (9), 094502.

21. Rodríguez-Tinoco, C.; Gonzalez-Silveira, M.; Ràfols-Ribé, J.; Lopeandía, A. F.; Clavaguera-Mora, M. T.; Rodríguez-Viejo, J., Evaluation of Growth Front Velocity in Ultrastable Glasses of Indomethacin over a Wide Temperature Interval. *The Journal of Physical Chemistry B* **2014,** *118* (36), 10795-10801.

22. Rafols-Ribe, J.; Gonzalez-Silveira, M.; Rodriguez-Tinoco, C.; Rodriguez-Viejo, J., The role of thermodynamic stability in the characteristics of the devitrification front of vapour-deposited glasses of toluene. *Physical Chemistry Chemical Physics* **2017,** *19* (18), 11089-11097.

23. Bhattacharya, D.; Sadtchenko, V., Vapor-deposited non-crystalline phase vs ordinary glasses and supercooled liquids: Subtle thermodynamic and kinetic differences. *Journal of Chemical Physics* **2015,** *142* (16), 164510.

24. Leon-Gutierrez, E.; Sepulveda, A.; Garcia, G.; Clavaguera-Mora, M. T.; Rodriguez-Viejo, J., Stability of thin film glasses of toluene and ethylbenzene formed by vapor deposition: an in situ nanocalorimetric study. *Physical Chemistry Chemical Physics* **2010,** *12* (44), 14693-14698.

25. Talón, C.; Ramos, M. A.; Vieira, S.; Shmyt'ko, I.; Afonikova, N.; Criado, A.; Madariaga, G.; Bermejo, F. J., Thermodynamic and structural properties of the two isomers of solid propanol. *Journal of Non-Crystalline Solids* **2001,** *287* (1–3), 226-230.

26. Yamamuro, O.; Tsukushi, I.; Lindqvist, A.; Takahara, S.; Ishikawa, M.; Matsuo, T., Calorimetric study of glassy and liquid toluene and ethylbenzene: Thermodynamic approach to spatial heterogeneity in glass-forming molecular liquids. *J. Phys. Chem. B* **1998,** *102* (9), 1605-1609.

27. Cubeta, U.; Bhattacharya, D.; Sadtchenko, V., Melting of superheated molecular crystals. *The Journal of Chemical Physics* **2017,** *147* (1), 014505.

28. Vyazovkin, S.; Chrissafis, K.; Di Lorenzo, M. L.; Koga, N.; Pijolat, M.; Roduit, B.; Sbirrazzuoli, N.; Sunol, J. J., ICTAC Kinetics Committee recommendations for collecting experimental thermal analysis data for kinetic computations. *Thermochim. Acta* **2014,** *590*, 1-23.

29. Pogliani, L., Pseudo-zero-order reactions. *Reaction Kinetics and Catalysis Letters* **2008,** *93* (2), 187-191.

30. Chen, Y.; Powell, C. T.; Yu, L., Tensile Fracture of Molecular Glasses Studied by Differential Scanning Calorimetry: Reduction of Heat Capacity by Lateral Constraint. *The Journal of Physical Chemistry B* **2017,** *121* (2), 444-449.

31. Hinze, G.; Sillescu, H., H-2 nuclear magnetic resonance study of supercooled toluene: Slow and fast processes above and below the glass transition. *Journal of Chemical Physics* **1996,** *104* (1), 314-319.

32. Sepulveda, A.; Tylinski, M.; Guiseppi-Elie, A.; Richert, R.; Ediger, M. D., Role of fragility in the formation of highly stable organic glasses. *Phys Rev Lett* **2014,** *113* (4), 045901.

33. Ramos, M. A.; Kabtoul, B.; Hassaine, M., Calorimetric and thermodynamic study of glass-forming monohydroxy alcohols. *Philosophical Magazine* **2011,** *91* (13-15), 1847-1856.

Chapter Five: Relaxation mechanism of rapidly heated non-crystalline phases

Preface: This Chapter is a modified version of a manuscript submitted to a peer-reviewed journal with co-author Vladislav Sadtchenko.

5.1. Overview

As discussed in Chapter 4 of this Dissertation, the surface- or interface-facilitated softening mechanism of ordinary glasses can open a new venue for studying non-crystalline materials by the FSC technique. Indeed, the distinctions between the apparent activation energy barriers for softening front propagation in strong and fragile glassy films imply a strong dependence of the softening kinetics on the initial structural state of the sample[1]. Further FSC studies are, however, necessary to fully validate this preliminary conclusion and to establish direct *quantitative* relationships between the initial state of a non-crystalline material and its high temperature softening kinetics.

A meaningful exploration of the correlations between the kinetic parameters of the zero-order softening process and the sample's initial structure, thermodynamics, or dynamic state (see Section 1.6) requires a *set* of non-crystalline samples with distinct but well-defined initial states. Ordinary or vapor-deposited molecular glasses at temperatures below the compound's T_g are *not* appropriate for such a study because a glass's initial state is *not easily defined* nor characterized (see Section 1.3). Although the initial state of a non-equilibrium glass can be, to some extent, characterized by its fictive temperature, an accurate determination of the sample's T_f and its meaning are still a matter of debate[2].

In contrast to a glass, the structural and thermodynamic state of a meta-equilibrium, supercooled molecular *liquid* is well-defined (see Fig. 1.1). As such, amorphous materials that are *fully equilibrated* at distinct temperatures above and slightly below the compound's T_g have well-defined initial states. During rapid heating of such a sample, the fictive temperature is simply the initial temperature of the material, i.e. T_f is equal to T_i. Furthermore, the initial thermodynamic variables (enthalpy, entropy, or specific volume) and the kinetics of the initial state (relaxation time or self-diffusivity) are typically well known (see Section 1.9). For example, the wealth of available data[3-19] on the heat capacity, density, and molecular kinetics in supercooled *liquid* methyl benzene (MB) makes this material an excellent choice for a study that evaluates the correlation between the initial state of a non-crystalline material and the kinetics of its high temperature relaxation during rapid heating.

Fig. 5.1 illustrates the basic concept of the FSC study described in this Dissertation Chapter. We prepared a set of *fully-equilibrated*, micrometer-thick films of supercooled liquid MB (T_g is 117 K) at initial temperatures ranging from T_g *-1* K to T_g *+7* K. These ordinary liquid films were subjected to rapid heating from Ti through the temperature of fast relaxation, T_R, and beyond. In agreement with past FSC studies[20], the shape and position (T_R) of the fast relaxation endotherms shown in Fig. 5.1.a are very sensitive to each sample's initial temperature, T_i or T_f. As we increase T_i, the endotherms broaden and the temperature at which relaxation takes place decreases. The proceeding Sections of this Chapter describe a novel FSC thermogram analysis method and propose a quantitative model for the mechanism of fast relaxation in rapidly heated non-crystalline phases.

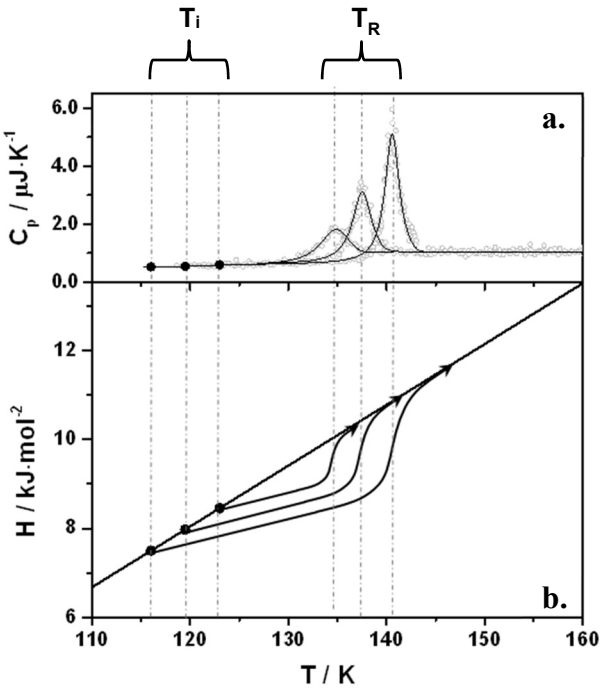

Fig. 5.1. An outline of the FSC experiments described in Chapter 5. *Fully-equilibrated liquid* films of methyl benzene (MB) can be prepared at temperatures above and slightly below T_g (117 K). These micrometer-scale MB samples have *well-defined initial states*. **(a)** During rapid heating, the FSC thermograms of these samples exhibit high temperature **(T_R)** relaxation endotherms that are *extremely sensitive* to each sample's initial temperature **(T_i)**. As shown in the top panel **(a)**, an increase in T_i leads to a decrease in the onset temperature of relaxation and a broadening of the relaxation endotherm. **(b)** The relative enthalpy of each sample, i.e. integrated thermogram **(curved lines)**, can be matched to MB's literature values **(straight line)**. Thus, we know the initial state of each sample. Consequently, a kinetic analysis of the FSC endotherms for this data set makes is possible to validate our hypothesis for the proposed relaxation mechanism.

5.2. Experimental technique

All experiments in this Dissertation Chapter utilized the custom-built, adiabatic, fast scanning calorimetry (FSC) apparatus that is described extensively in Chapter 2. The data acquisition system, vapor deposition source, and temperature calibrations were identical to those used in experiments described in the preceding Chapters. Therefore, I proceed with describing the sample preparation protocol utilized to prepare the fully-equilibrated, ordinary supercooled liquid films that were needed for the study described in this Dissertation Chapter.

5.3. Sample preparation protocols

Micrometer-scale films of methyl benzene (MB) were prepared by vapor deposition with rates of approximately 15 $nm \cdot s^{-1}$ and with substrate temperatures ranging from 116 K to 124 K. Although vapor-deposition at low temperatures may result in the formation of unique non-crystalline phases (see Section 1.8), such phases are not the focus of this Dissertation Chapter. Therefore, vapor deposition was followed by an annealing and cooling protocol that ensured the formation of *fully-equilibrated ordinary supercooled liquids*. Although, as described in Chapter 4, ordinary liquid or glassy samples can be prepared by slow cooling ($1K \cdot min^{-1}$) from $T_g + 10$ K to a temperature near T_g, this preparation technique is very time intensive. Therefore, a less time-consuming protocol was developed to produce sample films of fully-equilibrated, ordinary liquids near or above T_g. It is illustrated in Fig. 5.2 and explained immediately below.

The diagram in Fig. 5.2 illustrates of the sample preparation protocol used to obtain fully equilibrated supercooled liquid films of MB. In the first step, vapor is deposited onto

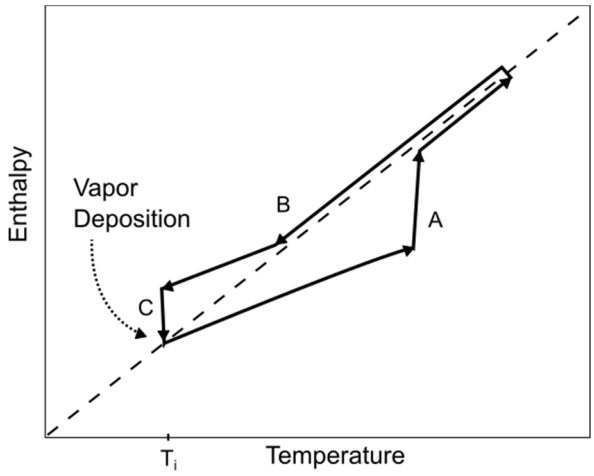

Fig. 5.2. An illustration of the sample preparation protocol used for the experiments described in this dissertation Chapter. The **solid lines** reflect the sample's enthalpy at each step of the protocol. The arrows illustrate the direction of the change for each step. The extrapolated enthalpy of the supercooled liquid is drawn for comparison **(dashed line)**. During sample preparation, vapor deposition at T_i **(dotted line)** is followed by a heating pulse to soften the film **(A)**. The sample is then passively cooled back down to T_i **(B)**, which produces a glassy phase with a fictive temperature above T_i. Thereafter, the sample is annealed **(C)** at T_i for a duration that is sufficient to fully equilibrate the sample. Thus, at the conclusion of the sample preparation protocol, we produce a fully equilibrated liquid that has a fictive temperature equal to T_i.

the filament at a low temperature, T_i, which may produce a glass of heightened kinetic stability[21]. In order to avoid this outcome, the sample film is softened with a short and fast heating pulse that increases the sample's temperature to approximately 25 K above T_g (step A). The warm liquid film is then cooled back down to T_i with a rate in excess of 50 $K \cdot s^{-1}$ (step B), producing a high enthalpy glassy phase which may have a relatively high fictive temperature. Thereafter (step C), the films are annealed at T_i for a time interval that is an order of magnitude higher than the dielectric relaxation time (τ_α). In short, this sample preparation protocol produces *fully equilibrated* ordinary supercooled liquid films, i.e. the T_f of each sample is equal to T_i. We routinely verified this conclusion by increasing and decreasing the annealing time at each T_i.

The thickness of each MB film was determined from its FSC thermogram. Because the MB thermograms are free of endotherms and exotherms in the temperature range of 160 to 200 K, the heat capacity values in this range can be used to calculate the sample mass and thickness. Thus, dividing the measured C_p by the specific heat capacity of liquid MB yields the mass of each film[22]. The thickness of each film is then calculated with an accuracy of approximately ±25 nm using estimates of MB's liquid density in this temperature range[23]. This routine thickness determination was validated by an alternative estimate that relied on measuring the sample's overall enthalpy of vaporization [24].

5.4. Analysis of FSC thermograms

A novel method of FSC thermogram analysis, illustrated in Fig. 5.3, was used to obtain the kinetic parameters of fast relaxation for these fully-equilibrated liquid samples. First, the apparent heat capacity, $C_{p,a(T)}$, of the rapidly heated MB films was measured as

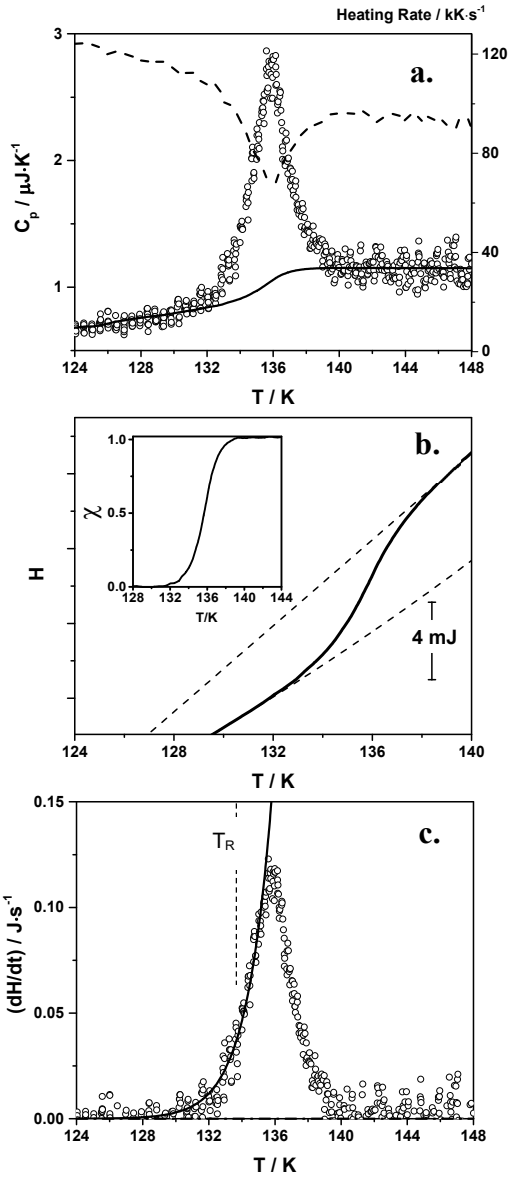

Fig. 5.3. An example of the kinetic analysis used for the FSC thermograms of ordinary liquid films. The sample is a 1.45-µm-thick film of MB fully equilibrated at 118.5 K. **(a)** The apparent heat capacity, $C_{p,a}$, **(circles)** and the heating rate **(dashed line)** of the sample films are measured by the FSC apparatus's data acquisition system, as described in Chapter 2.5. The true heat capacity **(solid line)** of the sample during the FSC scan can be inferred from sample's enthalpy variations (see Eq. 5.2). **(b)** The enthalpy variations **(solid line)** of the sample during the FSC scan is obtained by integrating its $C_{p,a}$. The sample's enthalpy prior to and after transformation can be fit and extrapolated to estimate the enthalpy of the sample in its fully unrelaxed and fully relaxed states **(dashed lines)** over the temperature range of transformation. The **inset in (b)** shows the fraction of the sample that is fully relaxed during the FSC scan, as derived from Eq. 5.1. **(c)** The excess heat flow, $(dH/dt)_{ex}$, during the FSC scan **(circles)** and the Arrhenius fit **(solid line)** of that data (see Eq. 5.3). The heat flow is assumed to be proportional to the absolute transformation rate.

described in Section 2.5 of this Dissertation. The data shown in Fig. 5.3 is for a representative, 1.45-μm-thick film of MB that was prepared by the protocol illustrated in Fig. 5.2. The MB film was vapor deposited onto the FSC filament at 118.5 K, rapidly heated to 145 K (step A), quickly cooled to 118.5 K (step B), and then annealed at this temperature for 180 s (step C). As I describe in Section 5.3, this preparation protocol yields an ordinary liquid sample which is fully equilibrated at T_i (118.5 K).

As shown in Fig. 5.3.a, the apparent heat capacity changes linearly with temperature at the start of rapid heating, as it would for a glassy sample[25-26]. In other words, rapid heating takes the sample phase far out of equilibrium, as illustrated in Fig. 5.1.b. The initial linear increase of $C_{p,a}$ in Fig. 5.3.a is followed by the FSC thermogram's fast relaxation endotherm (FRE) with the onset temperature of 132 K. As the sample relaxes from its glass-like state to the warmed equilibrium liquid state, the apparent heat capacity reaches a maximum at 136 K. As heating continues, $C_{p,a}$ decreases rapidly and the relaxation transformation is complete near 140 K, where $C_{p,a}$ becomes nearly independent of temperature. The rapidly heated liquid film remains in quasi-equilibrium until it vaporizes at temperatures above 200 K (not shown, see Chapter 3). As illustrated by the dashed line in Fig. 5.3.a, the heating rate ranges from 120,000 to 70,000 $K \cdot s^{-1}$ during the film's rapid transformation.

We begin our kinetic analysis by integrating the $C_{p,a}(T)$ shown in the Fig. 5.3.a. The resulting relative enthalpy is shown as the solid line in Fig. 5.3.b and serves as the basis for calculating the dimensionless extent of transformation, $\chi(T)$, during rapid relaxation[27]. Although both the initial and final states of the sample are equilibrium liquids (at T_i or above T_R), for the sake of simplicity, we will refer to the unrelaxed sample state as "solid"

and the fully relaxed sample state as "liquid." As illustrated by the dashed lines in Fig. 5.3.b, the enthalpies of the film are well-approximated by a second-degree polynomial for the "solid" prior to transformation and a linear function for the "liquid" after transformation. These fits are then extrapolated over the entire temperature range of relaxation. Because the sample's enthalpy can be viewed as a linear combination of the enthalpies of its components[28], we can calculate extent of conversion (i.e. transformation) using the following equation:

$$\chi(T) = \frac{H(T) - H_s(T)}{H_l(T) - H_s(T)}, \quad (5.1)$$

where $H_s(T)$ and $H_l(T)$ are the polynomial and linear fits of the "solid" and "liquid" enthalpies. The $\chi(T)$ values for the example film are shown as an inset in Fig. 5.3.b.

We continue the kinetic analysis by utilizing the fact that, in the temperature range of relaxation (136 ± 4 K), the overall *apparent* heat capacity, $C_{p,a}$, must consist of two contributions. The first contribution is the *true* heat capacity, C_p, of the sample during transformation. The second contribution is the *excess* heat, $(dH/dT)_{ex}$, which arises from the increased heat flow into a sample undergoing endothermic relaxation. The $(dH/dT)_{ex}$ value is, essentially, the difference between $C_{p,a}(T)$ and $C_p(T)$.

We can estimate the sample's *true* heat capacity, $C_p(T)$, during transformation as linear combination of the distinct heat capacities of its components[29]:

$$C_p = C_{p,s} \cdot (1 - \chi) + C_{p,l} \cdot \chi, \quad (5.2)$$

In Eq. 5.2, the $C_{p,s}(T)$ and $C_{p,l}(T)$ values are, respectively, the heat capacities of the sample in the "solid" and "liquid" states. As shown in Fig. 5.3.a, prior to relaxation, $C_{p,s}(T)$ has a linear dependence on temperature. In contrast, after the transformation, $C_{p,l}(T)$ is nearly constant with temperature. Similar to the treatment of the enthalpies in the preceding

paragraphs, we can extrapolate the heat capacities for the sample's fully "solid" and fully "liquid" states over the entire temperature range of transformation. Thus, using our estimates of the sample's relaxed fraction, $\chi(T)$, with Eq. 5.2, we infer the sample's true heat capacity, as shown by the solid line in Fig. 5.3.a. Finally, subtracting these values from the thermogram's apparent heat capacity yields the excess heat, $(dH/dT)_{ex}$.

In the last step of our kinetic analysis, we multiply $(dH/dT)_{ex}$ by the heating rate, dT/dt, to obtain the heat flow *rate*, $(dH/dt)_{ex}$, shown in Fig 5.3.c. In agreement with the results discussed in Chapter 4, an Arrhenius temperature dependence,

$$\left(\frac{dH}{dt}\right)_{ex}(T) = \left(\frac{dH}{dt}\right)_0 \times e^{-\frac{E_{a,R}}{RT}}, \quad (5.3)$$

provides the best fit for our rate data, as illustrated by the solid line in Fig. 5.3.c. In Eq. 5.3, $(dH/dt)_0$ is a temperature-independent constant and $E_{a,R}$ is the apparent activation energy barrier for relaxation.

Before proceeding with a discussion of these results, we note that it was only necessary to use the sophisticated analytical steps described in the preceding paragraphs for FSC thermograms of relatively warm liquid films, which are characterized by relatively small endotherms. In fact, when the T_i of a sample was below T_g + 4 K, we could use a simpler, linear approximation for the variations in the true C_p across the temperature range of transformation (see Chapter 3 and Chapter 4). For low T_f samples, the rate data obtained using this simpler approximation were nearly identical to the data reported here.

5.5. Determining the Arrhenius parameters of rapid relaxation

Fig. 5.4 shows representative kinetic data for non-equilibrium relaxation of three ordinary liquid MB films which have well-defined initial states. Each sample was prepared

following the protocol described in Section 5.3, with a thickness of approximately 1.5 μm. The initial temperatures, T_i, of the example liquid MB films in Fig. 5.4 are 117, 119, and 121K, as shown in the top label. Because the sample films were *fully equilibrated prior to scanning*, the initial temperatures of the samples during rapid, non-equilibrium heating are also the fictive temperatures (see Section 5.3). As expected from previous studies [1, 20], the $(dH/dt)_{ex}$ rate diagrams in Fig. 5.4.a. show that relaxation begins at lower temperatures for less stable films (higher T_f). Furthermore, at any given temperature prior to the completion of transformation, the *rate is lower for more stable samples* (lower T_f).

As I have described already (see Section 5.4), the excess heat flow rate values are proportional to the transformation rate of each sample. Yet, the $(dH/dt)_{ex}$ values shown in Fig. 5.4.a. are also a convolution[27] of both the *absolute* transformation rate, *dN/dt*, and the average enthalpy change during transformation[30-32], ΔH_{ex}. Nevertheless, these two effects can easily be decoupled. Fig. 5.4.b demonstrates that the ΔH_{ex} values for samples prepared under distinct conditions can be calculated with a temperature-integral of the excess heat capacity, $(dH/dT)_{ex}$. Alternatively, ΔH_{ex} can be estimated from the relative enthalpy diagrams (see Fig. 5.3.b). Simply dividing $(dH/dt)_{ex}$ by ΔH_{ex} yields overall absolute rate of relaxation, *dN/dt*. However, we scale the *dN/dt* values by the surface area of the transformation front, because it proved to be more informative to express the rate as a *flux* of constituents across the front. Thus, we calculate the transformation rate, *Z(T)*, using the following equation:

$$Z = \left(\frac{dH}{dt}\right)_{ex} \times \frac{1}{\Delta H_{ex}} \times \frac{1}{A_f}, \quad (5.4)$$

where A_f is approximately equal to the film's surface area, e.g. $6.4 \cdot 10^{-3}$ cm^2, and does not change significantly while surface-facilitated[30], zero-order rate kinetics are observed.

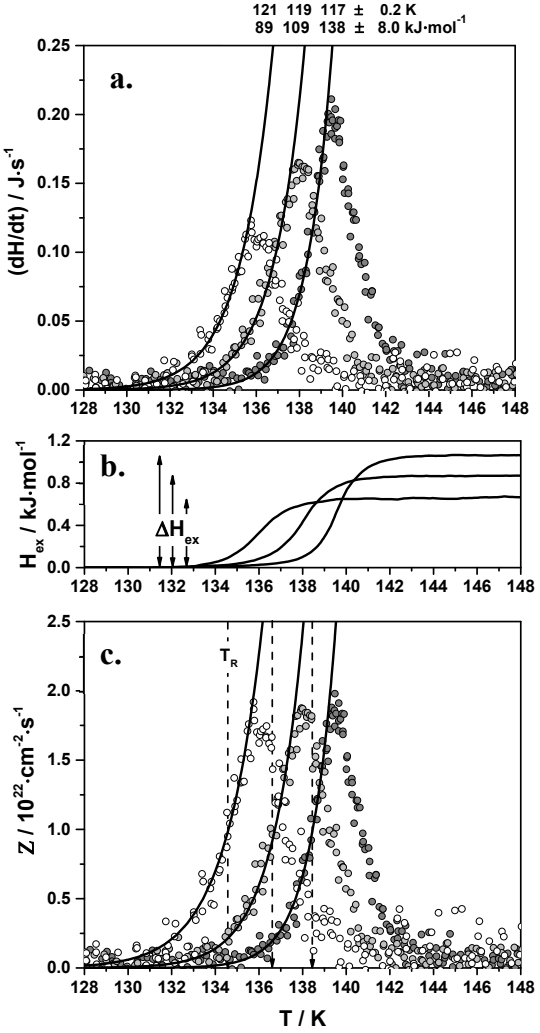

Fig. 5.4. FSC data for rapidly heated 1.5-μm-thick MB films that were fully equilibrated at initial temperatures of 117, 119, and 121K. **(a)** Circles represent the excess heat flow, $(dH/dt)_{ex}$, during each sample' relaxation and solid lines represent the Arrhenius fits of the rate data. **(b)** The enthalpy recovered during the relaxation, calculated from the temperature integral of $(dH/dt)_{ex}$. **(c)** Circles represent the absolute transformation rates, $Z(T)$, of the samples and solid lines represent the Arrhenius fits (see Eq. 5.4). The T_i and the inferred apparent activation energy barrier, $E_{a,R}$, to transformation for each example are shown above the top panel (a).

Fig. 5.4.c shows the transformation flux diagrams for the representative MB samples (T_f of 117, 119, and 121 K). We chose to report *Z(T)* values in units of molecules·cm^{-2}·s^{-1}, which is a common way of expressing flux values in surface science[33]. From the transformation flux, it is easy to obtain other kinetic parameters of rapid relaxation. For example, as shown in Fig. 3.3 of Chapter 3, the transformation front velocity can be calculated using estimates of the characteristic surface density of constituents[34], e.g. 10^{15} molecules·cm^{-2}, and of the spacing between constituent monolayers[14], e.g. 0.34 nm for MB. As shown in Fig. 5.4.c, the transformation flux magnitude reaches a maximum of $2.0 \cdot 10^{22}$ molecules·cm^{-2}·s^{-1}, after which there occurs a breakdown in zero-order kinetics. As we discussed in Chapter 3 and Chapter 4, this breakdown likely results from the physical decoupling of the molecular film from the substrate when the specific volume change in a partially transformed sample induces structural stresses during rapid heating. Although we have not derived a detailed model of such a process, we emphasize that a significant fraction of most samples, e.g. no less than 50%, does relax following zero-order kinetics. As such, we delve into the physical meaning of the Arrhenius parameters for relaxation front propagation during rapid heating of liquid MB films.

Similar to the preliminary results described in Chapter 4, the apparent activation energy of fast relaxation, $E_{a,R}$, is quite large for MB films. Even in the case of MB samples that are fully equilibrated at 121 K (see Fig. 5.4.a), the $E_{a,R}$ value is still near 90 kJ·mol^{-1}, which is 13 times greater than the melting enthalpy of MB, and twice the enthalpy of its vaporization (see Table 3.1 in Chapter 3). The high energy barrier indicates that there is a high degree of cooperative constituent motion[35-38] in the relaxation mechanism during rapid

heating. However, such *a highly activated process is only known to occur*[39-40] at temperatures near T_g (see Chapter 1), and *not at the temperature of fast relaxation, T_R*. In other words, the high $E_{a,R}$ values indicate that the non-equilibrium relaxation of a rapidly heated liquid is largely controlled by the liquid's initial molecular structure. To further validate this preliminary conclusion, we can compare the $E_{a,R}$ values for our series of liquid MB films with distinct fictive temperatures (T_f or T_i).

Fig. 5.5.a shows the apparent activation energies for rapid relaxation for twenty distinct films that were well-equilibrated at T_is in the range of 115 to 124 K. The $E_{a,R}$ values are derived from an Arrhenius fit of each sample's FSC transformation rate, *Z(T)*, as shown in Fig. 5.4.c. The apparent activation energies for dielectric α-relaxation, $E_{a,\tau}$, and for self-diffusion, $E_{a,D}$, in the quasi-equilibrium MB supercooled liquid are shown in Fig. 5.5.a for comparison. These $E_{a,\tau}$ and $E_{a,D}$ values are derived from the VFT fits of MB's reported dielectric relaxation time[41], τ, and MB's self-diffusivity coefficients, D, measured by noble-gas permeation[42]. As detailed in Section 1.5, the activation energies at distinct temperatures can be calculated with the following equation:

$$E_{a,D} \text{ or } E_{a,\tau} = R \cdot \frac{d(\ln(D \text{ or } \tau))}{d(1/T)}, \quad (5.5)$$

where R is the gas constant.

As shown by black circles in Fig. 5.5, when the $E_{a,R}$ values derived from FSC data are plotted as a function of each sample's *initial temperature*, they match the $E_{a,D}$ values for near-equilibrium self-diffusion *at these T_i temperatures*. Indeed, Fig. 5.5.b demonstrates that there is a one-to-one correlation of $E_{a,R}(T_i)$ with $E_{a,D}(T_i)$. Although $E_{a,R}$ values are somewhat lower than the $E_{a,\tau}(T_i)$ values for dielectric structural relaxation, they display a similar temperature dependence when plotted as a function of T_i. However, as

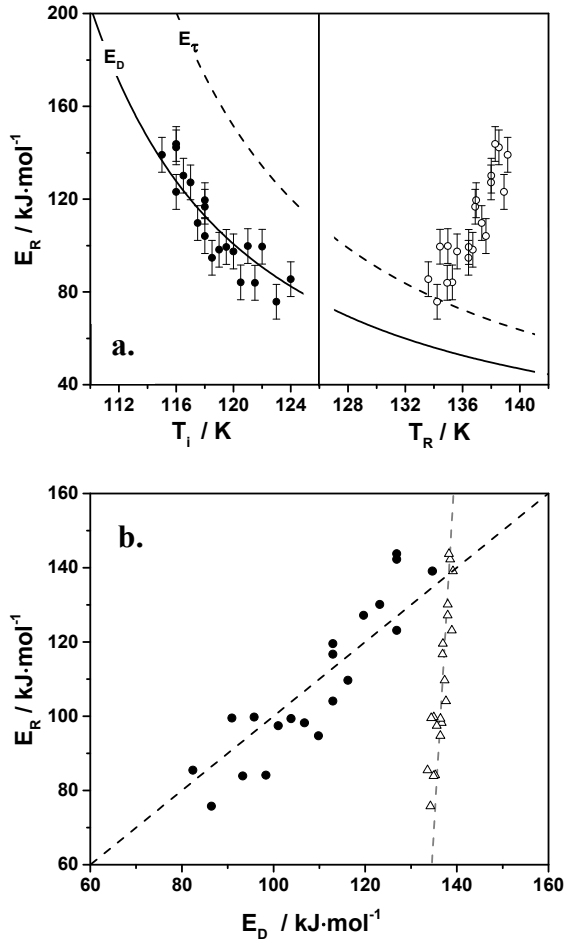

Fig. 5.5. (a) Apparent activation energy barriers to rapid relaxation for quasi-equilibrium liquid films of MB as functions of their initial temperatures, T_is, (solid circles) and their relaxation temperatures, T_Rs (open circles). The solid and dashed curves represent, respectively, the activation energy barriers to self-diffusion, E_D, and to dielectric relaxation, E_τ, calculated as described in the text from Eq. 5. **(b)** The correlation between the energy barriers to relaxation, E_Rs, during rapid heating and the E_D barriers to self-diffusion at each sample's T_i (solid circle). The triangles illustrate the lack of correlation between E_Rs and the E_D at the relaxation temperatures, T_R.

shown in the right panel of Fig. 5.5.a, no correlations are evident when the $E_{a,R}$ values are plotted *as a function of* T_R. In fact, the dependence of $E_{a,R}$ on the characteristic temperature of fast relaxation, T_R, above 130 K is *in complete contrast* to the basic assumption of the front propagation mechanism, as well as the experimentally observed trends (see open symbols in Fig. 5.5.a and Fig. 5.5.b). To illustrate, the relaxation of MB films at the highest T_R is characterized by the highest transformation barrier (approximately 140 kJ·mol^{-1}). However, this activation energy should be the lowest, if the propagation of the relaxation front were controlled entirely by diffusion or α-relaxation in warm liquid at T_R (140 K). Needless to say, it is also several times greater than the near-equilibrium values of $E_{a,D}$ and $E_{a,\tau}$ near 140 K. As I will explain in the proceeding Section, the observed correlation between $Ea_{,R}$ (T_i) and $E_{a,D}(T_i)$ can provide insights into the microscopic details of the front propagation mechanism during rapid heating.

5.6. Proposed mechanism of relaxation front propagation

It is a physically sound and generally accepted notion that the kinetics of any front-propagated, non-equilibrium transformation of a single component system must be governed by constituent self-diffusion near the front, driven by the Gibbs free energy difference. For example, the classical Wilson-Frenkel (WF) model[43-45] describes the temperature dependence of the transformation front velocity, i.e. the transformation rate, as product of two terms:

$$Z(T) \sim e^{-\frac{\Delta G^{\ddagger}(T)}{kT}} \times \left(1 - e^{-\frac{\Delta G}{kT}}\right), \quad (5.6)$$

The first exponential term in Eq. 5.6 describes the kinetic aspects of the transformation, i.e. $\Delta G^{\ddagger}(T)$ is the Gibbs free energy barrier to self-diffusion near the transformation front. The

expression in the parenthesis of Eq. 5.6 reflects the thermodynamic driving force (TDF) of the transition, i.e. ΔG is the free energy difference between the non-equilibrium and equilibrium states of the material[46-47]. The TDF term is a relatively weak function of temperature[48] (see Chapter 6). Consequently, self-diffusion near the transformation front is the primary controlling parameter for the entire relaxation process[49].

In the past, the classical WF model was primarily used to describe crystallite growth in supercooled liquids[38, 43-45, 50-52]. Since Eq. 5.6 does not make any assumptions about the microscopic structure of the two phases, there is no fundamental argument against the application of the WF model to another non-equilibrium heterogeneous transition, e.g. glass softening or liquid relaxation under conditions of rapid heating. However, as we explain in the proceeding paragraphs, the microscopic structure of the *interface* between equilibrium and non-equilibrium phases must be addressed.

As illustrated in Fig. 5.6, two scenarios are possible during rapid, heterogeneous, non-equilibrium relaxation via a transformation front. In the classical model (see Fig. 5.6.a), the transformation front advances by constituents diffusing away from the surface of the "solid" part of the sample. Although this process may require the formation of some kind of transition state[38, 53-55], it is hard to imagine that there would be a significant energy barrier for constituent self-diffusion at the relatively mobile interface between the "solid" and "liquid" phases in Fig. 5.6.a. Thus, the rate-limiting step for fast relaxation in the classical scenario is, essentially, diffusion into a "warm" liquid[32, 56]. Consequently, the $E_{a,R}$ for rapid relaxation would be approximately equal to the $E_{a,D}$ for self-diffusion at T_R. Furthermore, in this first scenario, we would expect $E_{a,R}$ values to decrease for transformations occurring at warmer T_R temperatures, as the equilibrium densities of the

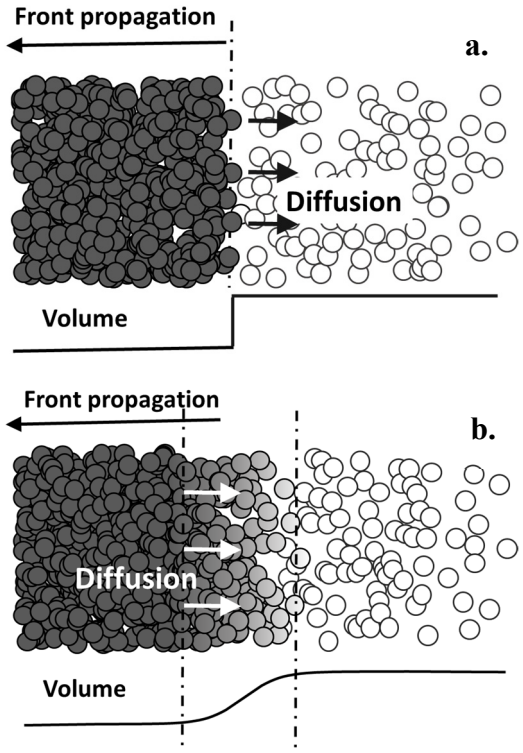

Fig. 5.6. Two Wilson-Frankel-type **models** for a material's non-equilibrium relaxation mechanism. Gray circles represent the "solid" unrelaxed portion and white circles represent the "liquid" relaxed portion of a sample. Lines represent the **molar volume** of the material across the transformation front. **(a)** The rate limiting step in the classical model of relaxation front propagation is the diffusion of constituents in the "liquid" portion of the sample. **(b)** The transformation mechanism proposed in this dissertation Chapter is based on the correlation between the $E_{a,R}$ values and E_D at each sample's initial temperature. The rate limiting step for this model is diffusion of constituents in the "solid" portion of the sample. See text for discussion.

warmer liquids are lower[57].

Although seemingly sound, the classical relaxation mechanism depicted in Fig. 5.6.a is in obvious contrast to our results of rapid relaxation kinetics in liquid MB samples. As shown at the top of Fig. 5.4.a and in Fig. 5.5, the activation energies for relaxation at higher T_Rs are actually higher than the $E_{a,R}$s for lower relaxation temperatures. Additionally, the $E_{a,R}$ values derived from our FSC experiments are actually from 1.2 to 3 times higher than the near-equilibrium values of $E_{a,D}$ for self-diffusion at T_R (50 to 60 kJ·mol^{-1}). Lower values are expected if front propagation were controlled by diffusion in the warm liquid. Therefore, we consider an alternative front propagation scenario, which may be somewhat more realistic during rapid heating.

A close examination of the relaxation mechanism depicted in Fig. 5.6.a reveals several underlying assumptions. Front propagation by this idealized mechanism requires a structural discontinuity at the interface between the "solid" and "liquid" fractions[47]. A single diffusion jump across a few molecular diameters in the warm liquid would be sufficient to accomplish the constituent's transition into the relaxed state. In other words, the mechanism implicitly assumes that the width of the transformation front is limited to a few monolayers at most. Although this may occur during isothermal, low temperature experiments with stable vapor-deposited glasses[21, 32, 56, 58-62], there are many physical reasons why the transformation front is likely to broaden significantly as it propagates from the surface of the sample into its interior during rapid heating.

One reason for front broadening in FSC experiments may be the density difference between the "solid" and "liquid" sample fractions[63-64]. In any case, the configurational relaxation of the film must be accompanied by a significant volume expansion[65], which is

not instantaneous. This time constraint may not pose a problem in relatively slow isothermal experiments[60]. However, as the non-equilibrium heating rate increases, the front velocity is likely to become so high so that the rate of relaxation exceeds the characteristic rate of volume expansion. This would lead to the formation of a progressively wider region in the wake of the transformation front, such that the molar volume of the region varies continuously from that of the "solid" to that of the "liquid" fractions of the sample (see Fig. 5.6.b). This continuous density variation, i.e. the relaxation front broadening, would explain the high activation energy barriers for non-equilibrium relaxation. Indeed, unlike the classical scenario depicted in Fig. 5.6.a, the transition of a constituent from the "solid" to the "liquid" states in the proposed mechanism requires a sequence of diffusion jumps, which become progressively easier as the density decreases. Therefore, the rate-limiting step for the front propagation mechanism is the first diffusion jump, which we believe to occur in an environment that is almost identical to the "solid" phase (as illustrated in Fig. 5.6.b).

In summary, we propose a heterogeneous relaxation mechanism that provides the simplest explanation for our kinetic results. The proposed mechanism is based on the well-established Wilson-Frankel model for non-equilibrium transformations[43-45]. As illustrated in Fig. 5.6.b, we modify the model with single realistic assumption that the interface between the non-equilibrium and equilibrium phase has a *non-zero* width. This modified WF model provides a ready explanation for the high energy barriers to the relaxation of liquid MB films and the dependence of $E_{a,R}$ on initial temperature. Note that this hypothesis is also consistent with the high activation energy barriers to the melting of superheated molecular crystals[24], and to the softening[1] of stable vapor-deposited or

ordinary glassy films, which we observed in our recent FSC studies (see Chapter 3 and Chapter 4). In the following Sections, we offer further evidence in support of the WF front propagation mechanism.

5.7. Correlation between non-equilibrium relaxation rates, Z(T), and equilibrium diffusivity, D(T)

As I argue in Sections 5.5 and 5.6 of this Dissertation, the non-equilibrium relaxation rate of ordinary liquid films is defined primarily by their properties prior to transformation. The main basis for this argument is the high activation energy barriers for front propagation and their dependence on the fictive temperatures of the samples. If this conjecture is correct, there should also be a significant correlation between the non-equilibrium relaxation rate and actual values of equilibrium self-diffusivity at T_i. The observed Arrhenius temperature dependences of the relaxation rates makes it trivial to verify the existence of such a correlation.

As shown in Fig. 5.7.a, the relaxation rates for samples with distinct fictive temperatures can be compared directly at a single test temperature, T'. Each of the lines in Fig. 5.7.a represent the Arrhenius fits of experimental Z(T) values near the characteristic temperature of transformation, T_R, for each sample (see Fig. 5.4.c). These fits can be extrapolated to temperatures a few K outside the data range, if necessary. The solid lines in Fig. 5.7.a are the transformation rates that correspond to the liquid MB films with the lowest (116 K) and the highest (124 K) initial temperature; the dashed lines correspond to intermediate T_i values. As shown by the arrow in Fig. 5.7.a, a test temperature of 135 K is well within the common temperature range of non-equilibrium relaxation for the distinct MB sample set.

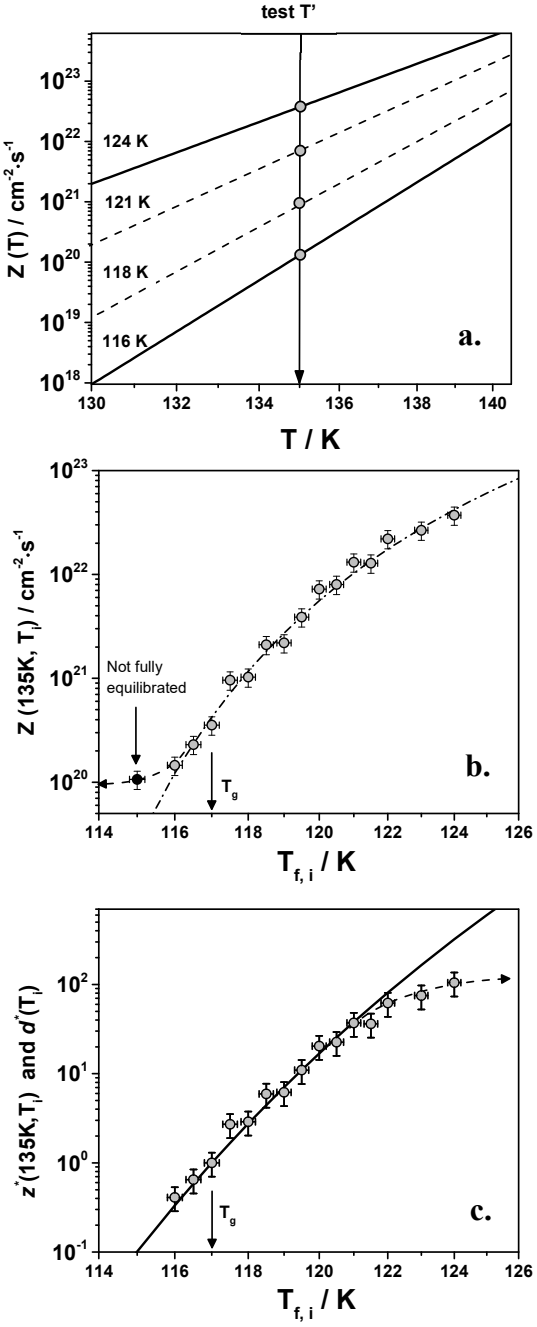

Fig. 5.7. (a) Examples of Arrhenius relaxation rates inferred from the FSC endotherm of rapidly heated quasi-equilibrium MB film (solid and dashed lines). The samples' initial temperatures are shown next to each line (T_i or T_f). The grey circles are the relaxation rate values at the test temperature, T' of 135 K. **(b)** The absolute relaxation rate values at T', Z(135K, T_i), for the entire set of the fully equilibrated liquid MB films (gray circles) plotted as a function of their initial temperature. The dash-dotted line is essentially a polynomial eye guide. **(c)** The scaled relaxation rate values, z^* (circles), and the scaled self-diffusivities, d^* (solid line), plotted as a function of each sample's T_i. See text for details.

Fig. 5.7.b shows the relaxation rate values at a test T' of 135 K for samples with distinct initial temperatures, $Z(135\ K,T_i)$. Note that these values are plotted *in Arrhenius coordinates*. The dashed line is a polynomial fit of the data, which clearly demonstrates that the non-equilibrium relaxation rate at 135 K is a strong "super-Arrhenius" function of T_i, i.e. not a linear function. In fact, as illustrated in Fig. 5.7.c, the *reduced* non-equilibrium relaxation rate, $z^*(T_i)$, and *reduced* diffusivity, $d^*(T_i)$, are nearly identical for samples with fictive temperatures near T_g. The *reduced* z^* and d^* values were calculated by dividing $Z(T_i)$ and $D(T_i)$ by their respective values at T_g. The observed correlation, shown in Fig. 5.7.c, between the non-equilibrium z^* relaxation rate and the near-equilibrium d^* self-diffusivity is the strongest argument in the support of the conjecture that, under condition of rapid heating, the relaxation of an ordinary liquid is controlled primarily by the liquid's initial state.

The correlation between non-equilibrium relaxation rates at high temperatures, T_R, and equilibrium diffusivity near T_g in Fig. 5.7.c is especially good for samples with initial temperatures near or below T_g. However, the $z^*(T_i)$ values begin to deviate from $d^*(T_i)$ as the sample's T_i exceeds 121 K, i.e. 4 K above T_g. We emphasize that such a deviation is expected in the framework of the proposed WF model and can be interpreted as further proof of its validity. According to the model, the transformation rate is a product of the kinetic and thermodynamic terms (see Eq. 5.6). The first exponent in Eq. 5.6 essentially describes the self-diffusivity of MB in the structurally unrelaxed part of the transforming film. Therefore, the first term correlates with near-equilibrium self-diffusivity values at T_i. However, the second term, which is the thermodynamic driving force (TDF), limits the relaxation rate. This term does vary, even for samples prepared at distinct temperatures in

the limited range of the explored T_is (8 K). Ultimately, the second term in Eq. 5.6 is a function of sample "overheating", ΔT, beyond the sample's "equilibrium" temperature, T_i. Overheating is not as extensive for samples with T_is closer to T_R, i.e. ΔT is lower. The Gibb's ΔG in Eq. 5.6, and thus the term in parenthesis, is lower for such samples. Furthermore, in the limit of high ΔT, the ΔG grows and the expression in parenthesis approaches unity. Therefore, it is not surprising that, for liquid MB films with a relatively high T_f, we observe a "breakdown" in the correlation between the non-equilibrium transformation rates and the near-equilibrium self-diffusivities. In fact, this behavior is in good *qualitative* agreement with the proposed modified Wilson-Frenkel model.

5.8. Summary and afterword

The uncovered correlation between non-equilibrium relaxation rates at high temperatures and equilibrium diffusivity near T_g may offer a unique opportunity for rapid and efficient determination of the diffusion coefficients in glasses and other non-crystalline condensed phases. Furthermore, it may be possible to use such FSC-based near-equilibrium diffusivity measurements for materials in which molecular kinetics are inaccessible by all other techniques. The exceptional feature of fast scanning calorimetry is that, with the right choice of experimental parameters, e.g. heating rate and film thickness, even glasses with extremely low fictive temperatures will undergo surface-facilitated softening[66-67].

5.9. References for Chapter Five

1. Cubeta, U.; Bhattacharya, D.; Sadtchenko, V., Communication: Surface-facilitated softening of ordinary and vapor-deposited glasses. *Journal of Chemical Physics* **2017,** *147* (7), 071101.
2. Hodge, I. M., Enthalpy relaxation and recovery in amorphous materials. *Journal of Non-Crystalline Solids* **1994,** *169* (3), 211-266.
3. Alba, C.; Busse, L. E.; List, D. J.; Angell, C. A., Thermodynamic aspects of the vitrification of toluene, and xylene isomers, and the fragility of liquid hydrocarbons. *The Journal of Chemical Physics* **1990,** *92* (1), 617-624.
4. Krall, A. H.; Sengers, J. V.; Kestin, J., Viscosity of liquid toluene at temperatures from 25 to 150 C and at pressures up to 30 MPa. *Journal of Chemical & Engineering Data* **1992,** *37* (3), 349-355.
5. Hinze, G.; Sillescu, H.; Fujara, F., Anisotropic motion of toluene above and below the glass transition studied by 2H NMR. *Chem. Phys. Lett.* **1995,** *232* (1), 154-158.
6. Hinze, G.; Sillescu, H., 2H nuclear magnetic resonance study of supercooled toluene: Slow and fast processes above and below the glass transition. *The Journal of Chemical Physics* **1996,** *104* (1), 314-319.
7. DöS, A.; Hinze, G.; Schiener, B.; Hemberger, J.; Böhmer, R., Dielectric relaxation in the fragile viscous liquid state of toluene. *The Journal of Chemical Physics* **1997,** *107* (6), 1740-1743.
8. Hinze, G., Geometry and time scale of the rotational dynamics in supercooled toluene. *Phys. Rev. E* **1998,** *57* (2), 2010-2018.
9. Yamamuro, O.; Tsukushi, I.; Lindqvist, A.; Takahara, S.; Ishikawa, M.; Matsuo, T., Calorimetric Study of Glassy and Liquid Toluene and Ethylbenzene: Thermodynamic Approach to Spatial Heterogeneity in Glass-Forming Molecular Liquids. *The Journal of Physical Chemistry B* **1998,** *102* (9), 1605-1609.
10. Harris, K. R., Temperature and Density Dependence of the Viscosity of Toluene. *Journal of Chemical & Engineering Data* **2000,** *45* (5), 893-897.
11. Polikhronidi, N. G.; Abdulagatov, I. M.; Magee, J. W.; Batyrova, R. G., Isochoric Heat Capacity for Toluene near Phase Transitions and the Critical Point. *Journal of Chemical & Engineering Data* **2001,** *46* (5), 1064-1071.
12. Chauhan, R. S.; Singh, P.; Singh, C. P., Study of thermoelastic properties of liquid toluene. *Indian Journal of Pure & Applied Physics* **2011,** *49* (10), 535-538.

13. Assael, M. J.; Mylona, S. K.; Huber, M. L.; Perkins, R. A., Reference Correlation of the Thermal Conductivity of Toluene from the Triple Point to 1000 K and up to 1000 MPa. *Journal of Physical and Chemical Reference Data* **2012,** *41* (2), 023101-023101-12.

14. Luning Prak, D. J., Density, Viscosity, Speed of Sound, Bulk Modulus, Surface Tension, and Flash Point of Binary Mixtures of Butylcyclohexane with Toluene or n-Hexadecane. *Journal of Chemical & Engineering Data* **2016,** *61* (10), 3595-3606.

15. Luning Prak, D. J.; Cowart, J. S.; McDaniel, A. M.; Trulove, P. C., Density, Viscosity, Speed of Sound, Bulk Modulus, Surface Tension, and Flash Point of Binary Mixtures ofn-Hexadecane + Ethylbenzene or + Toluene at (293.15 to 373.15) K and 0.1 MPa. *Journal of Chemical & Engineering Data* **2014,** *59* (11), 3571-3585.

16. Marciniak, J.; Bąkowicz, J.; Dobrowolski, M. A.; Dziubek, K. F.; Kaźmierczak, M.; Paliwoda, D.; Rajewski, K. W.; Sobczak, S.; Stachowicz, M.; Katrusiak, A., Most Frequent Organic Interactions Compressed in Toluene. *Crystal Growth & Design* **2016,** *16* (3), 1435-1441.

17. Holzhauer, J. K.; Ziegler, W. T., Temperature dependence of excess thermodynamic properties of n-heptane-toluene, methylcyclohexane-toluene, and n-heptane-methylcyclohexane systems. *The Journal of Physical Chemistry* **1975,** *79* (6), 590-604.

18. Avelino, H. M. T.; Fareleira, J. M. N. A.; Wakeham, W. A., Simultaneous Measurement of the Density and Viscosity of Compressed Liquid Toluene. *International Journal of Thermophysics* **2003,** *24* (2), 323-336.

19. Sastry, N. V.; Patel, S. R.; Soni, S. S., Densities, Speeds of Sound, Excess Molar Volumes, and Excess Isentropic Compressibilities at T = (298.15 and 308.15) K for Methyl Methacrylate + 1-Alkanols (1-Butanol, 1-Pentanol, and 1-Heptanol) + Cyclohexane, + Benzene, + Toluene, + p-Xylene, and + Ethylbenzene. *Journal of Chemical & Engineering Data* **2011,** *56* (1), 142-152.

20. Bhattacharya, D.; Sadtchenko, V., Vapor-deposited non-crystalline phase vs ordinary glasses and supercooled liquids: Subtle thermodynamic and kinetic differences. *J Chem Phys* **2015,** *142* (16), 164510.

21. Sepulveda, A.; Leon-Gutierrez, E.; Gonzalez-Silveira, M.; Clavaguera-Mora, M. T.; Rodriguez-Viejo, J., Anomalous Transformation of Vapor-Deposited Highly Stable Glasses of Toluene into Mixed Glassy States by Annealing Above T-g. *Journal of Physical Chemistry Letters* **2012,** *3* (7), 919-923.

22. Scott, D. W.; Guthrie, G. B.; Messerly, J. F.; Todd, S. S.; Berg, W. T.; Hossenlopp, I. A.; McCullough, J. P., Toluene: thermodynamic properties, molecular vibrations, and internal rotation. *The Journal of Physical Chemistry* **1962,** *66* (5), 911-914.

23. Barlow, A. J.; Lamb, J.; Matheson, A. J., Viscous behaviour of supercooled liquids. *Proceedings of the Royal Society of London. Series A. Mathematical and Physical Sciences* **1966,** *292* (1430), 322-342.

24. Cubeta, U.; Bhattacharya, D.; Sadtchenko, V., Melting of superheated molecular crystals. *The Journal of Chemical Physics* **2017,** *147* (1), 014505.

25. Kearns, K. L.; Whitaker, K. R.; Ediger, M. D.; Huth, H.; Schick, C., Observation of low heat capacities for vapor-deposited glasses of indomethacin as determined by AC nanocalorimetry. *The Journal of Chemical Physics* **2010,** *133* (1), -.

26. Kapko, V.; Zhao, Z. F.; Matyushov, D. V.; Angell, C. A., "Ideal glassformers" vs "ideal glasses": Studies of crystal-free routes to the glassy state by "potential tuning" molecular dynamics, and laboratory calorimetry. *Journal of Chemical Physics* **2013,** *138* (12).

27. Sbirrazzuoli, N.; Guigo, N.; Vyazovkin, S., Isoconversional Kinetics by Fast Scanning Calorimetry. In *Fast Scanning Calorimetry*, Schick, C.; Mathot, V., Eds. Springer International Publishing: 2016; pp 237-257.

28. Vyazovkin, S.; Chrissafis, K.; Di Lorenzo, M. L.; Koga, N.; Pijolat, M.; Roduit, B.; Sbirrazzuoli, N.; Sunol, J. J., ICTAC Kinetics Committee recommendations for collecting experimental thermal analysis data for kinetic computations. *Thermochim. Acta* **2014,** *590*, 1-23.

29. Yoshioka, D., The Heat Capacity of a Solid. In *Statistical Physics: An Introduction*, Springer Berlin Heidelberg: Berlin, 2006; pp 67-81.

30. Mazinani, S. K. S.; Richert, R., Enthalpy recovery in glassy materials: Heterogeneous versus homogenous models. *Journal of Chemical Physics* **2012,** *136* (17).

31. Ahrenberg, M.; Chua, Y. Z.; Whitaker, K. R.; Huth, H.; Ediger, M. D.; Schick, C., In situ investigation of vapor-deposited glasses of toluene and ethylbenzene via alternating current chip-nanocalorimetry. *Journal of Chemical Physics* **2013,** *138* (2).

32. Chen, Z.; Sepulveda, A.; Ediger, M. D.; Richert, R., Dynamics of glass-forming liquids. XVI. Observation of ultrastable glass transformation via dielectric spectroscopy. *Journal of Chemical Physics* **2013,** *138* (12).

33. Mattox, D. M., *Handbook of Physical Vapor Deposition (PVD) Processing*. Elsevier Science: 2010.

34. Bello, I., *Vacuum and Ultravacuum: Physics and Technology*. CRC Press: 2017.

35. Vyazovkin, S., A time to search: finding the meaning of variable activation energy. *Physical Chemistry Chemical Physics* **2016,** *18* (28), 18643-18656.

36. Karamanov, A.; Dzhantov, B.; Paganelli, M.; Sighinolfi, D., Glass transition temperature and activation energy of sintering by optical dilatometry. *Thermochim. Acta* **2013,** *553* (0), 1-7.

37. Schroter, K., Characteristic length of glass transition heterogeneity from calorimetry. *Journal of Non-Crystalline Solids* **2006,** *352* (30-31), 3249-3254.

38. Corberi, F.; Cugliadolo, L. F.; Yoshino, H., Growing Length Scales in Aging Systems. In *Dynamical Heterogeneities in Glasses, Colloids, and Granular Media*, Berthier, L.; Biroli, G.; Bouchaud, J. P.; Cipelletti, L.; Van Saarloos, W., Eds. OUP Oxford: 2011; pp 370-401.

39. Angell, C. A., Perspective on the glass transition. *Journal of Physics and Chemistry of Solids* **1988,** *49* (8), 863-871.

40. Yamamuro, O.; Tatsumi, S., Thermodynamic Study on Simple Molecular Glasses. *Nihon Reoroji Gakkaishi* **2012,** *40* (3), 137-142.

41. Chen, Z.; Richert, R., Dynamics of glass-forming liquids. XV. Dynamical features of molecular liquids that form ultra-stable glasses by vapor deposition. *Journal of Chemical Physics* **2011,** *135* (12), 124515.

42. May, R. A.; Smith, R. S.; Kay, B. D., Mobility of supercooled liquid toluene, ethylbenzene, and benzene near their glass transition temperatures investigated using inert gas permeation. *J Phys Chem A* **2013,** *117* (46), 11881-9.

43. Kirkpatrick, R. J., Crystal growth from the melt: A review. *American Mineralogist* **1975,** *60* (9-10), 798-614.

44. Wilson, H. W., XX. On the velocity of solidification and viscosity of super-cooled liquids. *Philosophical Magazine Series 5* **1900,** *50* (303), 238-250.

45. Frenkel, J., Note on a relation between the speed of crystallization and viscosity. *Phys. Z. Sowjetunion* **1932,** *1*, 498.

46. Duvall, G. E.; Graham, R. A., Phase transitions under shock-wave loading. *Rev. Mod. Phys.* **1977,** *49* (3), 523-579.

47. Hart, E. W., Two-dimensional phase transformation in grain boundaries. *Scripta Metallurgica* **1968,** *2* (3), 179-182.

48. Hoffman, J. D., Thermodynamic Driving Force in Nucleation and Growth Processes. *The Journal of Chemical Physics* **1958,** *29* (5), 1192-1193.

49. Ojovan, M. I.; Lee, W. E., Viscosity of network liquids within Doremus approach. *J. Appl. Phys.* **2004,** *95* (7), 3803-3810.

50. Yoshioka, M.; Hancock, B. C.; Zografi, G., Crystallization of indomethacin from the amorphous state below and above its glass transition temperature. *Journal of Pharmaceutical Sciences* **1994,** *83* (12), 1700-1705.

51. Sun, Y.; Zhu, L.; Kearns, K. L.; Ediger, M. D.; Yu, L. A., Glasses crystallize rapidly at free surfaces by growing crystals upward. *Proc. Natl. Acad. Sci. U. S. A.* **2011,** *108* (15), 5990-5995.

52. Toda, A.; Androsch, R.; Schick, C., Insights into polymer crystallization and melting from fast scanning chip calorimetry. *Polymer* **2016,** *91*, 239-263.

53. Koziatek, P.; Barrat, J. L.; Derlet, P.; Rodney, D., Inverse Meyer-Neldel behavior for activated processes in model glasses. *Phys. Rev. B* **2013,** *87* (22).

54. Gupta, P. K.; Heuer, A., Physics of the iso-structural viscosity. *Journal of Non-Crystalline Solids* **2012,** *358* (24), 3551-3558.

55. Böhmer, R.; Ngai, K. L.; Angell, C. A.; Plazek, D. J., Nonexponential relaxations in strong and fragile glass formers. *The Journal of Chemical Physics* **1993,** *99* (5), 4201.

56. Sepulveda, A.; Swallen, S. F.; Ediger, M. D., Manipulating the properties of stable organic glasses using kinetic facilitation. *Journal of Chemical Physics* **2013,** *138* (12).

57. Stephenson, R. M.; Malanowski, S., *Handbook of the Thermodynamics of Organic Compounds*. Springer Netherlands: 1987.

58. Tylinski, M.; Sepúlveda, A.; Walters, D. M.; Chua, Y. Z.; Schick, C.; Ediger, M. D., Vapor-deposited glasses of methyl-m-toluate: How uniform is stable glass transformation? *The Journal of Chemical Physics* **2015,** *143* (24), 244509.

59. Dalal, S. S.; Ediger, M. D., Influence of substrate temperature on the transformation front velocities that determine thermal stability of vapor-deposited glasses. *J Phys Chem B* **2015,** *119* (9), 3875-82.

60. Chua, Y. Z.; Ahrenberg, M.; Tylinski, M.; Ediger, M. D.; Schick, C., How much time is needed to form a kinetically stable glass? AC calorimetric study of vapor-deposited glasses of ethylcyclohexane. *The Journal of Chemical Physics* **2015,** *142* (5), 054506.

61. Dalal, S. S.; Ediger, M. D., Molecular Orientation in Stable Glasses of Indomethacin. *Journal of Physical Chemistry Letters* **2012,** *3* (10), 1229-33.

62. Dawson, K. J.; Zhu, L.; Yu, L.; Ediger, M. D., Anisotropic Structure and Transformation Kinetics of Vapor-Deposited Indomethacin Glasses. *The Journal of Physical Chemistry B* **2011,** *115* (3), 455-463.

63. Dalal, S. S.; Walters, D. M.; Lyubimov, I.; de Pablo, J. J.; Ediger, M. D., Tunable molecular orientation and elevated thermal stability of vapor-deposited organic semiconductors. *Proc Natl Acad Sci U S A* **2015,** *112* (14), 4227-32.

64. Grzybowski, A.; Koperwas, K.; Kolodziejczyk, K.; Grzybowska, K.; Paluch, M., Spatially Heterogeneous Dynamics in the Density Scaling Regime: Time and Length Scales of Molecular Dynamics near the Glass Transition. *J Phys Chem Lett* **2013,** *4* (24), 4273-8.

65. Ishii, K.; Nakayama, H.; Hirabayashi, S.; Moriyama, R., Anomalously high-density glass of ethylbenzene prepared by vapor deposition at temperatures close to the glass-transition temperature. *Chem. Phys. Lett.* **2008,** *459* (1–6), 109-112.

66. Ramos, S. L.; Chigira, A. K.; Oguni, M., Devitrification properties of vapor-deposited ethylcyclohexane glasses and interpretation of the molecular mechanism for formation of vapor-deposited glasses. *J Phys Chem B* **2015,** *119* (10), 4076-83.

67. Lyubimov, I.; Ediger, M. D.; de Pablo, J. J., Model vapor-deposited glasses: Growth front and composition effects. *Journal of Chemical Physics* **2013,** *139* (14).

Chapter Six: Insights into near-equilibrium molecular kinetics of ordinary and stable, vapor-deposited glasses from FSC experiments

Preface: This Chapter is a modified version of a manuscript submitted to a peer-reviewed journal with co-author Vladislav Sadtchenko.

In Chapter 5, I proposed a Wilson-Frenkel-type mechanism[1-3] as a reasonable approximation for the kinetics of non-equilibrium relaxation by front propagation under conditions of rapid heating. In addition to its relative simplicity, the modified WF model stands out because it relies on a clearly defined thermodynamic parameter, the Gibbs free energy difference (ΔG), as the primary "driving force" for transformation[4] from non-equilibrium to the equilibrium state.

The principle objective of the FSC experiments and data analysis described in this chapter is two-fold. *First*, we provide a *quantitative* validation of the proposed WF mechanism by returning to the dataset described in Chapter 5, the well-equilibrated, ordinary methyl-benzene *liquid* films with distinct fictive temperatures. We demonstrate a *direct* correlation between MB's near-equilibrium molecular kinetics and the observed, absolute, Z relaxation rates at high temperatures. *Second*, we show that the modified WF formalism can be used to gain insights into the molecular kinetics in non-equilibrium phases, e.g. ordinary or vapor-deposited glasses, from the phases' relaxation rates in FSC experiments. Before proceeding with the details of these studies, we wish to reiterate the formalism and underlying assumption of our modified WF model.

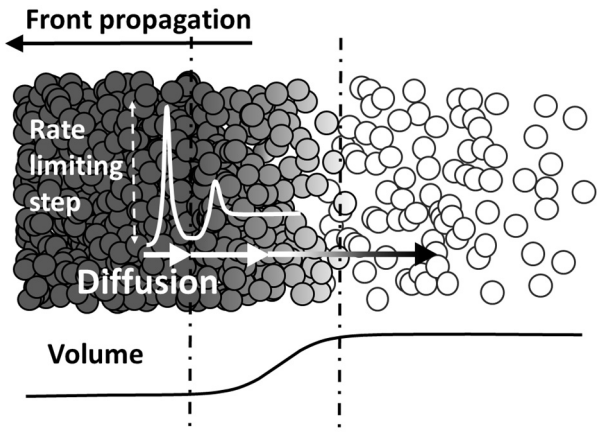

Fig. 6.1. The proposed devitrification mechanism of rapidly heated amorphous phases. Gray circles represent the "solid" unrelaxed portion and white circles represent the "liquid" relaxed portion of a sample. Lines represent the molar volume of the material across the transformation front. The mechanism is based on a modified Wilson-Frenkel model which explains the high values for the apparent activation energy for devitrification front propagation. The interface between the "solid" and "liquid" portions of the sample is not limited to one monolayer. Instead, there is a continuous change molar volume behind the transformation front. The barriers to constituent diffusion in the interface are illustrated in white.

6.1. Overview

During heating with rates typical of our FSC experiments (10^5 K·s^{-1}), a non-crystalline film is in near-perfect vibrational equilibrium (see Chapter 1 and Chapter 2). In other words, thermal lags or gradients are negligible and every portion of the sample has the same vibrational temperature, T. At the same time, the *bulk* of rapidly heated material is in state of near-complete structural arrest. Prior to transformation, the material is configurationally static, i.e. non-ergodic, as a result of the short experimental time scale (10 μs). Thus, the sample's non-equilibrium structure can be characterized by a fictive temperature, T_f. Again, for the sake of simplicity, we will refer to the unrelaxed sample state as "solid" and the fully relaxed sample state as "liquid."

In the absence of bulk structural dynamics, the sample's transformation is limited to the surface or interfacial layer, where additional degrees of freedom facilitate relaxation. As the sample's temperature increases, this surface layer becomes the relaxation front and begins to propagate into the sample's bulk, as illustrated in Fig. 6.1. The width of the transformation front is *unlikely* to be limited to a single molecular diameter. Therefore, the limiting step to the front's propagation is crossing the free energy barrier in the structurally arrested part of the sample (see Chapter 5 for discussion).

For a material characterized by T_f, the absolute transformation rate, $Z(T, T_f)$, of the front-propagated, modified Wilson-Frenkel mechanism can be expressed as a product of two factors (see Eq. 5.6 in Chapter 5): (1) the rate of diffusion at the transformation front and (2) the thermodynamic driving force for transformation[4, 8]. The diffusion factor, $D_F(T, T_f)$, is related to both the change in the sample's vibrational temperature, T, and the structural T_f. The thermodynamic factor is related to the amount of overheating, i.e. the

difference between T and T_f. As a sample's vibrational temperature increases, there is an increase in the magnitude of the (negative) Gibbs free energy difference, $\Delta G(T, T_f)$, between initial sample's state, characterized by T_f, and an equilibrium sample state, for which T_f is equal to T. Therefore, Eq. 5.6 can be rewritten as follows:

$$Z(T, T_f) = Z_0 \times D_F(T, T_f) \times \underbrace{\left(1 - e^{\frac{\Delta G(T, T_f)}{RT}}\right)}_{TDF}, \quad (6.1)$$

where Z_0 is a temperature-independent constant, $D_F(T, T_f)$ is the self-diffusion coefficient in the structurally arrested "solid", and the term in the parenthesis is the thermodynamic driving force (TDF) for the non-equilibrium relaxation process[4, 9-10]. Note that the TDF term in Eq. 6.1, which can vary from a value of 0 to 1, is a relatively weak function of temperature *during* transformation. This is illustrated by the example in Fig. 6.2.

Although the self-diffusion coefficient, $D_F(T, T_f)$, is written out in Eq. 6.1 as a function of both the vibrational T and the sample's the fictive temperature, its dependence on T_f is not explicit. From the conclusions reached in Chapter 5, we can define the non-equilibrium self-diffusion coefficient at the relaxation front with the following Arrhenius function:

$$D_F(T, T_f) = D_{F,0} \times e^{-\frac{E_D(T_f)}{RT}}, \quad (6.2)$$

where $D_{F,0}$ is a temperature-independent coefficient, R is the gas constant, and $E_D(T_f)$ is the apparent activation energy barrier for *equilibrium* self-diffusion in liquid or glass at a *constant* temperature equal to the sample's fictive T_f. Indeed, the experiments with well-equilibrated MB films described in Chapter 5 have already confirmed the validity of

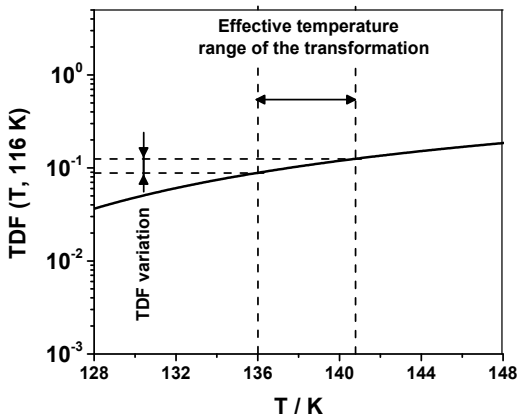

Fig. 6.2. Example of the variations in the thermodynamic driving force (TDF) factor in the Eq. 6.1. at the characteristic temperature range of relaxation (see Fig. 5.4 in Chapter 5). Calculations are for a glassy MB sample with the fictive temperature of 116 K (T_g – 1 K). At the relatively high onset temperatures of the FSC relaxation endotherms, the temperature dependence of the TDF factor can often be neglected in the effective temperature range of transformation. While the TDF varies by less than 20% in that temperature range, the absolute transformation rate changes by more than an order of magnitude (see Fig. 5.7.a in Chapter 5).

equation Eq. 6.2. As illustrated in Fig. 5.5, the apparent activation energy barriers to the relaxation front propagation in rapidly heated liquid films are well correlated with the activation energy barriers to equilibrium self-diffusion[6-7] at the samples' T_fs. For each well-equilibrated ordinary liquid MB sample in Chapter 5, we can combine Eq. 6.1 and Eq. 6.2 to estimate the diffusivity coefficient at the relaxation front as:

$$D_F\left(T,T_f\right)=\frac{Z\left(T,T_f\right)}{Z_0}\times\left(1-e^{\frac{\Delta G\left(T,T_f\right)}{RT}}\right)^{-1}. \quad (6.3)$$

In Eq. 6.3, the Arrhenius fit of the absolute relaxation rate can be substituted for $Z\left(T,T_f\right)$, as illustrated by the lines in Fig. 5.7.a. This substitution is valid in the effective temperature range of transformation.

To summarize our hypothesis, we predict several direct interrelationships between the measured rapid relaxation rates in our FSC experiments, $Z\left(T,T_f\right)$, and the equilibrium and non-equilibrium diffusivity coefficients, $D_s\left(T_f\right)$ and $D_F\left(T,T_f\right)$, in amorphous condensed phases characterized by district fictive temperatures, T_f. The predicted relations are as follows:

$$D_s\left(T_f\right)\propto D_F\left(T,T_f\right)\propto\frac{Z\left(T,T_f\right)}{TDF}. \quad (6.4)$$

In the following sections of this Dissertation chapter, I validate Eq. 6.1-6.4 with calculations of the thermodynamic driving force for the rapid relaxation in ordinary liquid MB films. Then, I demonstrate that our FSC experimental approach and kinetic analysis can be used to gain insights into the exceedingly slow molecular kinetics of non-crystalline materials with fictive temperatures significantly below T_g.

6.2. Experimental details and sample preparation protocols

All of the samples in this Dissertation Chapter were prepared in our quasi-adiabatic, thin-wire fast scanning calorimetry apparatus, for which the design and operations is described in Chapter 2. Each sample film of methyl benzene (T_g of 117 K) was approximately 1.8 μm thick; these micrometer-scale dimensions of MB samples allow for measurements of bulk properties. The thermodynamic and kinetic analysis described in this Chapter utilizes two sets of data. The first dataset is described in Chapter 5, and consists of the thermograms of ordinary liquid MB films that are fully equilibrated at temperatures between T_g - 1 K and T_g + 7 K. The ordinary liquid and melt-cooled glass MB films were prepared using the experimental protocol described in Chapter 5. The additional dataset is from FSC experiments with vapor-deposited, glassy MB films of heightened kinetic stability. These VD samples were prepared by direct vapor deposition onto the calorimeter filament at deposition temperatures between 112 and 124 K. The annealing time for these films was only 50 ms, after which rapid heating was initiated to produce FSC thermograms.

6.3. Calculating thermodynamic parameters for rapid relaxation

As I ascertained in section 6.1, critical tests of the proposed Wilson-Frenkel formalism for rapid relaxation require estimates of the Gibbs free energy difference[3-4, 9-12] between the "solid" and "liquid" portions of the materials at the transformation front (see Eq. 6.1). The meaning of $\Delta G(T, T_f)$ is clarified in Fig. 6.3.a. When the system is configurationally static, i.e. crystal or glass, the changes in its chemical potential with temperature are small compared to that of the liquid phase[4]. In contrast, the free energy of a liquid that is heated quasi-statically, i.e. near-equilibrium, changes drastically with

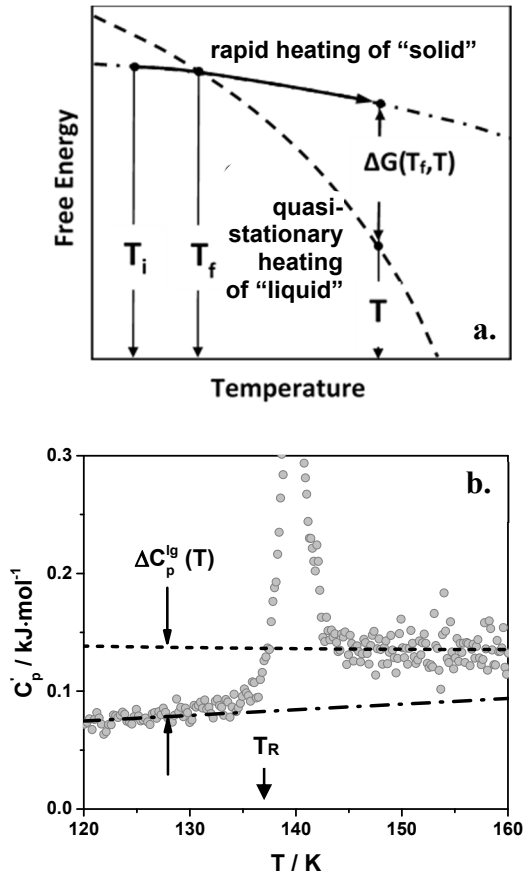

Fig. 6.3. (a) An illustration of the Gibbs free energy difference between a rapidly heated glassy phase and the near-equilibrium quasi-stationary heating of a liquid phase. The configurationally static glassy phase has a free energy temperature dependence that is similar to that of the crystalline material, whereas the higher entropy changes in the heated liquid yield a large change in G with temperature. At the sample's fictive temperature, T_f, the Gibbs free energies of the "solid" and "liquid" phases are identical. As the vibrational temperature of the sample increases, i.e. magnitude of "overheating" grows, the $\Delta G(T, T_f)$ value grows. (b) The FSC thermogram of an ordinary MB film (T_f is 117 K) scaled by the sample size. The molar heat capacity of the fully liquid sample (dashed line) and the fully glassy sample (dot-dashed line) can be fit and extrapolated in the temperature range of transformation (135 to 145 K). The heat capacity difference, $\Delta C_p^{lg}(T)$, between these phases can be used to calculate the Gibbs free energy difference, $\Delta G(T, T_f)$, illustrated in (a).

temperature. Therefore, a rapidly-heated, non-equilibrium "solid" sample has a weaker free energy dependence than the equilibrium "liquid" sample, as shown by the dashed lines in Fig. 6.3.a. As the temperature of the sample increases from T_i during an FSC scan, the $\Delta G(T, T_f)$ increases until the onset of fast relaxation at T_R.

The values of $\Delta G(T, T_f)$ for sample films can be calculated as a function of the sample's vibrational temperature and fictive temperature, if we possess accurate data for the molar heat capacities of liquid and glassy materials in the temperature range of transformation. For example, as illustrated by Fig. 6.3.b, the molar C_p^l and C_p^g values of MB can be derived from FSC thermograms and literature specific heat values[13] in the typical temperature range of our FSC scans (e.g. from 100 to 180 K). Thus, the Gibbs free energy difference between the final and initial states of the sample can be calculated with the following integral expression[4]:

$$\Delta G(T_f \to T) = \int_{T_f}^{T} \Delta C_p^{lg}(T) dT + T \cdot \int_{T_f}^{T} \frac{\Delta C_p^{lg}(T)}{T} dT, \quad (6.5)$$

where $\Delta C_p^{lg}(T)$ is the heat capacity *difference* between the molar heat capacities of the sample in the quasi-equilibrium liquid and the unrelaxed glassy states. In essence, the first integral is the enthalpy difference and the second is the entropy difference between the non-equilibrium and equilibrium states of the material at the vibrational temperature, T, of the sample.

Fig. 6.4.a shows the calculated temperature dependence of the free energy difference, $\Delta G(T, T_f)$, in well-equilibrated liquid MB samples with three distinct fictive temperatures (T_i). In agreement with our preliminary findings in Chapter 5, for any particular test temperature (e.g. *T'* of 135 K), the magnitude of $\Delta G(T, T_f)$ is greater for

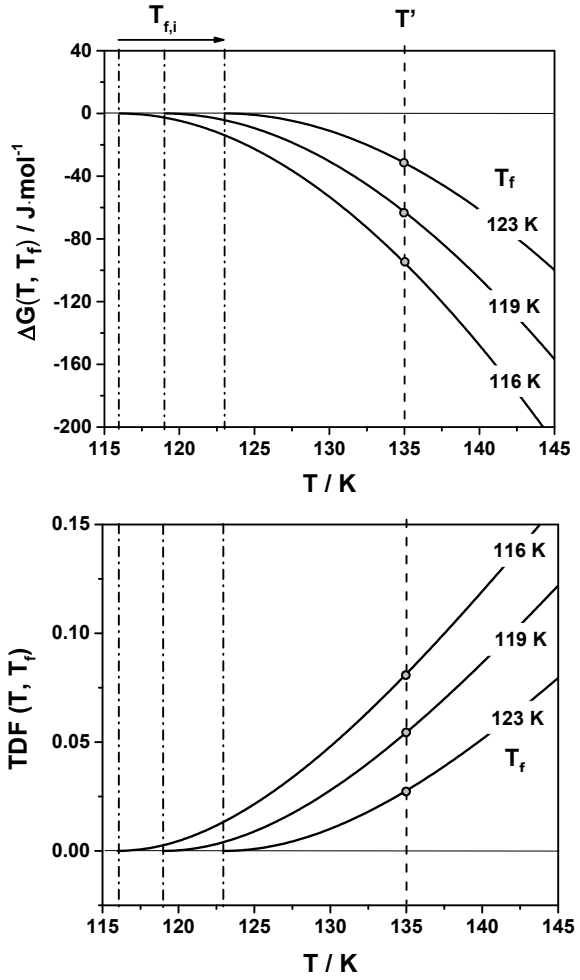

Fig. 6.4. The calculated thermodynamic parameters for ordinary liquid films of MB with well-defined fictive temperatures (116, 119, and 123 K) prepared as described in Chapter 5. (a) The Gibbs free energy difference between the "glassy" and "liquid" sample phase, calculated using Eq. 6.5 from the molar heat capacities of the films. (b) The thermodynamic driving force (TDF) of rapid relaxation, calculated from $\Delta G(T, T_f)$ as described in Eq. 6.1 and Fig. 6.3.

more stable samples with a lower fictive temperature. Consequently, the TDF factor in Eq. 6.1 is greater for samples with a lower T_f. As I explain further in the Section 6.5, the same trend is observed for stable VD samples of MB as their fictive temperatures become significantly lower than the standard T_g.

6.4. Correlation between low-temperature equilibrium self-diffusivities and self-diffusivities during high-temperature transformation

Figure 6.5 summarizes the observed correlations between the absolute relaxation rate, $Z(T, T_f)$, and the equilibrium and non-equilibrium diffusion coefficients, $D_s(T_f)$ and $D_F(T, T_f)$, for ordinary liquid methyl benzene samples that were fully equilibrated at initial temperatures between 116 and 124 K. As discussed in Chapter 5, to simplify the comparison, these dynamic parameters were scaled by their values at T_g of MB (117 K). The samples' transformation rates, $z^*(T,T_f)$, and the high temperature self-diffusivities, $d^*(T,T_f)$, are reported at a test temperature T' of 135 K. As we already mentioned, this value corresponds to the mid-point in the range of transformation temperatures, e.g. 130 to 140 K, for distinct, rapidly heated samples and therefore minimizes errors due to extrapolation of inferred Arrhenius dependences to lower or higher temperatures (see Fig. 5.7). The $D_F(135\ K, T_f)$ values were calculated from the transformation rates using Eq. 6.3 and the Gibbs free energy analysis in the preceding sections of this chapter.

Unlike the absolute relaxation rates, $z^*(135\ K, T_f)$, in Fig. 6.5.a, the diffusivity values at the relaxation front, $d_F^*(135\ K, T_f)$, in Fig. 6.5.b, match the equilibrium $d_s^*(T_f)$ values almost perfectly for the entire range of the samples' fictive (initial) temperatures. Therefore, adjusting the absolute relaxation rate by the thermodynamic driving force

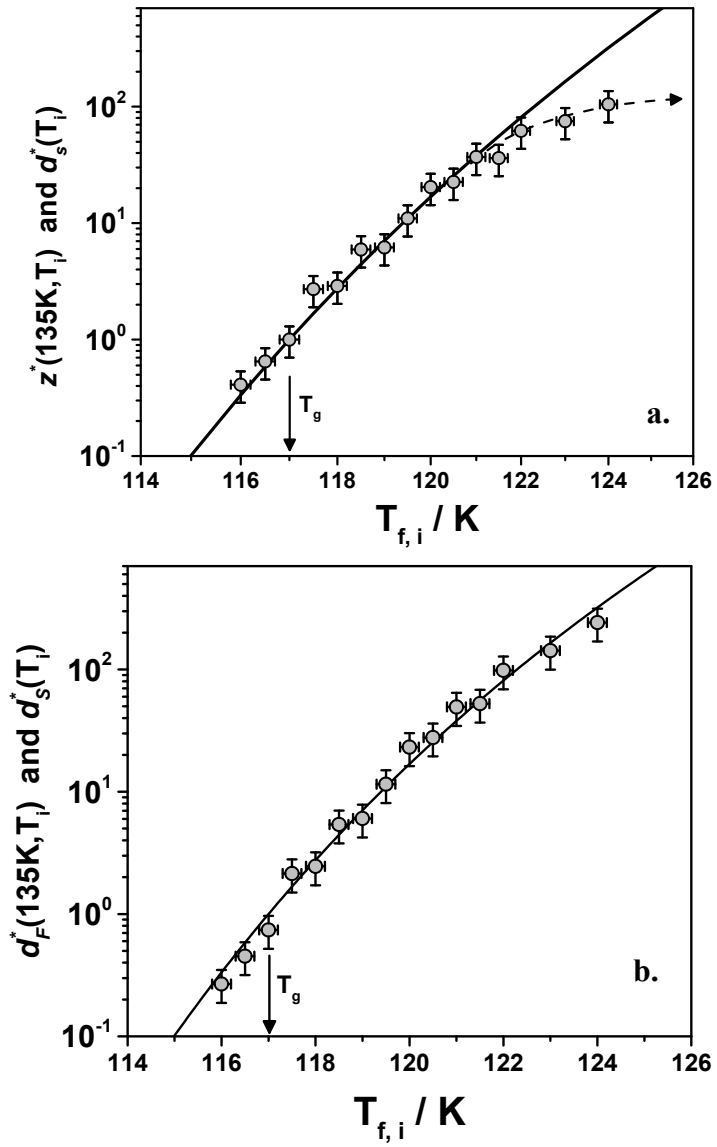

Fig. 6.5. The absolute relaxation rate and the self-diffusion coefficients for ordinary liquid MB films that were fully equilibrated at initial temperatures ranging from T_g - 1 K to T_g + 7 K, prepared as described in Chapter 5. The lines represent the equilibrium self-diffusion coefficients, $D_S(T_f)$, for liquid MB[6] at temperatures equal to T_f. These values are scaled by the coefficient's value at T_g resulting in the $d_S^*(T_f)$ values illustrated by the black lines. (a) The circles represent the scaled, absolute relaxation rate, $z^*(135K,T_i)$, for each sample film at the test vibrational temperature. (see Fig. 5.7). The estimated error bars are shown. (b) Using Eq. 6.3, we estimate the diffusivity coefficient at the relaxation front, $D_F(135K,T_f)$, at the test temperature. These values are scaled by the corresponding value measured for a sample with a fictive temperature equal to T_g. The resulting $d_F^*(135K,T_f)$ are plotted as circles, with estimated error bars. Note that the differences between literature and measured diffusivity values in panel (b) are small compared to the differences between $z^*(135K,T_i)$ and $d_S^*(T_f)$ values in panel (a) for MB samples with high fictive temperatures. See text for details.

(Eq. 6.1 and Eq. 6.3) significantly improves the connection between the kinetic parameters measured under non-equilibrium conditions, i.e. rapid heating, and the molecular dynamics of the equilibrium liquids. Furthermore, the correlation plot in Fig. 6.6 examines the strength of this qualitative link between equilibrium diffusivity at T_f and high temperature, non-equilibrium self-diffusion at T_R. The slope of the plot is 1.03 ± 0.3, implying a proportionality relation of:

$$D_F(T, T_f) = \gamma \cdot D_s(T_f), \quad (6.6)$$

where γ is simply a scaling coefficient. Again, $D_F(T, T_f)$ is the *high temperature* (e.g. T' is T_g + *18* K), self-diffusion coefficient in a rapidly heated glassy or liquid MB film with a distinct fictive (or initial) temperature, whereas $D_s(T_f)$ is proportional to the *near-equilibrium* self-diffusion coefficient at low temperatures, (T_g - *1* K to T_g + *7* K).

The extreme physical conditions present during FSC experiments, i.e. non-equilibrium heating with rates of thousands of K per second, may make the simple relationship between equilibrium and non-equilibrium self-diffusivities given by Eq. 6.6 seem remarkable. We emphasize, however, that the earliest experiments with glasses reveal an equally "remarkable" property of these condensed phases. Unlike crystalline materials, glasses have been shown to have a strong "memory" of the conditions of their preparation, i.e. their thermal or mechanical history[14]. In fact, the concept of fictive temperature, explained in Chapter 1 and used extensively throughout this Dissertation, was introduced as early as 1946 by Tool[15] and co-workers, in an attempt to formalize this remarkable phenomenon. Thus, we believe that the implied simple relationship between the sample's molecular dynamics in and out of equilibrium (Eq. 6.6) is a direct consequence of the

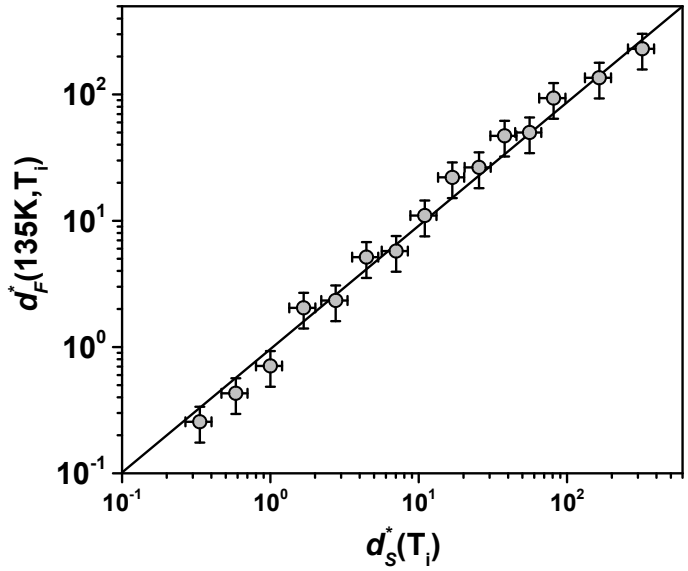

Fig. 6.6. Correlation plot between the non-equilibrium diffusivity at the fast relaxation front and the equilibrium diffusivity, each scaled by its value at T_g. The $d_F^*(135K, T_f)$ values are scaled front diffusivities for the ordinary liquid MB samples shown in Fig. 6.5.b. The $d_s^*(T_f)$ values are from isothermal gas-permeation experiments[7]. Error bars indicate uncertainties in $d_F^*(135K, T_f)$ values. The slope of the correlation plot is 1.03 ± 0.3 (solid line).

simplified phase transformation kinetics (zero-order and Arrhenius surface-facilitated relaxation) in the limit of extreme heating rates.

6.5. Insights into equilibrium molecular dynamics in stable vapor-deposited glasses with low fictive temperatures

As I discuss in Chapter 1, physical vapor deposition at temperatures below T_g often results in non-crystalline materials with "abnormally" low enthalpy and specific volume[16-19]. The high kinetic stability of these samples is manifested by the higher temperatures of devitrification during slow, quasi-static heating[20]. Historically[17, 21], formation of these phases was observed at temperatures near $0.86 \cdot T_g$ when vapor deposition rates were kept below 1 nm·s^{-1}. Nevertheless, as demonstrated by Bhattacharya *et.al.*[22], relatively stable VD glasses of MB can be prepared at temperatures as high $0.95 \cdot T_g$ with deposition rates as high as 15 nm·s^{-1}. Despite not representing the most stable VD glasses of MB, the micrometer-scale films prepared under such conditions offer an opportunity to demonstrate the utility of the FSC methodology for studies of low fictive temperature non-crystalline systems in general.

Before proceeding, we note that these stable VD films of methylbenzene may not be the most ideal system for gaining insights into the fundamental properties of *ordinary* glasses. In particular, MB may form structurally unique amorphous phases during vapor deposition below T_g. This conclusion is based[22], in part, on a diverging dependence of the MB's initial enthalpy on deposition temperature. As shown in Fig. 6.7, the initial enthalpy of the sample VD films is lower than the enthalpy of quasi-equilibrium liquid MB below and even slightly above T_g (119 K), which is in contrast to the enthalpy dependence of

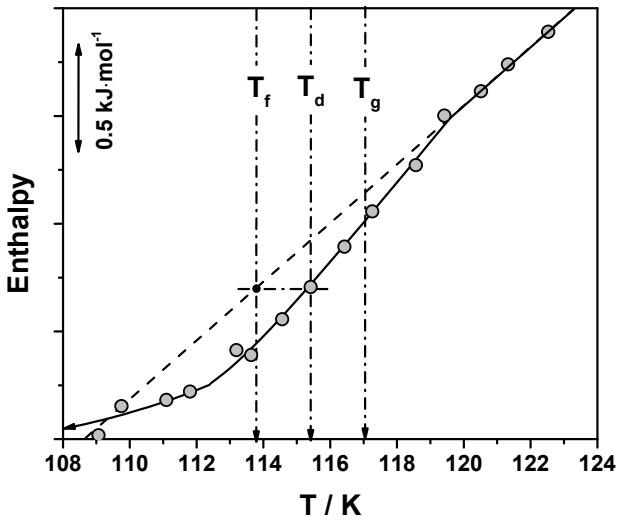

Fig. 6.7. The fictive temperatures, T_f, for vapor deposited stable films of MB was determined by comparing the relative enthalpies of the sample films (circles) at the initial scan temperature, T_i or T_d, to supercooled liquid enthalpy (dashed line). The anomalous properties of vapor-deposited films are evident by the loss of correlation below T_g + 2 K, which is described in detail in Ref [5].

ordinary glass or liquid MB films with this initial or fictive temperature. Thus, the FSC experiments and the results described in this section may not be universally pertinent to all glassy materials. Yet, MB films prepared by vapor deposition below T_g with rates near 15 nm·s^{-1} *are* non-crystalline and *are* significantly more stable[22] that ordinary melt-cooled liquid or glassy samples. Consequently, these samples can be used to gain insights into the *possible* temperature variations of a glassy material's kinetic parameters in the sub-T_g region.

Our previous FSC experiments[5, 22] with VD samples of MB were afflicted by instrumental issues, e.g. electromagnetic interferences due to inadequate shielding and electrical power instabilities. The low signal-to-noise ratio of the samples' FSC thermograms precluded a kinetic analysis, with the exception[22] of the most stable MB films vapor deposited at 112 K. Therefore, taking advantage of the improved DAQ performance after changing laboratory conditions, I have repeated the experiments with stable MB films vapor deposited with a rate of approximately 15 nm·s^{-1}. The results of these new measurements are summarized in Fig. 6.8, which compares the rapid relaxation of non-crystalline VD films with distinct deposition temperatures, T_d. As illustrated on Fig. 6.8.a, the FSC endotherm of each VD sample shifts toward higher temperatures as the T_d is lower from 117 to 112 K. Furthermore, the magnitude of the FRE endotherm increases almost exponentially with T_d while their widths decrease; i.e. smaller temperature interval for transformation. At deposition temperatures below 112 K, the endotherms broadened and they begin to shift back towards lower temperatures (data is not shown), which signifies the progressively lower kinetic stability of these VD samples. In summary, the new measurement are in excellent agreement with the results of past FSC studies[5, 22], that had

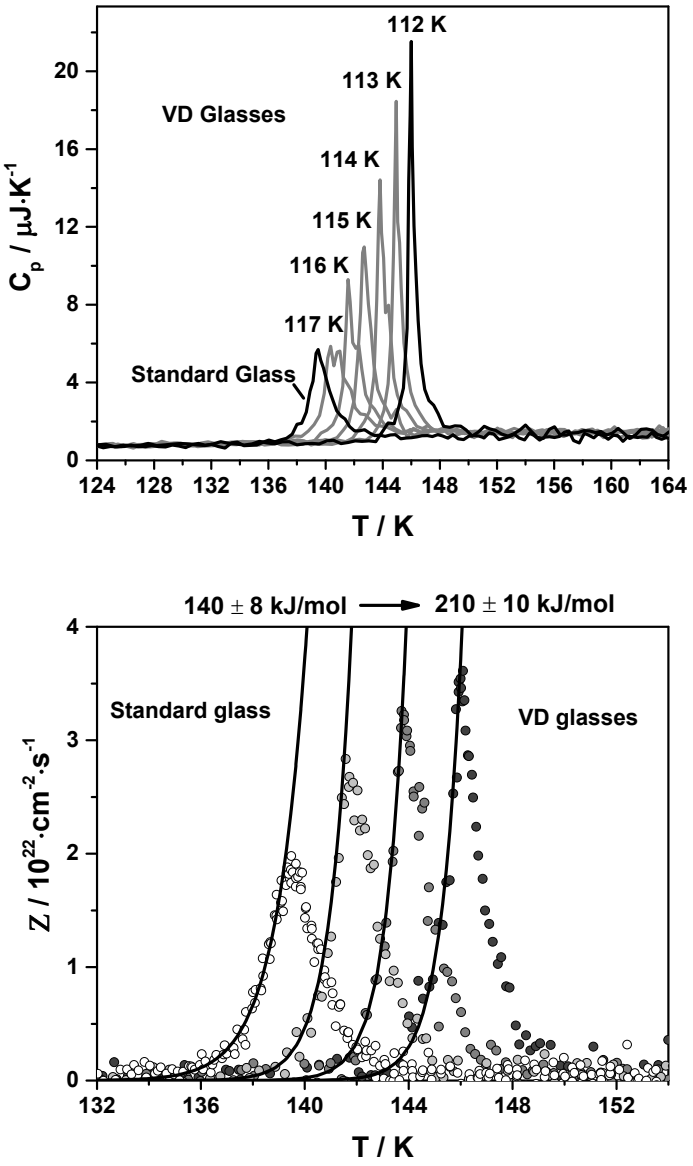

Fig. 6.8. (a) The FSC thermograms of the vapor deposited MB samples prepared at progressively lower deposition temperatures (T_d as low as T_g – 5 K). For comparison, we include an FSC thermogram of a standard glass, prepared by slow melt cooling to T_g (see Chapter 4). Vapor deposition at temperatures below T_g produces samples with kinetic stabilities higher than the standard glass. This is manifested by the higher onset temperature of relaxation in the heat capacity data. For example, the onset of relaxation for an VD sample prepared at T_g – 5 K is approximately 144 K, significantly higher than the onset of 138 K for the VD sample prepared at T_g. **(b)** The absolute relaxation rates, *Z(T)*, for a subset of the vapor deposited MB samples shown in panel (a) with deposition temperatures of 112, 114, and 116 K. For comparison, the relaxation rate of a standard melt-cooled glass with a fictive temperature equal to T_g is included (see Chapter 4). The apparent activation energy for rapid relaxation increases substantially, as illustrated at the top of panel (b).

also revealed a critical deposition temperature of 112 K for the formation of the very stable VD films when the deposition vapor flux was approximately 15 nm·s^{-1}.

Fig. 6.8.b shows the representative results of the kinetic analysis for FSC thermograms of vapor-deposited micrometer-scale MB samples. The absolute transformation rates, $Z(T, T_d)$, for all samples are expressed as the number of MB molecules crossing the relaxation front per surface area, per time. The $Z(T, T_f)$ values for an ordinary glassy MB film with a fictive temperature of 117 K (standard glass) is shown for comparison. In every case, an Arrhenius function provides an excellent fit for the leading edges of the devitrification rate diagrams. However, in contrast to the relaxation rate kinetics observed for the ordinary glass, the zero-order relaxation rate of each VD sample is characterized by a significantly higher apparent activation energy barrier. In fact, the E_a (205 ± 12 kJ·mol^{-1}) for the most stable MB sample vapor deposited at 112 K does not just exceed E_a for the standard ordinary glass (140 ± 8 kJ·mol^{-1} kJ), but approaches the energy barriers to *melting* front propagation in the superheated crystalline films of methyl benzene, as described in Chapter 3 of this Dissertation.

In contrast to the FSC experiments described in Chapter 5, where fully equilibrated liquid MB films each had a well-defined T_f that was simply equal to the film's initial temperature, the fictive temperature of each MB films prepared by vapor deposition is not immediately apparent. Fortunately, we can use the enthalpy analysis carried out by Bhattacharya *et. al.*[5] on a set VD glasses identical to those described here to quickly infer the fictive temperature for a VD film prepared at a particular T_d (see Fig. 6.7). By calculating the fictive temperature of our VD samples, we can further illustrate the differences between the high temperature relaxation kinetics of highly stable VD glass

films and the relaxation kinetics of ordinary glassy and supercooled liquid films. Therefore, we can compare the kinetic parameters of the amorphous material characterized by a fictive temperature below T_g with the parameters of the compound characterized by fictive temperatures near or above T_g.

Fig. 6.9 shows the apparent activation energy barriers to relaxation front propagation for non-crystalline MB samples with distinct fictive temperatures. As shown in the figure, at temperatures above T_g, the E_a values are nearly indistinguishable for VD and ordinary liquid samples. However, the activation energy values begin to diverge rapidly as T_f decreases below 117 K. Even more remarkably, the apparent activation energy to front propagation reaches a maximum of approximately 205 $kJ \cdot mol^{-1}$ and remains nearly constant for VD phases with fictive temperatures that range from 114 to 108 K. The sudden change in the temperature dependence of E_a strongly implies a crossover or change in the non-equilibrium self-diffusivity behavior at the relaxation front of low T_f samples during high temperature relaxation. Furthermore, according to conclusions reached in Sec. 6.4, this change also implies a cross-over in the equilibrium self-diffusivity of the compound at low temperatures, at or below T_g.

Fig. 6.9b shows the high temperature self-diffusion coefficients, $D_F(T, T_f)$, in ordinary and vapor-deposited MB films with distinct fictive temperatures. These values were calculated using Eq. 6.3 from the absolute relaxation rates, $Z(135\ K, T_f)$, at the test temperature of 135 K. We also performed calculations identical to those described in Section 6.3, in order to estimate the Gibbs free energy and the TDF factors for each VD sample. As described in Section 6.4, we present the kinetic parameters for non-equilibrium

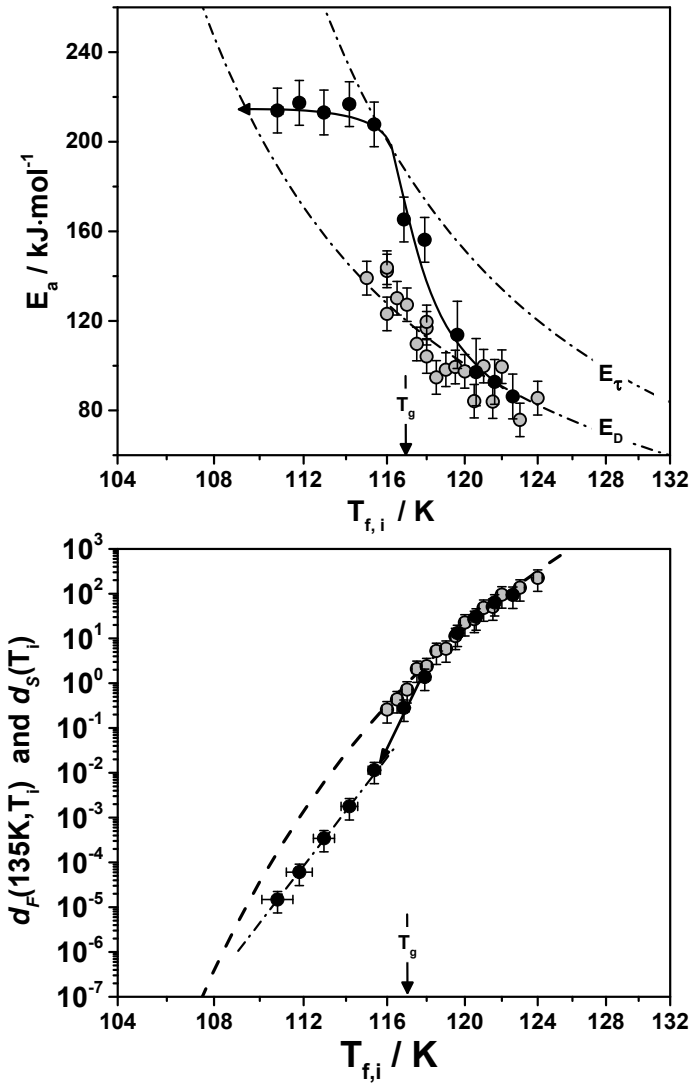

Fig. 6.9. The differences in rapid relaxation kinetics between ordinary liquid films (gray circles) and vapor-deposited glassy films (black circles) of micrometer-scale methyl benzene (MB). The samples were prepared as described in Section 6.2. The fictive temperatures of VD films were calculated as described in Fig. 6.7 and the fictive temperatures of liquid films were equal to the samples' initial temperatures. The T_f values are plotted as inverse temperature. **(a)** The apparent activation energy, E_a, of relaxation front propagation plotted as a function of the samples' fictive temperatures. The activation energies (dashed lines) of structural relaxation, E_τ, and equilibrium self-diffusivity, E_D, for MB are calculated as described by Eq. 5.5 from literature values of dielectric relaxation time and noble gas permeation studies. **(b)** Arrhenius plot of diffusivity parameters at T_f. The dashed line represents the scaled self-diffusivity values, $d_S^*(T_f)$, of equilibrium liquid MB. For ordinary liquid films with fictive temperatures above T_g, the non-equilibrium diffusivity values, $d_F^*(135K, T_f)$, at the relaxation front correlate well with $d_S^*(T_f)$. For VD samples with fictive temperatures near or below T_g, the $d_F^*(135K, T_f)$ values are lower than predicted by $d_S^*(T_f)$.

and equilibrium diffusivity in their scaled form, d_F^* and d_S^*, to facilitate comparison between samples with distinct fictive temperatures.

In Fig. 6.9.b, the self-diffusion coefficients derived for VD films of MB above 119 K are indistinguishable from those derived for melt cooled MB sample films. For both sample preparation techniques, the d_F^* values are well approximated by the same VFT equation, which represents near-equilibrium self-diffusivity at temperatures equal to the samples' fictive temperatures (see dashed line is Fig. 6.9.b). However, as the deposition and fictive temperatures are lowered below T_g, the d_F^* values of the stable VD samples begin to diverge from those of the ordinary MB glasses. The drop in the relaxation front self-diffusivity values for VD films coincides with the increase in the apparent activation energy barriers to relaxation front propagation (see Fig. 6.9.a). In other words, for temperatures in the range of $T_g \pm 2$ K, the kinetic parameters of vapor deposited phases exhibit cross-over behavior. Finally, as the fictive temperature of the VD films drops below 115 K and the activation energy for front propagation plateaus, the temperature dependence of D_F changes from a VFT, super-Arrhenius dependence to a temperature dependence that is almost perfectly Arrhenius.

In accord with the conclusions reached in Sections 6.3 and 6.4, the scaled high-temperature diffusivities inferred from the absolute relaxation rates of rapidly heated samples *must* have a strong correlation with the *equilibrium* values of self-diffusivity at temperatures equal to the samples' fictive temperatures. To our knowledge, there have been no direct measurements of self-diffusion coefficients in any non-crystalline MB glasses with a T_f below 115 K. Therefore, independent of whether the structure of an amorphous VD film is identical to that of an ordinary low fictive temperature glass[7, 23-25], the

discovered kinetic crossover may represent an important contribution to the field of low-temperature amorphous materials. Indeed, our preliminary FSC results indicate that, in the limit of low sample T_f, the temperature dependence of the kinetic mobility parameters (e.g. self-diffusivity) appears to undergo a crossover from highly non-Arrhenius to Arrhenius behavior. In fact, our results implicate the existence of a *dynamic fragile-to-strong*[26-27] transition in fragile MB glasses at fictive temperatures below T_g. Prior to the publication of this Dissertation, such *fragile-to-strong* transitions were only observed[26-27] in strong glasses at temperatures *above* T_g.

6.6. Summary and afterword

The high temperature relaxation (softening or devitrification) kinetics of quasi-equilibrium liquid, melt-cooled glass, and vapor deposited amorphous phases of methyl-benzene (MB) were analyzed in the framework of a modified Wilson-Frenkel model of non-equilibrium phase transitions by a surface- or interface-facilitated mechanism. In the case of ordinary liquids and glasses, we found a strong linear correlation between high temperature self-diffusivity at the relaxation front during rapid heating and the self-diffusivity at the low initial temperatures of the samples prior to heating. We applied our kinetic analysis to stable, vapor deposited MB glasses with progressively lower fictive temperatures and revealed a dynamic crossover regime. This crossover is manifested as a plateau in apparent activation energy barriers to relaxation and as a change from a highly super-Arrhenius to an Arrhenius temperature dependence of self-diffusivity during rapid heating. From a perspective that includes the strong correlation between high and low temperature diffusivities observed in experiments with ordinary glasses (see

Section 6.4), I interpret this crossover in the kinetic parameters of vapor-deposited phases as an indication of a possible *fragile-to-strong* dynamic transition.

I emphasize that the experiments described in this chapter are intended primarily as a demonstration of the FSC technique's utility for studying glassy phases under conditions of rapid heat loading. In fact, such experiments have the potential to gain insights into the slow molecular kinetics of amorphous materials at temperatures significantly below standard T_g. Of course, further research is needed to fully validate the groundbreaking findings and ideas described in this Dissertation. In the next chapter I suggest future research directions to fulfill this goal.

6.7. References for Chapter Six

1. Wilson, H. W., XX. On the velocity of solidification and viscosity of super-cooled liquids. *Philosophical Magazine Series 5* **1900,** *50* (303), 238-250.

2. Frenkel, J., Note on a relation between the speed of crystallization and viscosity. *Phys. Z. Sowjetunion* **1932,** *1*, 498.

3. Kirkpatrick, R. J., Crystal growth from the melt: A review. *American Mineralogist* **1975,** *60* (9-10), 798-614.

4. Hoffman, J. D., Thermodynamic Driving Force in Nucleation and Growth Processes. *The Journal of Chemical Physics* **1958,** *29* (5), 1192-1193.

5. Bhattacharya, D.; Sadtchenko, V., Enthalpy and high temperature relaxation kinetics of stable vapor-deposited glasses of toluene. *The Journal of Chemical Physics* **2014,** *141* (9), 094502.

6. May, R. A.; Smith, R. S.; Kay, B. D., Mobility of supercooled liquid toluene, ethylbenzene, and benzene near their glass transition temperatures investigated using inert gas permeation. *J Phys Chem A* **2013,** *117* (46), 11881-9.

7. Smith, R. S.; May, R. A.; Kay, B. D., Probing Toluene and Ethylbenzene Stable Glass Formation Using Inert Gas Permeation. *Journal of Physical Chemistry Letters* **2015,** *6* (18), 3639-3644.

8. Stillinger, F. H., Relaxation and flow mechanisms in ‘‘fragile’’ glass-forming liquids. *The Journal of Chemical Physics* **1988,** *89* (10), 6461-6469.

9. Hart, E. W., Two-dimensional phase transformation in grain boundaries. *Scripta Metallurgica* **1968,** *2* (3), 179-182.

10. Larche, F. C.; Cahn, J. W., Thermochemical equilibrium of multiphase solids under stress. *Acta Metallurgica* **1978,** *26* (10), 1579-1589.

11. Duvall, G. E.; Graham, R. A., Phase transitions under shock-wave loading. *Rev. Mod. Phys.* **1977,** *49* (3), 523-579.

12. Zhang, L.; Li, Y.-H.; Cai, L.-C., A formulism of two-phase equilibrium and phase diagram for elastic-plastic deformed system under non-hydrostatic stress conditions: Formulations and verification. *International Journal of Plasticity* **2018**.

13. Yamamuro, O.; Tsukushi, I.; Lindqvist, A.; Takahara, S.; Ishikawa, M.; Matsuo, T., Calorimetric Study of Glassy and Liquid Toluene and Ethylbenzene: Thermodynamic Approach to Spatial Heterogeneity in Glass-Forming Molecular Liquids. *The Journal of Physical Chemistry B* **1998,** *102* (9), 1605-1609.

14. Hodge, I. M., Enthalpy relaxation and recovery in amorphous materials. *Journal of Non-Crystalline Solids* **1994,** *169* (3), 211-266.

15. Tool, A. Q., Relation between inelastic deformability and thermal expansion of glass in its annealing range. *Journal of the American Ceramic Society* **1946,** *29* (9), 240-253.

16. Kearns, K. L.; Swallen, S. F.; Ediger, M. D.; Wu, T.; Sun, Y.; Yu, L., Hiking down the energy landscape: Progress toward the Kauzmann temperature via vapor deposition. *J. Phys. Chem. B* **2008,** *112* (16), 4934-4942.

17. Ishii, K.; Nakayama, H.; Hirabayashi, S.; Moriyama, R., Anomalously high-density glass of ethylbenzene prepared by vapor deposition at temperatures close to the glass-transition temperature. *Chem. Phys. Lett.* **2008,** *459* (1–6), 109-112.

18. Nakayama, H.; Omori, K.; Ino-u-e, K.; Ishii, K., Molar Volumes of Ethylcyclohexane and Butyronitrile Glasses Resulting from Vapor Deposition: Dependence on Deposition Temperature and Comparison to Alkylbenzenes. *The Journal of Physical Chemistry B* **2013,** *117* (35), 10311-10319.

19. Chen, Z.; Richert, R., Dynamics of glass-forming liquids. XV. Dynamical features of molecular liquids that form ultra-stable glasses by vapor deposition. *Journal of Chemical Physics* **2011,** *135* (12), 124515.

20. Dalal, S. S.; Ediger, M. D., Influence of substrate temperature on the transformation front velocities that determine thermal stability of vapor-deposited glasses. *J Phys Chem B* **2015,** *119* (9), 3875-82.

21. Whitaker, K. R.; Scifo, D. J.; Ediger, M. D.; Ahrenberg, M.; Schick, C., Highly stable glasses of cis-decalin and cis/trans-decalin mixtures. *J Phys Chem B* **2013,** *117* (42), 12724-33.

22. Bhattacharya, D.; Sadtchenko, V., Vapor-deposited non-crystalline phase vs ordinary glasses and supercooled liquids: Subtle thermodynamic and kinetic differences. *J Chem Phys* **2015,** *142* (16), 164510.

23. Leon-Gutierrez, E.; Sepulveda, A.; Garcia, G.; Clavaguera-Mora, M. T.; Rodriguez-Viejo, J., Stability of thin film glasses of toluene and ethylbenzene formed by vapor deposition: an in situ nanocalorimetric study. *Physical Chemistry Chemical Physics* **2010,** *12* (44), 14693-14698.

24. Lyubimov, I.; Antony, L.; Walters, D. M.; Rodney, D.; Ediger, M. D.; de Pablo, J. J., Orientational anisotropy in simulated vapor-deposited molecular glasses. *J Chem Phys* **2015,** *143* (9), 094502.

25. Dalal, S. S.; Walters, D. M.; Lyubimov, I.; de Pablo, J. J.; Ediger, M. D., Tunable molecular orientation and elevated thermal stability of vapor-deposited organic semiconductors. *Proc Natl Acad Sci U S A* **2015,** *112* (14), 4227-32.

26. Geske, J.; Drossel, B.; Vogel, M., Fragile-to-strong transition in liquid silica. *AIP Advances* **2016,** *6* (3), 035131.

27. Zhou, C.; Hu, L.; Sun, Q.; Zheng, H.; Zhang, C.; Yue, Y., Structural evolution during fragile-to-strong transition in CuZr(Al) glass-forming liquids. *The Journal of Chemical Physics* **2015,** *142* (6), 064508.

Chapter Seven: Future research directions

The preceding Chapters in this Dissertation focused, primarily, on fundamental physical processes in rapidly heated molecular materials and their potential utility for gaining insights into exceedingly slow kinetics in amorphous solids at temperatures below T_g. The compounds for these FSC studies and the sample preparation procedures were selected to align with the goal of demonstrating the accuracy and potential of the FSC technique and data analysis. Having achieved this goal, I would like to suggest several glass-forming compounds that have properties which are significantly distinct from methyl-benzene (MB), e.g. molecular structure, intermolecular bonding, and supercooled liquid fragility. The compounds suggested in Table 7.1 are suitable to the FSC apparatus and would facilitate the generalization of the essential conclusions of my dissertation.

From the compounds listed in Table 7.1, the mono-hydroxyl alcohols, e.g. 2-butanol or 2-methyl-1-propanol, would be the most interesting class of glass-forming compounds for future FSC studies. The hydrogen bond interactions in these molecular liquids are much stronger than the typical intermolecular bonding found in glass-formers such as the relatively fragile MB. Network-forming glasses, such as silicon dioxide[3] or glycerol[5], typically have very low fragility indexes and the temperature dependence of these mobility parameters in these network-forming glasses are predicted to be strongly Arrhenius-like[7]. Yet, most network-forming liquids also have exceedingly low vapor pressure at ambient conditions, making them incompatible with our FSC apparatus. Fortunately, monohydroxy alcohols, with their relatively high vapor pressures (see Table 7.1) provide an alternative to glycerol and other hydrogen bonded systems. As demonstrated by the preliminary experiments with 2-propanol in Chapter 3 and Chapter 4,

Table 7.1.	Formula	MW g·mol^{-1}	T_m K	T_g K	m_A	VP mmHg
Aromatic Glass-formers						
methyl benzene	$C_6H_5CH_3$	92.1	α: 178 β: 153	117.2[c]	104[c]	22
ethyl benzene	$C_6H_5CH_2CH_3$	106.2	178	115.7[c]	98[c]	10
iso-propyl benzene	$C_6H_5CH(CH_3)_2$	120.2	177	125[b]	70[b]	8
n-propyl benzene	$C_6H_5(CH_2)_2CH_3$	120.2	174	122[b]	69[b]	2
m-xylene	$C_6H_4(CH_3)_2$	106.2	225	120[b]	56[b]	8.3
o-xylene	$C_6H_4(CH_3)_2$	106.2	248	123[b]	55[b]	6.6
Non-Aromatic Glass-formers						
ethyl cyclo-hexane	$C_6H_{11}CH_2CH_3$	112.21	162	101[g]	57[c]	31
propylene carbonate	$CH_3C_2H_3O_2CO$	102.09	218	159.5[a]	99[a]	0.13
cis-trans decalin mix	$C_6H_{10}(CH_2)_4$	138.25	*c:* 230.3 *t:* 242.7	*mix:* 137.4[a]	145[a]	2.3
Mono-Hydroxyl Alcohols						
2-ethyl-1-hexanol	$CH_3(CH_2)_3CH$-$(CH_2CH_3)CH_2OH$	130.23	197	146[b]	72[b]	0.2
4-methyl-3-heptanol	$CH_3(CH_2)_2CH$-$(CH_3)CH(OH)CH_2CH_3$	130.23	150	162[b]	57[b]	0.9
1-propanol	$CH_3CH_2CH_2OH$	60.1	148	98[e]	40[e]	21
2-propanol	$(CH_3)_2CHOH$	60.1	185	115[e]	~55[e]	23
1-butanol	$CH_3(CH_2)_3OH$	74.12	183.3	111[e]	59[e]	6
2-butanol	$CH_3CHOHCH_2CH_3$	74.12	158	118[e]	63[e]	12.5
2-methyl-1-propanol	$(CH_3)_2CHCH_2OH$	74.12	165	107[a]	39[a]	9
1-pentanol	$CH_3(CH_2)_3CH_2OH$	88.15	195	121[b]	--	2.2
2-methyl-1-butanol	$CH_3CH_2CH(CH_3)$-CH_2OH	88.15	156	123.6[f]	46[f]	3

Table. 7.1. Glass-forming compounds suggested for future FSC research studies. The T_g and m_A values were derived from data: a[1], b[2], c[4], f[6], d[8] ,e[9],g[10]. All other data was obtained from PubChem[11]. Vapor pressure (VP) is at ambient temperature.

the activation energy barrier to relaxation front propagation in these materials is typically lower than for fragile systems. Though we anticipate smaller temperature variations in the E_a barriers to relaxation for mono-hydroxyl alcohols, the sensitivity in measurements of absolute transformation rate and the relationship to self-diffusivity demonstrated by FSC experiments with MB indicate that calculating absolute Z values for alcohols may provide us with some useful information on the impact of hydrogen bonding on molecular mobility.

My second suggestion for a future research direction is the development of a complimentary technique using the existing components of the calorimeter's data acquisition system. As discussed in Chapter 2, the thermal conductivity of a glassy sample limits the range of possible FSC heating rates. Yet, for many compounds, there are few data on its thermal properties at temperatures near T_g, and we must rely on estimating the thermal equilibration time from extrapolations of existing data (see Section 2.8). However, it may be possible to utilize the existing components of the FSC apparatus to measure thermal conductivity of condensed phases near T_g. Immediately below, I provide a brief review of the thermal properties of glassy materials and the proposed apparatus modification that would allow measuring these properties in glassy films.

The thermal conductivity, κ, of condensed phases carries a wealth of structural information and is therefore studied extensively. Molecular crystals usually follow the Debye model[12,13] of phonon dispersion at low temperatures, with both heat capacity and thermal conductivity proportional to T^3, unless material boundaries interfere. At higher temperatures, crystals have increased phonon scattering, due to anharmonistic vibration, and resistance to thermal momentum transfer, due to Umklapp processes[12]. At temperatures significantly above the Debye temperature[12], a simple kinetic model for

perfect crystals predicts the dependence of thermal conductivity on the phonon mean free path, $l(T)$:

$$\kappa(T) \approx \frac{1}{3} C \cdot v \cdot l(T), \quad (7.1)$$

where the heat capacity, *C,* is assumed to be approximately constant and the speed of sound in the material, v, is proportional to $l(T)$. In perfect, large crystals, $l(T)$ is proportional to temperature with a negative exponent[14]. However, the $l(T)$ and, consequently, $\kappa(T)$ depend strongly on the microscopic structure of the material, such as the density of defects.

To illustrate, in semi-disordered molecular crystals[15], $\kappa(T)$ decreases significantly because the phonons have a reduced mean free path[12], i.e. are scattered by defects. In glassy amorphous solids, $l(T)$ decreases even further and is assumed to be on the scale of intermolecular distances[15]. Above 30K, heat transfer in simple but disordered materials, i.e. metallic and ionic high-defect crystals, typically fits an empirical equation that is based on Einstein's random walk model[15]. The Einstein model predicts a non-zero minimum of thermal conductivity for all simple materials, and glassy amorphous solids are thought to approach that limit[14-15]. In other words, $\kappa(T)$ in completely disordered isotropic amorphous condensed phases should approach that theoretical minimum in thermal heat conductivity[14]. It is therefore logical to expect that the structurally anisotropic VD amorphous phases will have a thermal conductivity that is distinct from that of ordinary isotropic molecular glasses. Furthermore, as illustrated by the recent work by Mizuno at al[16] and Hopkins[17], for super-lattices with a lamellar structure, the transverse conductivity may be *below* Einstein's theoretical limit.

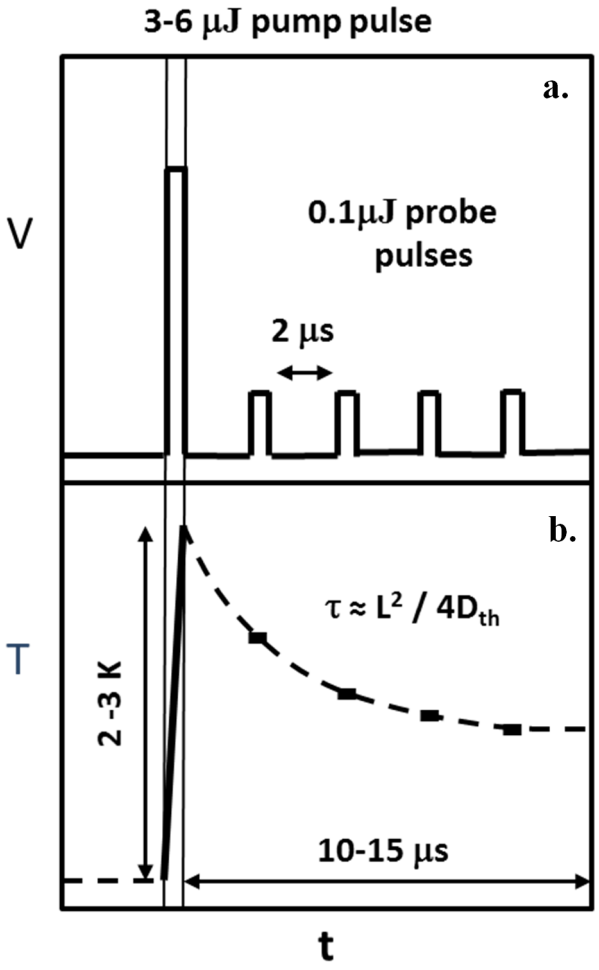

Fig. 7.1. Experimental protocol and DAQs modifications necessary to measure the relative transverse thermal diffusivity for vapor-deposited or melt-cooled amorphous films. The initial heat pulse is followed by a series of probing pulses. Each pulse allows the temperature of the filament to be measured. The thermal relaxation time equation (Eq. 2.6) for our cylindrical geometry is shown in the lower panel(b).

The modifications needed to measure the thermal properties of molecular films by FSC are not extensive. As I explained in Chapter 2, the primary output of our FSC experiments is the effective heat capacity during rapid heating, but an alternative program of data acquisition may make it possible to *qualitatively* measure the relative transverse thermal diffusivity of the films. The experimental approach to thermal diffusivity measurements is illustrated in Fig. 7.1. As shown in the figure, first, the temperature of the filament is raised by 2–3 K. This can be accomplished by applying a potential difference of 30 V across the filament to generate a short (e.g. 0.3 μs) heating pulse of 5μJ. This heat pulse is significantly shorter than the characteristic thermal equilibration time, τ_{th}, between the filament and a molecular film. In other words, the initial jump in the filament temperature will be followed by a gradual decrease due to the heat transfer from the filament to the molecular film.

This heat transfer is governed by the film's thermal diffusivity, D_{th}, which is proportional[18] to its κ:

$$\kappa(T) = D_{th}(T) \cdot C_p(T) \cdot \rho(T), \quad (7.2)$$

where $\rho(T)$ is the material's density. For example, as discussed in Chapter 2.8, for supercooled liquids such as MB[19], the D_{th} at 180 K is expected to be approximately 10^{-7}m·s^{-1}. Using the Einstein-Smoluchowski equation[20] (Eq. 2.6), we can predict the film's thermal equilibration time, τ_{vib}, which is approximately 5 μs for a 2-μm-thick molecular liquid film. In general, a liquid's thermal conductivity increases with lower temperatures and, although the κ of amorphous solids is below that of crystals[15], it is still predicted to be higher than that of supercooled liquids[5, 14].

Because of the low specific heat capacity of tungsten[21], the overall heat capacity of

the filament is close to that of the film, which is verified by direct heat capacity measurements in our experiments (see Chapter 2). Therefore, the initial temperature jump of 2 – 3 K is followed by a 1 – 1.5 K decrease in the temperature of the filament due to heat transfer. This temperature decrease occurs on the timescale of tens of milliseconds, as shown in Fig. 7.1.b. As the filament cools, the temperature of the filament can be measured by generating a sequence of short (0.3 μs) current pulses of low magnitude, such that the overall energy of each pulse is lower than 0.1 μJ (see Fig. 7.1.a). According to our estimates, such a low-energy pulse sequence will not produce enough heat to affect the filament temperature variations, as long as the interval between the pulses is greater than 2 μs; i.e. as long as the net energy delivered by the probe pulse sequence is significantly less than that delivered by the initial heating pump pulse, during the experiments (5 - 15 μs). As shown in Fig. 7.1.b, the data collected would result in a time dependent temperature curve of the filament, whose shape will be defined primarily by the thermal diffusivity of the molecular film.

The temperature decay curves can, in principle, be fit to analytical solutions of the heat transport equation representative of our experimental geometry with the appropriate initial and boundary conditions. Such fits may yield the absolute values of τ_{th} and D_{th}. With estimates of $\rho(T)$ and measurements of $C_p(T)$, the D_{th} can, in principle, be used to calculate $\kappa(T)$. However, the accurate measurement of *absolute* thermal diffusivity would not be the primary goal of these heat conductivity studies. Our task is much easier and consists of detecting *variations* in the thermal relaxation time for films of molecular solids prepared under distinct conditions. These variations can be detected by slower or faster thermal equilibration between the filament and film, i.e. differing *T(t)* curves.

In addition to answering a wide array of other fundamental questions, these comparative studies of a thermal conductivity will be invaluable for resolving the current dispute about the structure and physical properties of stable vapor deposited glasses. As I mentioned briefly in Chapter 4 and Chapter 6, there is an on-going debate in the glass community on the analogy between VD phases and their melt-cooled counterparts. Although some experiments[22] with the VD films imply that the enthalpy[23], density[23-25], and speed of sound[26] are consistent with the values characteristic of *equilibrium* supercooled liquids at some characteristic fictive temperature, T_f, there are also experimental results that contradict these findings. Numerous wide-angle x-ray scattering and simulation studies that show that low-temperature vapor deposition of certain compounds may result in the formation of an *anisotropic* phases[27-30]. In other words, these VD phases are not structurally identical to isotropic supercooled liquids with low fictive temperatures. Because the thermal diffusivity of the condensed phase is sensitive to variations in microscopic structure, we would expect a *qualitative* difference between the thermal equilibration curves of stable vapor-deposited amorphous phases and ordinary melt-cooled glasses. Such an observation may clarify the origin of the cross-over behavior observed for stable VD phases in Chapter 6 and would be a significant contribution to the field of glass science.

7.1. References for Chapter Seven

1. Wang, L. M.; Angell, C. A.; Richert, R., Fragility and thermodynamics in nonpolymeric glass-forming liquids. *J Chem Phys* **2006,** *125* (7), 074505.
2. Wang, L. M.; Richert, R., Glass transition dynamics and boiling temperatures of molecular liquids and their isomers. *J Phys Chem B* **2007,** *111* (12), 3201-7.
3. Ojovan, M. I.; Lee, W. E., Viscosity of network liquids within Doremus approach. *J. Appl. Phys.* **2004,** *95* (7), 3803-3810.
4. Chen, Z.; Richert, R., Dynamics of glass-forming liquids. XV. Dynamical features of molecular liquids that form ultra-stable glasses by vapor deposition. *Journal of Chemical Physics* **2011,** *135* (12), 124515.
5. Andersson, O.; Johari, G. P., Thermal conductivity of Glycerol's liquid, glass, and crystal states, glass-liquid-glass transition, and crystallization at high pressures. *J Chem Phys* **2016,** *144* (6), 064504.
6. Wang, L. M.; Richert, R., Glass Transitions in Viscous Monohydroxy Alcohols: Calorimetry Versus Dielectric Relaxation. *International Journal of Thermophysics* **2008,** *29* (6), 2055-2061.
7. Böhmer, R.; Ngai, K. L.; Angell, C. A.; Plazek, D. J., Nonexponential relaxations in strong and fragile glass formers. *The Journal of Chemical Physics* **1993,** *99* (5), 4201.
8. Whitaker, K. R.; Scifo, D. J.; Ediger, M. D.; Ahrenberg, M.; Schick, C., Highly stable glasses of cis-decalin and cis/trans-decalin mixtures. *J Phys Chem B* **2013,** *117* (42), 12724-33.
9. Ramos, M. A.; Kabtoul, B.; Hassaine, M., Calorimetric and thermodynamic study of glass-forming monohydroxy alcohols. *Philosophical Magazine* **2011,** *91* (13-15), 1847-1856.
10. Ramos, S. L.; Chigira, A. K.; Oguni, M., Devitrification properties of vapor-deposited ethylcyclohexane glasses and interpretation of the molecular mechanism for formation of vapor-deposited glasses. *J Phys Chem B* **2015,** *119* (10), 4076-83.
11. Shiratani, E.; Sasai, M., Molecular scale precursor of the liquid-liquid phase transition of water. *Journal of Chemical Physics* **1998,** *108* (8), 3264-3276.
12. Kittel, C., *Introduction to solid state physics*. Wiley: Hoboken, NJ, 2005.
13. Yoshioka, D., The Heat Capacity of a Solid. In *Statistical Physics: An Introduction*, Springer Berlin Heidelberg: Berlin, 2006; pp 67-81.

14. Konstantinov, Heat Transfer in Molecular Crystals. In *Heat Transfer - Theoretical Analysis, Experimental Investigations and Industrial Systems*, Belmiloudi, A., Ed. InTech: Rijeka, Croatia 2011; pp 157-188.

15. Cahill, D. G.; Watson, S. K.; Pohl, R. O., Lower limit to the thermal conductivity of disordered crystals. *Phys. Rev. B* **1992,** *46* (10), 6131-6140.

16. Mizuno, H.; Mossa, S.; Barrat, J. L., Beating the amorphous limit in thermal conductivity by superlattices design. *Sci Rep* **2015,** *5*, 14116.

17. Hopkins, P. E.; Piekos, E. S., Lower limit to phonon thermal conductivity of disordered, layered solids. *Appl. Phys. Lett.* **2009,** *94* (18), 181901.

18. Watanabe, H.; Kato, H., Thermal Conductivity and Thermal Diffusivity of Twenty-Nine Liquids: Alkenes, Cyclic (Alkanes, Alkenes, Alkadienes, Aromatics), and Deuterated Hydrocarbons. *Journal of Chemical & Engineering Data* **2004,** *49* (4), 809-825.

19. Ramires, M. L. V.; de Castro, C. A. N.; Perkins, R. A.; Nagasaka, Y.; Nagashima, A.; Assael, M. J.; Wakeham, W. A., Reference data for the thermal conductivity of saturated liquid toluene over a wide range of temperatures. *Journal of Physical and Chemical Reference Data* **2000,** *29* (2), 133-139.

20. Lindsay, S., *Introduction to Nanoscience*. OUP Oxford: 2009.

21. Krause, D., Glasses. In *Springer Handbook of Condensed Matter and Materials Data*, Martienssen, W.; Warlimont, H., Eds. Springer Berlin Heidelberg: 2005; pp 523-574.

22. Ediger, M. D.; Harrowell, P., Perspective: Supercooled liquids and glasses. *The Journal of Chemical Physics* **2012,** *137* (8).

23. Swallen, S. F.; Kearns, K. L.; Mapes, M. K.; Kim, Y. S.; McMahon, R. J.; Ediger, M. D.; Wu, T.; Yu, L.; Satija, S., Organic Glasses with Exceptional Thermodynamic and Kinetic Stability. *Science* **2007,** *315* (5810), 353-356.

24. Ishii, K.; Nakayama, H.; Hirabayashi, S.; Moriyama, R., Anomalously high-density glass of ethylbenzene prepared by vapor deposition at temperatures close to the glass-transition temperature. *Chem. Phys. Lett.* **2008,** *459* (1–6), 109-112.

25. Dalal, S. S.; Walters, D. M.; Lyubimov, I.; de Pablo, J. J.; Ediger, M. D., Tunable molecular orientation and elevated thermal stability of vapor-deposited organic semiconductors. *Proc Natl Acad Sci U S A* **2015,** *112* (14), 4227-32.

26. Fakhraai, Z.; Still, T.; Fytas, G.; Ediger, M. D., Structural Variations of an Organic Glassformer Vapor-Deposited onto a Temperature Gradient Stage. *Journal of Physical Chemistry Letters* **2011,** *2* (5), 423-427.

27. Dawson, K.; Kopff, L. A.; Zhu, L.; McMahon, R. J.; Yu, L.; Richert, R.; Ediger, M. D., Molecular packing in highly stable glasses of vapor-deposited tris-naphthylbenzene isomers. *Journal of Chemical Physics* **2012,** *136* (9).

28. Ishii, K.; Nakayama, H., Structural relaxation of vapor-deposited molecular glasses and supercooled liquids. *Physical Chemistry Chemical Physics* **2014,** *16* (24), 12073-12092.

29. Lyubimov, I.; Antony, L.; Walters, D. M.; Rodney, D.; Ediger, M. D.; de Pablo, J. J., Orientational anisotropy in simulated vapor-deposited molecular glasses. *J Chem Phys* **2015,** *143* (9), 094502.

30. Dawson, K. J.; Zhu, L.; Yu, L.; Ediger, M. D., Anisotropic Structure and Transformation Kinetics of Vapor-Deposited Indomethacin Glasses. *The Journal of Physical Chemistry B* **2011,** *115* (3), 455-463.